INVESTIGATION OF THERMAL PERFORMANCE OF DOUBLE TAPERED AND ELLIPTICAL FIN MICROCHANNEL HEAT SINKS

Submitted in partial fulfillment of the requirements
for the award of the degree of

DOCTOR OF PHILOSOPHY

by

PALLIKONDA MAHESH

(Roll No.717123)

Supervisor:

Prof. K. KIRAN KUMAR

DEPARTMENT OF MECHANICAL ENGINEERING
NATIONAL INSTITUTE OF TECHNOLOGY
WARANGAL-506004, (T.S) INDIA

JANUARY- 2023

THESIS APPROVAL FOR Ph.D.

This thesis entitled **"INVESTIGATION OF THERMAL PERFORMANCE OF DOUBLE TAPERED AND ELLIPTICAL FIN MICROCHANNEL HEAT SINKS"** by **Mr. Pallikonda Mahesh** is approved for the degree of Doctor of Philosophy.

Examiners

_____

_____

_____

Supervisor

Prof. K. Kiran Kumar

Mechanical Engineering Department, NIT Warangal

Chairman

Prof. V. Suresh Babu

Head, Mechanical Engineering Department, NIT Warangal

NATIONAL INSTITUTE OF TECHNOLOGY WARANGAL
(T.S) INDIA 506004

CERTIFICATE

This is to certify that the thesis entitled **"Investigation of Thermal Performance of Double Tapered and Elliptical Fin Microchannel Heat Sinks"**, submitted by **Mr. Pallikonda Mahesh (717123)** for partial fulfillment of the award of **Doctor of Philosophy** (**Ph.D.)** in the Department of Mechanical Engineering, National Institute of Technology Warangal, is a record of research work done under my guidance. There results embodied in this thesis have not been submitted to any other Universities or Institutes for the award of any degree or diploma.

Prof. K. Kiran Kumar
Thesis Supervisor
Department of Mechanical Engineering,
National Institute of Technology, Warangal.

.

NATIONAL INSTITUTE OF TECHNOLOGYWARANGAL

(T.S) INDIA 506004

DECLARATION

This is to certify that the work presented in the thesis entitled **"Investigation of Thermal Performance of Double Tapered and Elliptical Fin Microchannel Heat Sink"**, was done by me under the guidance of Prof. K. Kiran Kumar and was not submitted elsewhere for the award of any degree.

I declare that this written submission represents my idea in my own words and where other's ideas or words have not been included. I have adequately cited and referenced the original sources. Also, I affirm that I have followed all standards of academic honesty and integrity and have not fabricated or falsified or manipulated any idea/data/fact/source in my submission. I understand that any violations of the above rules, the Institute may take disciplinary action as well as financial penalties for sources that I failed to properly cite or obtain permission

Date: 02/01/2023 **(Pallikonda Mahesh)**

Place: Warangal Research Scholar,

Roll No.717123.

Acknowledgements

The success and completion of my research requires guidance, assistance and encouragement from many people and I am extremely lucky to have got this throughout the duration of my research work. Whatever I have achieved, that is solely due to such guidance, assistance and encouragement. I take this opportunity to express my deep gratitude to everyone who helped me successful completion of my research.

First and foremost, I would like to express my deep sense of gratitude to my research supervisor **Prof. K Kiran Kumar,** MED, NIT Warangal for introducing me to this emerging field of microchannel heat sink and for his unwavering assistance, advice, inspiration and encouragement, which helped me to become a capable researcher. His commitment, systematic approach to research, and determination to produce high-quality work left a lasting impression on me. I am highly indebted to him for sharing his knowledge and expertise.

I would like to extend my sincere gratitude to **Dr. Karthik Balasubramanian** for his supervision and motivation as well as for providing necessary information pertaining to research and also for the support in completing research. I am highly indebted to him for sharing his knowledge and expertise.

I wish to express my sincere thanks to, **Prof. N. V. Ramana Rao**, Director, National Institute of Technology, Warangal for his official support and encouragement. I am very thankful to **Prof. V Suresh Babu, Head of Mechanical Engineering Department** for his constant support and cooperation. I also express my gratitude to **Prof. A. Kumar, Prof. R N Rao, Prof. N. Selvaraj** and **Prof. P. Bangaru Babu,** former head of Mechanical Engineering Department for their constant support and cooperation. I take this privilege to thank all my doctoral scrutiny committee (DSC) members **Prof. G. Naga Srinivasulu,** Mechanical Engineering Department,**Dr. Karthik Balasubramanian,** Associate Professor, Mechanical Engineering Department,**Prof. Shirish H Sonawane,** Chemical Engineering Department, National Institute of Technology, Warangal for their kind help, encouragement and valuable suggestions for successful completion of research work.

I wish to express my heartfelt thanks to Prof**. K. Amba Prasad Rao, Prof. VP Chandra Mohan, Prof. D. Jaya Krishna, Prof. C. Gururaja Rao and Prof. D. S. Kesava Rao,** for their guidance during course work. I would like to express my heartfelt thanks to **Dr. M. R. Vishwanathan, H&SS** department for suggestions in writing scientific Journals. I also express my thanks to all the faculty members and technical staff of Mechanical Engineering Department, NIT Warangal for the knowledge they have imparted me. My sincere thanks to fellow-scholars **Dr. Venkata Sai Sudheer, Dr. B Ramesh Babu**, **Dr. J. A. Ranga Babu, Dr. BrindavanPatro, Mr. Nandan Hegde, Mr. Raghuvaran,**for technical discussions during my research work. My special thanks to **Mr. M. Nitin Kumar & Reeti Mukherjee** for technical discussions and suggestions; and fellow batch mates**, Dr. Pittala Rajkumar, Dr. K Lokesh, Mr. M Sateesh Kumar Mr. S Rakesh Mr. Upendra and Mr. Rafaq** for their enormous support and encouragement. I would like to thanks my fellow scholars and friends **Dr.DRavi Chandra, Dr. Venkateshwara Babu, Mr. Shashi Kumar, Mr. Ragavan, Mr. Sandeep and Ch. Sravan Kumar** and many others for always being at my side and sharing a valuable information with me. I will always be grateful for their friendship.

I am always grateful to my parents (**Pallikonda Mallaiah & Laxmi**) for their care and countless sacrifices for my growth. Your prayers for me have made me what I am today. Finally, I render my thanks to all my family members (My wife: **Mrs.Pallikonda Sri Vathsavi**, Brother: **Mr. Pallikonda Harish,** Sisters & Brother in laws: **Arolla Pushpa Latha & Ravi**, **Indarapu Jamuna & Ramesh**, **Arolla Rajita & Prashant,** Uncle & Aunty: **Muchakurthy Bhumesh & Padma)** for giving moral support. They inspired and supported me all through my life. I would also like to use this opportunity to express my gratitude to all my family members, friends, and well-wishers who are the part of my success directly and indirectly.

NIT Warangal
JANUARY2023 (**Pallikonda Mahesh**)

Abstract

Microchannel heat sinks are the parallel flow paths having larger convective surface area and high heat transfer coefficient due to their micro size passages. The enhanced cooling characteristics of microchannel heat sink are more attractive to use in high heat transfer applications. A steady incompressible three dimensional forced convection of three distinct microchannel heat sinks (rectangular, double tapered and elliptical fin microchannel) were numerically investigated and compared by considering identical foot print area, heat flux and Re. The governing equations were solved by using finite volume method. The fluid behavior and heat transfer performance were analyzed within a laminar flow regime of Re 174-768. Among all the considered geometries, the elliptical fin microchannel yields better cooling performance. Besides this, the rise in wall temperature was reduced in comparison to straight rectangular fin microchannel. Then for elliptical fin microchannel heat sink, design parameters such as ellipticity ratio, orientation angle, fin height and fin to fin centre distance were varied to obtain optimal design parameters. Using temperature, pressure, friction factor, and Nusselt number results, the best performance parameters of an elliptical microchannel were determined and compared to that of a straight fin microchannel. The highest performance factor was found to be 1.61 for an optimal elliptical microchannelat Re -174. The optimal parameters of elliptical fin microchannel are ellipticity ratio of 0.20, orientation angle of 2°, fin height of 1mm, and a centre distance of 3mm. Finally, different nanofluids (CuO-water and Al_2O_3-water), heat sink materials, and different nanoparticle concentrations (0.125% - 1%) were employed in optimal designed microchannel heat sink to evaluate cooling performance of heat sink numerically and experimentally. The problem was modeled as incompressible, laminar and steady state two phase mixture model for nanofluid flow. The commercial ANSYS CFD software was employed to solve the governing equations. With the addition of nanoparticles to the base fluid, it was possible to further enhance the performance factor by 41% and to decrease the wall temperature by 14% (7.2°C) and the thermal resistance by 17% for 1% nanofluid at Re 436.

Table of Contents

Acknowledgements i

Abstract iii

List of figures viii

List of tables xiii

Nomenclature xiv

CHAPTER 1 1

Introduction 1

1.1 Background 1

1.2 Microchannel fabrication 2

1.3 Heat sink material 2

1.4 Coolants 3

1.4.1 Nanofluids 3

1.5 Applications of microchannel heat sinks 5

1.6 Motivation 6

1.7 Research Objectives 7

1.8 Outline of the thesis 8

1.9 Closure 8

CHAPTER 2 9

Literature survey 9

2.1 Straight microchannel 9

2.2 Effect of extended surface in conventional channel 11

2.3 Effect of microchannel cross sectional area 11

2.4 Effect of microchannel fin geometry 13

2.5 Effect of nanofluids on microchannel heat sinks 15

CHAPTER 3 18

Approach and Methodology 18

3.1 Geometrical models 18

3.2 Grid refinement 18

3.3 Numerical schemes for single-phase 19

3.4 Numerical schemes for two-phase 20

3.5 Assumptions 20
3.6 Governing equations 22
3.6.1 Single phase fluid 22
3.6.2 Two phase fluid 23
3.7 Data reduction 23
3.8 Numerical validation 27
CHAPTER 4 28
Optimization of double tapered microchannel heat sink geometry 28
4.1 Computational modelling of microchannel heat sink 28
4.2 Effect of height ratio on average bottom wall temperature, temperature difference ratio, thermal resistance ratio and pumping power. 32
4.2.1 Average bottom wall temperature 32
4.2.2 Temperature difference ratio 33
4.2.3 Thermal resistance ratio 34
4.2.4 Pumping power 36
4.3 Effect of width ratio on bottom wall temperature, temperature difference ratio, thermal resistance ratio and pumping power. 36
4.3.1 Average bottom wall temperature 36
4.3.2 Temperature difference ratio 38
4.3.3 Thermal resistance ratio 38
4.3.4 Pumping power 41
4.4 Effect of height and width ratio on bottom wall temperature, temperature difference ratio, thermal resistance ratio and pumping power. 41
4.4.1 Average bottom wall temperature 41
4.4.2 Temperature difference ratio 43
4.4.3 Thermal resistance ratio 43
4.4.4 Pumping power 43
4.5 Conclusions 48
CHAPTER 5 50
Numerical study of elliptical fin microchannel heat sink 50
5.1 Computational modeling 51
5.2 Flow characteristics 52

5.2.1 Pressure drop 52
5.2.2 Local pressure 54
5.2.3 Friction factor 56
5.3 Heat transfer characteristics 57
5.3.1 Average wall temperature 57
5.3.2 Local wall temperature 58
5.3.3 Average Nusselt number 60
5.3.4 Local Nusselt number 62
5.3.5 Velocity and temperature contours 64
5.3.6 Performance factor 66
5.4 Conclusion 67
CHAPTER 6 68
Parametric analysis of elliptical fin microchannel heat sink 68
6.1 Numerical Modeling 68
6.2 Effect of ellipticity ratio 71
6.2.1 Pressure drop characteristics 72
6.2.2 Velocity streamlines 74
6.2.3 Thermal characteristics 76
6.2.4 Performance factor 77
6.3 Effect of Fin orientation angle 78
6.4 Effect of Fin height 78
6.4.1 Pressure drop characteristics 78
6.4.2 Thermal characteristics 80
6.4.3 Performance factor 82
6.5 Effect of fin centre to centre distance 83
6.5.1 Pressure drop characteristics 83
6.5.2 Thermal characteristics 85
6.5.3 Performance factor 87
6.6 Conclusions 88
CHAPTER 7 90
Numerical study of nanofluids on optimized elliptical fin microchannel heat sink 90

7.1 Effect of heat sink material on Nu and thermal resistance 90
7.2 Effect of two different nanofluids on friction factor and Nu 91
7.3 Effect of volume fraction and Re on flow characteristics 93
7.4 Effect of volume fraction and Re on heat transfer characteristics 94
7.5 Conclusions 97
CHAPTER 8 99
Experimental study of nanofluids on optimized elliptical fin microchannel heat sink 99
8.1 Experimental setup 99
8.1.1 Microchannel test rig 99
8.1.2 Test Section 101
8.1.3 Microchannel fabrication 102
8.1.4 Nanofluid preparation 104
8.2 Estimation of thermo-physical properties of nanofluids 106
8.2.1 Density and specific heat of nanofluid (Theoretical) 106
8.2.2 Thermal conductivity (Experimental) 106
8.2.3 Viscosity of nanofluid (Experimental) 107
8.3 Data reduction 108
8.3.1 Heat transfer 108
8.3.2 Pressure drop 110
8.4 Uncertainty analysis 110
8.5 Flow characteristics 112
8.6 Heat transfer characteristics 113
8.7 Conclusions 117
CHAPTER 9 119
Overall conclusions and scope for future research 119
9.1 Overall conclusions 119
9.2 Scope for future research 121
Publications 122
References 123

List of figures

Figure 1.1 Thermal conductivity of different materials (Reference from [2], [3]) 4

Figure 3.1 The meshing of elliptical microchannel 19

Figure 3.2 Variation of pressure and wall temperature with Reynolds number 27

Figure 4.1 Schematic of double taper MCHS.(The figure is not drawn to scale) (a) front view(b) top view (c) side view (d) computational domain (e) heat sink 31

Figure 4.2 Effect of height tapered ratio and Re on (a) average bottom wall temperature, $(T_w)_{avg}$ (b) $\sigma_{\Delta T}$ (c) ξ_R and (d) pumping power, P 32

Figure 4.3 Temperature and velocity contours of height tapered MCHS at Reynolds number 340 (a) temperature contours in X-Y, Z-X plane (b) velocity contours in X-Y, Z-X plane (c) temperature contours in transverse (Z-Y plane) section (d) velocity contours in transverse (Z-Y plane) section 35

Figure 4.4 Effect of width tapered ratio and Re on (a) average bottom wall temperature, $(T_w)_{avg}$ (b) $\sigma_{\Delta T}$ (c) ξ_R and (d) pumping power, P 37

Figure 4.5 Temperature contours and velocity contours of width tapered MCHS (a) temperature contours in X-Y and Z-X plane (b) velocity contours in X-Y and Z-X plane (c) temperature contours in transverse section and (d) velocity contours in transverse section 40

Figure 4.6. Effect of width and height tapered ratio at Re 340 on (a) average bottom wall temperature,$(T_w)_{avg}$ (b) $\sigma_{\Delta T}$ (c) ξ_R (d) pumping power, P 42

Figure 4.7 Width tapered MCHS at constant H_y-3.9 (a) temperature contours in X-Y and Z-X plane (b) velocity contours in X-Y and Z-X plane (c) temperature contours in transverse section and (d) velocity contours in transverse section 45

Figure 4.8 Temperature and velocity contours of (a) straight and (b) best design channel (DTMC) 47

Figure 5.1 Schematic of elliptical MCHS (The Figure is not drawn to scale) (a) top view (b) 3D view (c) computational domain 51

Figure 5.2 Pressure drop for various angles of elliptical fin arrangement with flow direction for heat flux of (a) 50 W/cm^2 (b) 65 W/cm^2 53

Figure 5.3 (A) The effect of local static pressure along with downstream of flow at Re 436 for (a) 50 W/cm^2 and (b) 65 W/cm^2. (B) pressure contours at various locations (in Y-Z plane). 55

Figure 5.4 The friction factor of straight fin and elliptical fin microchannels for (a) 50 W/cm^2 b) 65 W/cm^2 57

Figure 5.5 Variation of average wall temperature for various angles of elliptical fin arrangement with flow direction for (a) 50 W/cm^2 (b) 65 W/cm^2..... 57

Figure 5.6 (A) The effect of local wall temperature along with the downstream of flow at Re 436 for (a) 50 W/cm^2 and (b) 65 W/cm^2. (B) temperature distribution at various locations (in Y-Z plane)……..59

Figure 5.7 (A) Variation of average Nusselt number with flow direction for different angles of elliptical fin arrangement for (a) 50 W/cm^2 (b) 65 W/cm^2 (B) temperature contours at mid plane (X-Z), Re- 436 for (a) straight fin microchannel (SFMC) (b) 2^o elliptical fin microchannel (EFMC) (C) velocity vectors of various elliptical fin microchannel (X-Z plane, 23 mm from inlet) at Re - 436, heat flux 50 W/cm^2…….....…….....61

Figure 5.8 The effect of Nusselt number along with the downstream flow for straight fin microchannel (SFMC) and 2^o elliptical fin microchannel (EFMC) at Re 436 for (a) 50 W/cm^2 and (b) 65 W/cm^2 (c) 50 locations long the channel length in elliptical fin microchannel……..…63

Figure 5.9 Temperature and velocity distribution of straight and elliptical fin at Reynolds number 436, heat flux of 50 W/cm^2 (23 mm-29 mm from inlet)…….……..……..……..65

Figure 5.10 The effect of performance factor for various angles of elliptical fin arrangement with flow direction for (a) 50 W/cm^2 b) 65 W/cm^2 66

Figure 6.1 Geometry of elliptical fin microchannel (not scaled) (a) 2D view (b) computational domain (c) 3D Microchannel heat sink 69

Figure 6.2 Effect of various parameters on elliptical fin microchannel (not scaled) (i) ellipticity ratio (ii) fin orientation angle (iii) fin height (iv) fin to fin centre distance 70

Figure 6.3 Effect of ellipticity ratio on pressure drop 72

Figure 6.4 (a) pressure variation along the channel length (b) effect of friction factor with Re (c) pressure contours of elliptical fin models and straight fin. 73

Figure 6.5 (a) velocity stream lines of elliptical fin models and straight fin (b) enlarged view of velocity stream lines between fin gaps 75

Figure 6.6 (a) effect of ER and Re on wall temperature (b) effect of ER and Re on Nusselt number (c) temperature contours of elliptical fin models and straight fin. 76

Figure 6.7 Effect of ER and Re on performance factor 77

Figure 6.8 (a) pressure variation along the channel length (b) effect of friction factor with Re (c) pressure contours of elliptical fin models and straight fin. 79

Figure 6.9 (a) effect of fin height and Re on wall temperature (b) effect of fin height and Re on Nusselt number (c) temperature contours of elliptical fin models and straight fin. 81

Figure 6.10 Effect of EFH and Re on performance factor 82

Figure 6.11 (a) pressure variation along the channel length (b) effect of friction factor with Re (c) pressure contours of elliptical fin models and straight fin. 84

Figure 6.12 (a) effect of fin to fin centre distance and Re on wall temperature (b) effect of fin to fin centre distance and Re on Nusselt number (c) temperature contours of elliptical fin models and straight fin. 86

Figure 6.13 Velocity contours of elliptical fin models and straight fin. 87

Figure 6.14 Effect of performance factor on centre distance and Re 87

Figure 7.1 Effect of heat sink material on (a) Nu (b) thermal resistance 90

Figure 7.2 Effect of nanofluids on (a) friction factor (b) Nu. 91

Figure 7.3 Effect of nanofluids in EFMC and SFMC on (a) thermal resistance (b) PF. 92

Figure 7.4 Effect of pure water and CuO-water nanofluid concentrations in EFMC on (a) Pressure drop (b) friction factor (c) temperature contours. 93

Figure 7.5 Effect of pure water and CuO-water nanofluid concentrations on (a) wall temperature (b) Nu in EFMC at different Re (c) temperature contours 95

Figure 7.6 Effect of pure water and CuO-water nanofluid concentrations on (a) pumping power (b) PF in EFMC at different Re. 96

Figure 7.7 Effect of pure water and CuO-water nanofluid concentrations on thermal resistance ratio in EFMC. 97

Figure 8.1 Experimental setup of microchannel heat sink (a) line diagram (b) actual experimental setup 100

Figure 8.2 Exploded view of test section 101

Figure 8.3 Schematic diagram of 3D metal printer 102

Figure 8.4 The 3D printed microchannel heat sinks (a) 3D view (b) enlarged view 103

Figure 8.5 Ultrasonic sonicator 104

Figure 8.6 Various equipments used for measuring properties (a) digital weighing machine (b) thermal conductivity analyzer (KD2 PRO) (c) Brookfield DV2T viscometer (d) nanofluid at different time periods..... 105

Figure 8.7 (a) comparison of thermal conductivity with correlations (b) comparison of thermal conductivity of CuO NF and Al_2O_3 NF..... 107

Figure 8.8 Dynamic viscosity variation with VF 108

Figure 8.9 Effect of pure water and CuO-water nanofluid concentrations on (a) Pressure drop (b) Friction factor in EFMC at different Re (c) experimental and numerical results of water and 1% CuO-water nanofluid..... 112

Figure 8.10 Effect of pure water and CuO-water nanofluid concentrations on (a) Wall temperature (b) Wall and fluid temperature difference in EFMC at different Re. 114

Figure 8.11 Effect of pure water and CuO-water nanofluid concentrations on (a) Nu (b) thermal resistance ratio in EFMC at different Re (c) experimental and numerical results of water and 1% CuO-water nanofluid. 115

Figure 8.12 Effect of pure water and CuO-water nanofluid concentrations on (a) pumping power (b) PF in EFMC at different Re. 116

List of tables

Table 3.1 Details of mesh 19

Table 3.2 The properties of substrate material and nanoparticles. 21

Table 3.3 The properties of substrate material and nanoparticles. 22

Table 4.1 Dimensions of DTMC investigated numerically. 29

Table 4.2 Performance parameters for various width tapered ratios, at height tapered ratio of 3.9 and Re 340……..……..……..46

Table 5.1 Dimensions of SFMC and EFMC were investigated numerically. 52

Table 5.2 Pressure drop % for various EFMC's over SFMC. 54

Table 5.3 Nusselt number enhancement % for various EFMCs over SFMC. 62

Table 6.1 Dimensions of EFMC investigated numerically……..…….71

Table 8.1 3D metal printer specifications.....……..102

Table 8.2 The geometrical dimensions of microchannel heat sink……..103

Table 8.3 Specifications of the nanoparticles……..104

Table 8.4 Uncertainty of measuring instruments…….111

Table 8.5 Uncertainty of estimated data…….111

Nomenclature

A_b	*Channel base area of single channel, (m^2)*
A_s	*Convective surface area of channel, (m^2)*
b_f	*Semi-minor axis of a fin, (m)*
C_p	*Specific heat capacity, (J/kg K)*
D_h	*Hydraulic diameter of channel, (m)*
E_{Nu}	*Effective Nusselt number*
E_f	*Effective friction factor*
f	*Friction factor*
f_{ef}	*Friction factor of elliptical fin*
f_{sf}	*Friction factor of straight fin*
H_{ch}	*Channel height, (m)*
H_Y	*Height tapered ratio*
h	*Convective heat transfer coefficient, (W/m^2 K)*
k	*Thermal conductivity, (W/m K)*
L	*Channel length, (m)*
l_f	*Semi-major axis of a fin, (m)*
N	*Number of channels*
P	*Pressure, (Pa)*
ΔP	*Pressure drop across the channel, (Pa)*

q''	*Total heat flux, (W/m^2)*
q_w''	*Wall heat flux, (W/m^2)*
Q	*Volume flow rate, (m^3/sec)*
Re	*Reynolds number*
S	*Centre distance between fins, (m)*
t	*Channel base thickness, (m)*
T_w	*Wall temperature, (K)*
T_{bf}	*Average bulk fluid temperature, (K)*
ΔT	*Temperature gradient between wall and bulk fluid temperature, (K)*
T_{in}	*Inlet fluid temperature, (K)*
T_{out}	*Out fluid temperature, (K)*
U_{avg}	*Average velocity of fluid, (m/sec)*
W_{ch}	*Channel width, (m)*
W_x	*Width tapered ratio*

Abbreviations

DTMC	*Double tapered microchannel*
MCHS	*Microchannel heat sink*
EFMC	*Elliptical fin microchannel*
SFMC	*Straight fin microchannel*
PF	*Performance factor*
MC	*Microchannel*

Greek letters

ξ	*Thermal resistance ratio*
σ	*Temperature difference ratio*
ψ	*Pumping power ratio*
Δ	*Gradient*
μ	*Dynamic viscosity, (Pa.sec)*
ρ	*Density of fluid, (Kg/m^3)*
κ	*Conductivity of fluid (W/m.K)*
Φ	*Volume fraction*
∇	*Vector differential operator*

Subscripts

Avg	*Average*
b	*Base*
bf	*Bulk fluid*
bnf	*Bulk nanofluid*
ch	*Channel*
dr	*Drift*
ef	*Elliptical fin*
f	*Fluid*
h	*Hydraulic*

in	*Inlet*
m	*Mixture*
nf	*Nanofluid*
out	*Outlet*
p	*Particle*
R	*Ratio*
s	*Surface*
sf	*Straight fin*
sol	*Solid*
S	*Distance*
tot	*Total*
tc	*Thermocouples*
w	*Wall*
x	*Location*

CHAPTER 1

Introduction

1.1 Background

Thermal management is a challenging issue in numerous engineering applications, such as thermal power plants, automotive sector, nuclear power plants, aerospace sector, cooling of batteries, data centres and especially the cooling of microelectronic devices. Most microelectronic devices generate heat, and if this heat energy is not adequately dissipated, it can cause damage to critical components of the device. In earlier days, air cooling technique was used to cool the electronic devices. Due to rapid development in technology, the size of electronic devices is scaling down while their power density is increasing tremendously. The excess heat generated in such miniaturized devices elevates its operating temperature. As a result, the performance may decline and there is a possibility of thermal failure when it is overheated. To meet the present cooling demand, the choice of conventional air cooling method is no more sufficient. Hence, it becomes inevitable to replace air cooling technique. Despite many cooling technologies such as phase change, porous medium, microchannel heat sink, cold plate and thermo-electronic cooling; the microchannel heat sinks are among the best cooling technologies available to dissipate higher heat fluxes. In 1981, Tuckerman and Pease [1] introduced the concept of liquid-cooled microchannel heat sinks. This technology offers several advantages, including a high heat transfer coefficient, a larger surface area to fluid volume ratio, and reduced coolant demand. These benefits result in faster heat transfer rates, ultimately improving the functionality and reliability of electronic devices.

Heat sinks are one of the indirect heat exchanging devices, which extract heat from electronic or mechanical devices and control the temperature of those devices. The heat transfer occurs in heat sinks according to the second law of thermodynamics. These micro heat exchangers are inspired from nature such as human lungs, kidneys, brain and veins, etc.The microchannels are typically parallel micro rectangular passages with hydraulic diameter of less than 0.1 mm [2]. In microchannels, transport of fluid and energy is

governed by surface to fluid volume ratio, fluid properties and shape of channels. Besides, these microchannels require less coolant, due to their compact size (compact heat exchangers). The efficiency of microchannel heat sinks can be enhanced by reducing thermal resistance or increasing heat transfer capacity. This can be achieved by modifying the geometry of microchannel, heat sink material, coolant thermo-physical properties and allowing low temperature fluid through microchannel.

1.2 Microchannel fabrication

The fabrication of complex microchannel geometries on the substrate material with precision is a challenging task for manufacturer. Over the years, various fabrication techniques have been developed based on application and material. The technologies include conventional and non-conventional techniques. Conventional include photolithography, wet and dry etching, micro-machining and embossing and imprinting; non-conventional include laser related machining such as UV- laser micro-machining, IR-laser micro-machining, and micro-machining by short ultrashort pulse laser and 3D printing. Non-conventional techniques make fabrication easier and more precise compared to conventional techniques. The simple rectangular microchannel can be fabricated using any of these techniques. But complex geometries like wavy, curved and wavy with branches are fabricated using laser related fabrication or 3D printing without compromising precision.

1.3 Heat sink material

Heat sink material also plays an important role in electronic cooling. High thermal conductivity material can conduct heat quickly to coolant fluid. For microchannel heat sink, numerous kinds of materials have been used such as copper, aluminum and silicon. The selection of heat sink material depends on application. Aluminum is one of the most widely used heat sink materials due to low cost, easy fabrication and has good thermal conductivity. However, high thermal conductivity materials like copper and silicon used in applications in which high heat flux removal is the main criterion.

1.4 Coolants

The fluid which absorbs heat from the microchannel walls is called as coolant fluid. Heat carrying capacity of the coolant fluid is influenced by its specific heat, thermal conductivity, viscosity, and mass flow rate of fluid. The heat carrying capacity can be increased by selecting high thermal conductivity, large specific heat, high mass flow rate and low viscous fluid. In general, higher specific heat and thermal conductivity result in greater heat carrying capacity, and vice versa. The most frequently used coolants for microchannel heat sink include air, water, ethylene glycol, refrigerants and oils. Over time, hybrid coolants (such as air, water, fluoro-chemicals, water plus ethylene glycol, etc.) replaced traditional coolants due to the increased heat-carrying ability.

1.4.1 Nanofluids

The conventional cooling fluids used in microchannel such as air, water and fluoro-chemicals etc., have low thermal conductive fluids with limited heat transfer performance. To dissipate high heat fluxes, it necessary to develop high thermal conductivity fluids in order to enhance heat transfer properties. In 1873, Maxwell proposed the novel concept of blending solid particles with base fluids. The suspension of micrometer, millimetre sized solid particle to the base fluid enhances the thermal conductivity but it leads to severe issues like clogging, erosion and increase of pressure drop. However, this idea could not bring any significant improvement in the heat dissipation due to its draw backs. Recent developments in manufacturing methods and nanotechnologies have enabled the production of extremely small or nano-sized particles, which address the aforementioned issues. With these advanced techniques, a novel cooling fluid called nanofluid was developed by Choi et al. [3] at the Argonne National Laboratory. The phrase "nanofluid" refers to a mixture of nano-sized metallic or non-metallic particles with a base fluid like water, ethylene glycol, or oil. In this, heat is transferred by Brownian motion and interactions of nanoparticles dispersion in the base fluid.

The key benefits of employing nanoparticle in base fluid are:

- Enhanced heat transfer area, due to availability of larger surface area between nanoparticles and fluid.
- Pumping power requirements for the same heat transfer are lower compared to conventional fluids.
- There is low particle clogging than in traditional slurries.
- High dispersion stability is possible.
- Thermal transport properties (thermal conductivity, viscosity and specific heat) can be adjusted by nano particle concentration, material, shape and size to meet the needs of the application.

In light of this, a large number of researchers have been attracted to the use of nanofluid in various engineering applications like biomedical, nanodrug delivery, turbine blade cooling, nuclear reactors cooling and microelectronic cooling etc., In general, metals (Cu, Al, Zn, Ni, Si, and Fe), metal oxides (CuO, ZnO, Al_2O_3, TiO_2, SiO_2 and Fe_2O_3) carbon nanotubes and graphene nanoplatelets etc. are widely used in nanofluid preparation. These highly conductive fluids are more favourable to transfer heat at a faster rate. Figure 1.1 provides information regarding the thermal conductivity of several materials [3], [4]. Further, thermal conductivity of nanofluid is also influenced by particle volume fraction, size of particle, particle shape, type of conventional fluid, temperature, additive, and P_H value.

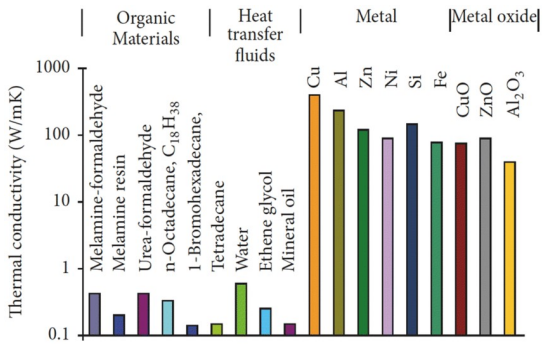

Figure 1.1 Thermal conductivity of different materials (Reference from [3], [4])

1.5 Applications of microchannel heat sinks

Microchannel heat sinks are widely used in various industries due to their superior heat transfer capabilities compared to traditional heat sinks. These industries include HVAC systems, bioengineering, photovoltaic thermal systems, automotive industry, gas turbine blade cooling, optics and lasers, and electric vehicle battery cooling. In bioengineering, microchannel heat sinks are used to regulate temperatures in lab-on-a-chip devices for medical diagnostics and research.

In addition, the combination of microchannel heat sinks with nanofluids has shown even more significant improvements in heat transfer performance. The nanofluids have been shown to exhibit enhanced thermal conductivity and convective heat transfer properties compared to traditional fluids, making them promising candidates for improving thermal management in these industries. Using nanofluids in microchannels can lead to substantial reductions in thermal resistance and increased heat transfer rates, making this combination particularly beneficial for applications where thermal management is critical, including electronic cooling and thermal energy systems.

1.6 Motivation

The following are some of the points that motivated this work:

- In recent years, there has been a significant shift in technology toward compact and miniaturized devices, which have resulted in a significant increase in the heat flux associated with such devices and compelled the need for improvement of heat dissipation.
- At present, air cooling heat sink is one of the most extensively used thermal management techniques. With the advent of miniaturized and compact devices with a high power density, this cooling approach is no longer adequate. Due to the limited heat conductivity and heat capacity of air, this technology is incapable of dissipating high heat flux in an effective manner.
- Literature reviews suggest that microchannel geometry with single phase liquid cooling and two phase liquid cooling has great potential to become a future thermal management technology due to its fast response, high convective heat transfer coefficient and high specific heat of liquids.
- Recently, there has been an increase in focus on the use of nanofluids in conventional rectangular microchannel heat sinks to cool microelectronic devices. This is due to the ease of fabricating complex microchannel geometries and production of nanoparticles using advanced fabrication techniques. Despite these merits, there have been few investigations conducted on complex microchannel heat sinks with the use of nanofluids.

The motivation points listed above were used to frame the following objectives, which are presented in the subsequent section

1.7 Research objectives

A. Several researchers have investigated different types of microchannel to improve the thermal performance, and they have been successful in achieving this goal through varying the geometries. However, identifying the most efficient microchannel geometry that enhances heat transfer performance remains a challenging area of research. **Thus, this study aims to identify an efficient microchannel geometry (including rectangular, double-tapered, and elliptical fin microchannels) that can improve heat transfer performance and provide valuable insights about geometrical configuration of microchannel heat sinks.**

B. To analyze the performance of new microchannel, parametric analysis can be done by varying one or more parameters and observing the corresponding changes in flow and heat transfer behavior. This process helps to identify the optimal design parameters which can enhance thermal performance. **Thus, this study is extended to numerically examine the impact of several design parameters, including ellipticity ratio, fin orientation angle, fin height, and fin-to-fin center distance, on the thermal performance of elliptical fin microchannel heat sinks.**

C. Nanofluids are tailored fluids that exhibit exceptional thermal conductivity and convective heat transfer properties compared to conventional fluids. As a result, they are a promising option for improving thermal management across various applications. When nanofluids are using with microchannel heat sinks, can produce greater improvement in heat transfer performance. **Thus, this study further aims to investigate the impact of nanofluid on thermal performance of optimal elliptical fin microchannel heat sinks using both experimental and numerical methods, as well as to determine the ideal range of Reynolds numbers and nanofluid volume fractions for achieving maximum thermal performance.**

1.8 Outline of the thesis

- Chapter 1 provides a quick overview of microchannel heat sinks and nanofluids, as well as the impact of nanofluids on microchannel heat sinks.
- Chapter 2 contains a complete review of literature relevant to the current study. This is followed by the motivation for research and research objectives. In addition to this, the applications of the research work have also been included.
- Chapter 3 presents geometry modeling, grid generation, grid independence study, assumptions considered in present numerical study, numerical scheme for simulation and validation of numerical procedure with experimental results.
- Chapter 4 presents numerical analysis of three geometrical microchannels of straight, double taper and elliptical fin microchannels in steady-state laminar zone.
- In Chapter 5 the effect of elliptical fin orientation on thermal performance and the fluid flow behaviour in steady state laminar zone is thoroughly investigated.
- Chapter 6 discusses the influence of important parameters, like fin ellipticity ratio, fin orientation angle, fin height and fin to fin centre distance on thermal performance of elliptical fin microchannel heat sink in steady state laminar zone.
- Chapter 7 describes numerical investigation of the effect of heat sink material, nanofluids and nanofluid concentration on flow parameters and thermal performance of optimal elliptical fin microchannel heat sink.
- Chapter 8 deals with experimental investigation of the effect of CuO/water nanofluid concentration on flow parameters and thermal performance of optimal elliptical fin microchannel heat sink.
- Chapter 9 includes general conclusions and future scope.

1.9 Closure

The chapters clearly outline the background, applications, and motivation for the research topic addressed in the current thesis. It also documents significant features of all the chapters, which provides clear idea to the reader.

CHAPTER 2

Literature survey

This chapter provides a brief overview of current research on microchannel heat sinks, highlighting significant contributions from both experimental and numerical studies, and various techniques used to improve their thermal performance. The chapter is divided into five parts, beginning with a discussion on straight fin microchannels and followed by detailed discussions on the effect of extended surface in second part, the third and fourth parts covers channel cross-sectional area, fin geometry, and the fifth part discusses effect of nanofluids in microchannels. Each part has been discussed in detail.

2.1 Straight microchannel

Tuckerman and Pease [1] first introduced the concept of microchannel (MC) heat sinks. They demonstrated that the microchannel heat sinks were effectively dissipating higher heat fluxes compared to conventional channels. They used silicon wafer to fabricate parallel micro rectangular channels with wall width of 57 μm and channel height of 365 μm. The heat sink kept substrate temperature below 110 ^{o}C and dissipated high heat flux of 790 W/cm^2. Furthermore, they revealed that these microchannel heat sinks exhibit better heat transfer coefficients for laminar flow than for turbulent flow. Subsequently, many researchers have focused on microchannel heat sinks to evaluate their effect on heat transfer and flow behavior, and have found significant differences between experimental results and classical theory. The deviation between the experimental results and classical theories was due to experimental uncertainty, entrance and exit effects, surface roughness, axial conduction effects, and viscous heating effects. To resolve the discrepancies, Liu and Garimella [5] carefully designed experiments and found good agreement with conventional theory. They suggested that classical theories used for conventional passages can be successfully implemented to microchannels and minichannels as well. Mehendale et al. [2] classified small channels based on channel dimensions; this classification divides the range from 1 μm to 100 μm as microchannels, 100 μm to 1 mm as meso-channels, 1mm to 6mm as compact passages, and > 6 mm as conventional passages. Later, Kandlikar et al. [6], [7]

modified the classification based on hydraulic diameter, with a range from ≤ 0.1 μm as nanochannel, 0.1 μm to 1 μm as Transitional nanochannel, 1 μm to 10 μm as transitional microchannel, 10 μm to 200 μm as microchannel, 200 μm to 3 mm as minichannel, and > 3 mm as conventional passages.

In subsequent studies, Lee et al. [8] & Mudawar et al. [9] experimentally and numerically investigated the thermal performance of three dimensional rectangular microchannels. Their results revealed that the numerically evaluated pressure drop and temperature distribution were in good agreement with experimental data (with maximum deviation of 5 %). Hence, numerical simulations were used to estimate the thermal performance of heat sink to reduce the cost of experiments. For instant, Prajapati et al. [10] analyzed the effect of fin height on cooling performance in conventional straight fin microchannels (SFMC). They found that increasing the fin height improves cooling performance, and they also found the optimal space between the cover plate and fin to further enhance cooling performance. Another set of researchers Zahhad et al. [11] studied the influence of stepwise varying width of MC and found that the local wall temperature decreased by increasing channel width.

Later, many researchers attempted various techniques to boost thermo-hydraulic performance of conventional SFMC by varying geometrical parameter [12], [13] (aspect ratio and channel length), surface texture [14], by changing working fluid as two phase fluid [15], [16], manifold design [17], [18], using hydrophilic and hydrophobic surfaces [19], [20]. For example, Kumar et al. [21] investigated the effect of channel aspect ratio of rectangular microchannel heat sink on thermal performance. Their results revealed that decreasing channel aspect ratio or increasing channel height is more advantageous for augmenting thermal performance. However, cooling performance of conventional SFMC is limited due to inefficient fluid mixing and incremental boundary layer thickness along the stream. As a result greater temperature variations existed within the heat sink from inlet to outlet.

2.2 Effect of extended surface in conventional channel

To improve the heat transfer capabilities of conventional SFMC, researchers have studied the effect of various extended surfaces in the channel, including ribs [22], grooves [23], dimples [24], combination of ribs and grooves [25]–[27], ribs and chamber [28], [29] and various shaped baffles [30] to induce efficient fluid mixing in conventional SFMC. Wang et al. [31] introduced bidirectional ribs such as vertical ribs and span wise ribs to disrupt the thermal boundary layer and to generate recirculation in both vertical and span wise directions. These bidirectional rib microchannel (BR-MC) were compared with vertical rib (VR-MC) and span wise rib microchannel (SR-MC) for a Re range of 100-1000. Their results revealed that BR-MC Nusselt number was found to be 1.4-2 and 1.2-1.42 times greater than VR-MC and SR-MC respectively with significant pressure penalty. Recently, Kumar and Pankaj [32] examined the thermal performance of three distinct configurations of arc grooves in rectangular MCs: grooves on side walls, grooves on floor wall, and grooves on both side walls and floor wall compared with simple SFMC. Their results showed that addition of grooves on both side walls and floor wall augmented the Nusslet number to 119 % over simple SFMC but it incurred greater pressure penalty. In addition to this, parametric study [32], [33] was also carried out to optimize the thermal performance. Although extended surfaces enhanced thermal performance, there was a significant pressure drop in the channel.

2.3 Effect of microchannel cross sectional area

Modifying the microchannel cross-sectional area is a viable approach to enhance heat transfer, and various geometrical configurations, such as rectangular, triangular, trapezoidal, and wavy shapes, were examined by altering the channel shape [34]–[37]. For instant, Liangbin et al. [38] analyzed the local heat transfer coefficient of an elliptical cross-sectional channel at a constant wall temperature in the laminar flow region. They investigated a range of channel aspect ratios (0.2-1) and Re (25-2000) and found that the local heat transfer was highly sensitive to lower Re (Re<250). Furthermore, they concluded that the aspect ratio had a negligible impact on local heat transfer. The wall temperature and thermal performance were significantly affected by the flow cross-sectional area and its variation in the stream-wise and span-wise directions. Hung and Yan [39] numerically

investigated the individual effects of width tapered ratio and height tapered ratio on thermal performance of heat sink at a constant pumping power condition. They found that the width tapered channel showed lower wall temperature and greater uniformity of temperature distribution compared to the height tapered channel. Also, there was a 16.7% enhancement in thermal performance for the width tapered channel design over the conventional straight channel. In subsequent study, Hung et al. [40], examined three different microchannel configurations, namely; single layer, double layer and tapered channels, and compared them with parallel rectangular channel. Out of all configurations, the taper channel exhibited better thermal performance and showed uniform temperature distribution. Later, Duryodhan et al. [41], [42] experimentally and numerically investigated the flow and thermal characteristics of converging microchannel. Hydraulic diameter of 156 μm, mass flux of 113–1200 kg/m^2-s with converging angle of 8° in the range of Re - 30 to 274, was investigated and the results were compared with diverging microchannels of similar dimensions. They found that converging microchannels have 35 % higher heat transfer coefficient than diverging microchannels. Similarly, authors [43], [44] attempted to reduce the flow cross-sectional area along the stream wise direction by using converging flow channels. In a converging channel [45], the velocity of the fluid is accelerated as it flows from the inlet to the outlet, leading to an increase in the convective heat transfer coefficient. This, in turn, led to enhanced heat transfer and a considerable reduction in wall temperature. As a result of the reduced wall temperature with converging flow, the local wall temperature dropped, and the overall temperature distribution in the heat sink became more uniform. For example, Dehghan et al. [45] also investigated the influence of width tapering under three different pressure conditions. Their study revealed that width tapered ratio of 0.5 showed reduction of pumping power by a factor of 4 when compared to straight microchannel at pressure condition of 3000 Pa. Vafai and Zhu [46] designed a double layer microchannel with contour flow to solve issues related to temperature non-uniformity and pumping power. They put a significant amount of effort to improve the thermal performance of double layer microchannel by varying geometrical parameters [40], [47], [48] like aspect ratio, channel width ratio, channel numbers and base thickness. As a result of their study, an increase of temperature and pressure drop over the length of the channel was considerably reduced compared to straight microchannels. Later, Osanloo et al. [49] used a heat sink with taper on

both lower and upper channels in double layer microchannel to analyse cooling performance for different fluid flow rates and convergence angles. Their results revealed that increased volume flow rate of cooling fluid reduces the bottom wall temperature and thermal resistance. They also found that optimal values of thermal resistance and uniformity of temperature distribution occurred at 4° convergence angle. Wang et al. [50] investigated hydrodynamic behaviour and thermal performance of periodic transversal elliptical fin microchannel (EFMC) under laminar flow region. Their findings revealed that the cooling performance of the transversal EFMC was better than that of SFMC. Hence, it can be concluded that altering the flow cross sectional area enhanced thermal performance, but there was a significant increase in pumping power requirement to pump the fluid through the channel.

2.4 Effect of microchannel fin geometry

Another group of researchers focused on fin geometry to enhance thermal performance by inducing flow separation and thermal boundary layer re-initialization [51]. For instant, Lee et al. [33] experimentally and numerically studied the effect of oblique fins on flow and heat transfer characteristics in laminar flow region (Re 250-780). The oblique fins were machined on copper plate of 25 mm × 25 mm cross section. The length of oblique fin was 1500 μm, channel width 500 μm, and oblique angle 27^{o}. The pitch between two successive fins was maintained at 2000 μm. When the working fluid water passes these oblique fins; at trailing edge the flow get separated into two streams: main flow stream and secondary stream. The secondary streams disrupt the boundary layer development and promote better mixing in the channel. Furthermore, boundary layer restarts at the leading edge of each fin. Hence, overall thermal performance of oblique fin MC was enhanced. The maximum heat transfer enhancement (in terms of Nusselt number) was recorded as 103 % over SFMC with acceptable pressure drop penalty. Moreover, significant wall temperature reduction (23 %) was observed over conventional SFMC. In their subsequent studies[52], the influence of oblique fin parameters such as oblique angle (27^{o} and 45^{o}), channel width (100 μm and 200 μm) and oblique fin pitch (400 μm, 800 μm and 1500 μm) was investigated. These studies show that small oblique fin angle and small fin pitch with narrow channel are preferable for enhancing thermal performance. To further improve the

thermal performance. Panse and Ekkad [53] arranged the oblique fins at alternatively offset direction about the centerline in the transverse direction. The influence of such oblique fin arrangements was analysed numerically for better results. Their findings reveal that the structures generated strong counter-rotating vortices due to the serpentine nature of flow from one secondary channel to other. Furthermore, optimal parameters were also determined in order to achieve best performance. Irmawati et al. [54] numerically and experimentally analyzed the feasibility oblique fin MC in electrical vehicle battery cooling application. Their results found that liquid cold plate with oblique fin held the battery surface temperature below its working temperature of 50^{o} C. Hence it could be a viable option for battery cooling.

Yogesh et al. [55] used different orientation angles (0^{o} -50^{o}) and ellipticity ratio (0.6, 0.7 and 0.8) of elliptical mini fin tube heat exchanger for transitional flow regime (1300-1600) using air as cooling medium at constant wall temperature of 300K. Their findings showed that the heat transfer capabilities of elliptical fin tubes were enhanced over circular tube heat exchangers. This can be further enhanced with decrease in ellipticity ratio. Another important finding was friction factor, which was reduced to 52.9 % with 0.6 ellipticity ratio over circular fin tube heat exchanger. Deshmukh and Warkhedkar [56] employed mixed convection technique to enhance thermal performance of the elliptical mini pin fin heat sink. Optimal design parameters were also evaluated by varying transverse pitch, longitudinal pitch and fin arrangement in presence of air as cooling medium at heat flux of 1.48 W/cm^2. The results implied that an increasing transverse and longitudinal pitch led to better fluid mixing and showed 24 % higher heat transfer than circular pin fin heat sink. It was also found that there was 63 % more effective heat transfer with staggered elliptical fin over inline elliptical fin arrangement. Amer et al. [57] designed and analyzed five mini pin fin heat sinks and compared them with unpinned heat sink to predict heat transfer and fluid flow characteristics numerically, by maintaining constant flow area at inlet of fin. The five designs were: circular, square, strip, triangular and elliptical pin fin. They concluded from the results that elliptical pin fin showed the best hydrothermal performance compared to other pins due to no sharp edges and more aerodynamic profile shape of the elliptic pin fin. Similarly, Subash et al. [58] numerically analyzed the thermal performance of four different micro pin fin shapes; square, hexagon, circular and elliptical fin for various

flow velocities at a heat flux of 20 W/cm^2, by maintaining constant heat transfer surface area. They used water as a cooling fluid in their study and found that square fin showed best thermal performance among all other fin shapes. Nevertheless, the elliptical fin showed minimum pressure drop with fairly better thermal performance. Their consequent studies [59] were focused on variable axial distance between pin fin (1000 μm - 1600 μm) and staggered elliptical fin layouts to improve cooling characteristics. They considered four different layouts of elliptical fin heat sink such as case i. inline elliptical fin, case ii. elliptical fins arranged in serpentine manner, case iii. alternative pin fins located in the center of MC and near the walls, and case iv .alternative pin fin divided into two halves and located adjacent to the walls with convex part of pin fin facing each other. Among all the layouts, elliptical fins arranged in serpentine manner showed best cooling performance with a little higher pressure penalty than other pin fins. This was further improved by increasing variable axial distance between fins due to the converging and diverging flow effect. The spawned studies [60], analysed the effect of elliptical pin fin height (300 μm, 400 μm and 500 μm) and fin orientation angles ranging from 20º - 80º with an increasing step size of 20º. According to their findings, the greatest heat transfer coefficient was seen when a 400 μm height elliptical fin was oriented at 20º to the flow direction.

2.5 Effect of nanofluids on microchannel heat sinks

Nanofluids in microchannels have received considerable attention from researchers in recent years. The use of nanofluids in microchannels leads to improved thermal performance due to the enhanced heat transfer characteristics of the fluid that of water. It is also observed from the literature that the past two decades have witnessed a considerable amount of research on nanofluids. However, the research on nanofluids has mainly focused on their thermo-physical properties. Some of the review articles addressed thermo-physical properties of nanofluids [61]–[64]. In recent times, nanofluids in conventional microchannel have grabbed attention [65]–[70] and are successfully used in place of conventional fluids. In this context, some of the most significant contributions from the literature are discussed here. Chein et al. [71] studied heat transfer and flow characteristics in a silicon microchannel heat sink with nanofluid. In their analysis, nanofluids were considered as a single phase, and particle random motion was accounted as well. The research revealed that

the addition of nanoparticles to a base fluid improves thermal conductivity and heat transfer rate with minimum pressure drop. Ghasemi et al. [72] numerically examined the impact CuO water nanofluids on heat transfer using single phase and two phase methods and compared them with experimental results. The numerical results revealed that two phase approach was closer to experimental results than single phase methods. Azizi et al. [73] conducted experiments on a cylindrical microchannel heat sink consisting of 86 microchannels with a hydraulic diameter of 526 μm. The study investigated the effect of Cu-water nanofluid with varying volume fractions under laminar flow condition. They found a significant decrease in convective thermal resistance at a mass fraction of 0.3% wt and a Reynolds number of approximately 600. Additionally, the researchers developed a new correlation for predicting Nusselt number and friction factor by taking into account the volume fraction of the nanoparticle, in addition to Reynolds number and Prandtl number. The proposed correlations concur well with experimental values with deviations of ±10 %. Jang and choi [74] numerically examined the performance of micro channel heat sink with nanofluid. They considered three different types of coolants in their study: water, water based diamond nanofluid (1vol %, 2 nm) and copper nanofluid (1vol %, 6 nm) and compared the cooling performance of micro channel heat sink. The result shows that micro channel heat sink with diamond based nanofluid improving heat transfer rate higher than other two fluids. Further, there was reduction of temperature of micro channel wall. Jung et al. [75], [76] conducted an experiment on a rectangular microchannel heat sink using Al_2O_3 as a nanofluid in laminar flow regime .They selected nano particles of size 170 nm and studied the effect of nano particle volume fraction (0.6 - 1.8 %) on convective heat transfer coefficient and friction factor. The results indicated that the convective heat transfer coefficient increased up to 32 % compared to pure water at 1.8 % volume fraction, without major friction loss. Ghazvini et al. [77] compared the effect of channel aspect ratio, porosity and variation of volume fraction on heat transfer of micro channel heat sink in presence of CuO nanofluid in two different approaches namely fin model and porous medium approaches. Mohammed et al. [78] elucidated the influence of Al_2O_3-H_2O on MCHS and found that augmentation of convective heat transfer occurs with increase in flow rate. Moreover, it increases with an increase of volume concentration. Recently, Peyghambarzadeh et al. [79] investigated the performance of MCHS using two different

types of nanofluid, namely CuO and Al_2O_3. They found that CuO based nanofluid is more prone to deposition compared to Al_2O_3 nanoparticle. But from a heat transfer rate point of view, CuO nanofluid was more efficient than Al_2O_3. Helin et al. [80] numerically investigated the effect of Koch fractal baffle structures and nanofluid volume fractions on heat transfer and flow resistance. The result showed that, the most effective arrangement was found to be the staggered distribution of baffles, which led to a maximum increase of 3.32 times in Nu within the Re range of 100-1000, as well as a 1.79 times reduction in flow resistance. Moreover, the study revealed that the combined heat transfer performance of nanofluids outperformed that of deionized water for Re values ranging from 100-439. Sakanova et al. [81] conducted a significant numerical study to investigate the impact of nanofluid on wavy microchannels. The results indicated that the wavy microchannels exhibited better performance compared to regular rectangular microchannels when water or nanofluid was used as a coolant. The study analyzed the effect of volume flow rate, wave amplitude, and wave length on pressure drop and thermal resistance. It concluded that pressure drop had an inverse relation with wavy length. But it had direct relation with volume flow rate and amplitude of wave. Furthermore, thermal resistance decreases with increase of volume flow rate and amplitude of wave.

Since then, several authors have conducted experimental and numerical analysis on microchannel heat sinks to enhance the performance and dissipate high heat flux from electronic devices. In the literature numerous research articles on various microchannel geometries are available. However, research on complex microchannel designs with nanofluid is still scarce. Therefore, in this study, a detailed investigation of Double tapered and elliptical fin microchannel has been done to evaluate heat dissipation and fluid flow characteristics. Furthermore, the influence of various parameters on elliptical fin microchannel heat sink such as ellipticity ratio, fin orientation, channel depth and fin to fin centre distance have been numerically analysed to understand the fluid flow and heat transfer characteristics in the range of Re 100 to 780 and higher heat flux range of 50 -100 W/cm^2. Apart from the geometrical design of the microchannel, an addition of nano particle range of 0 to 1 % volume fraction to the cooling fluid and its effect on the heat transfer rate and pressure drop have also been analyzed. Finally, the conclusions and summaries are presented based on findings obtained.

CHAPTER 3

Approach and Methodology

There are basically three ways to analyze microchannel heat sinks: analytical, numerical, and experimental, which vary in cost, accuracy, and complexity. The numerical approach is relatively inexpensive and provides precise results (close to experimental results) by utilizing mathematical models and computer simulations. On the other hand, the analytical method relies on mathematical equations to derive solutions, but it may not accurate for complex geometries and boundary conditions. The experimental approach involves physical experiments that can be time-consuming and expensive. A combination of numerical and experimental analysis is usually used to optimize the design of the heat sink and enhance its thermal performance. In present study, Numerical analysis was carried out initially to determine the optimal geometrical dimensions of microchannel. Later, experimental approach was used on to the optimized parameters for determining the thermal performance of the heat sink.

3.1 Geometrical models

In the present study, various microchannel geometrical designs were used for numerical investigations, namely: straight fin microchannel (SFMC), double tapered microchannels (DTMCs), elliptical fin microchannel (EFMC), optimal elliptical fin microchannels (OEFMC). Then, the optimal elliptical fin microchannels were explored numerically and experimentally, employing nanofluid as the coolant. The geometrical models were developed in SOLIDWORKS; meshing and analysis were carried out through ANSYS FLUENT software.

3.2 Grid refinement

The computational domains were meshed with hexahedral elements. Final grid size was determined by grid independence test to reduce the computational time without compromising the accuracy in the solution. A detailed grid independence analysis was performed for 4º EFMC, in which three different element sizes of coarse, medium, and fine (0.049 mm, 0.039 mm, and 0.029 mm) were compared at an inlet velocity of 0.5 m/s and

temperature 293 K (shown in Figure 3.1). The calculated average Nusselt numbers for these grid sizes are as 22.39, 22.74, and 22.94 respectively (as given in Table 3.1). The percentage reduction in Nusselt number for coarse to medium grid size is 1.5 %, and on further refining grid size, the Nusselt number reduces to 0.87 %. This marginally increases the computational time. Hence, medium grid size was used for the present numerical study to save computational time. Similarly, grid independence analysis was done for the remaining cases also.

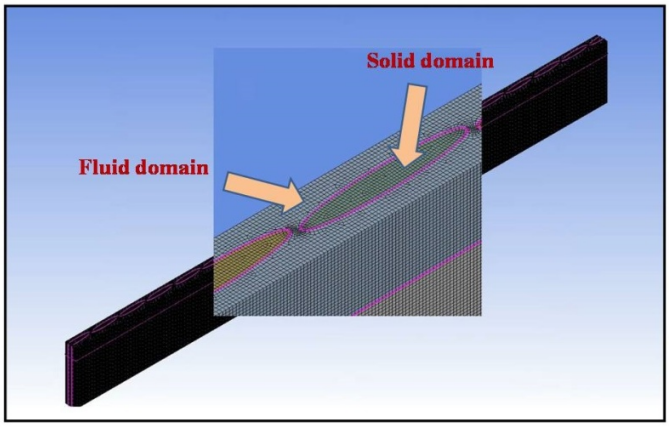

Figure 3.1 The meshing of elliptical microchannel

Table 3.1 Details of mesh

Type of Mesh	Mesh divisions	Element size (mm)	No. of elements	Nu	Variation
Coarse	1020×20×30	0.049	11440743	22.39	-
Medium	1282×25×38	0.039	19851894	22.74	1.5 %
Fine	1724×34×51	0.029	40683028	22.94	0.87 %

3.3 Numerical schemes for single-phase

In single-phase, finite volume based solver ANSYS FLUENT was used to solve the governing equations. The SIMPLE scheme was selected for pressure and velocity coupling

and second order upwind scheme was employed for pressure discretization. Similarly, the momentum and energy equations were solved with the help of second order upwind scheme. In the conjugate simulation, uniform velocity and pressure boundary conditions were applied at inlet and outlet of the channel respectively. Simultaneously, uniform heat flux was implemented at the bottom wall of the channel and no-slip condition was applied on all inner walls of channel. A uniform mesh density was opted for solid as well as fluid domain. A residue of 10^{-6} was selected as convergence criteria for continuity, momentum and energy equations.

3.4 Numerical schemes for two-phase

Two-phase mixture model was adopted to solve the conjugate heat transfer problem. The SIMPLE scheme was selected for pressure and velocity coupling and second order upwind scheme was employed for pressure discretization. Similarly, the momentum and energy equations were solved for the mixture and a volume fraction equation is used for the secondary phases. In the conjugate simulation, uniform velocity and pressure boundary conditions were applied at inlet and outlet of the channel respectively. Simultaneously, uniform heat flux was implemented at the bottom wall of the channel and no-slip condition was applied on all inner walls of channel. A uniform mesh density was opted for solid as well as fluid domain. A residue of 10^{-6} was selected as convergence criteria for continuity, momentum energy equations and 10^{-2} for volume fraction equation.

3.5 Assumptions

A three-dimensional conjugate heat transfer model was used to analyze the heat transfer and fluid flow characteristics of microchannel designs, which account for convective heat transfer in fluid and conductive heat transfer in solid substrate.

To simplify the analysis, the numerical study uses the following assumptions.

- Flow is steady and laminar.
- The fluid is incompressible and velocity is uniform at the inlet of the channel.
- No internal heat generation.
- Gravitational effects are neglected.

- Channel material is homogeneous and isotropic.
- Thermo-physical properties of cooling fluid and heat sink material are temperature. Independent except thermal conductivity and viscosity of the fluid.
- No radiation heat transfer.
- No-slip velocity at channel walls.

In this analysis, water and nanofluid were used as cooling fluid, and their thermal conductivity and viscosity were a function of temperature. Furthermore, heat sink and coolant properties are given below [82] [83].

Table 3.2 The properties of substrate material and nanoparticles.

Property	**Property dependent equations**	**Units**
Density [83]	$\rho(t) = \frac{a_0 + a_1 t + a_2 t^2 + a_3 t^3 + a_4 t^4 + a_5 t^5}{1 + bt}$	kg/m^3
Thermal conductivity [83]	$k(T) = -0.58166 + 6.33555 \times 10^{-3} T - 7.9643 \times 10^{-6} T^2$, $W/m.K$	$W/m.K$
Viscosity [83]	$\mu(T) = 2.414 \times 10^{-5} \times 10^{\frac{247.8}{(T-140)}}$	$N.s/m^2$

Where, the constant values are

$$a_0 = 999.8396 \quad a_4 = 1.49756 \times 10^{-7}$$

$$a_1 = 18.22494 \quad a_5 = -3.93295 \times 10^{-10}$$

$$a_2 = -7.92221 \times 10^{-3} \quad b = 1.81597 \times 10^{-2}$$

$a_3 = -5.54485 \times 10^{-5}$ t and T has the units of °C and K respectively

Table 3.3 The properties of substrate material and nanoparticles.

Property	Density (ρ)	Specific heat (C)	Thermal conductivity (k)
	kg/m^3	$J/kg.K$	$W/m.K$
Substrate : Copper	8978	381	387.6
Substrate : Steel alloy 17-4PH	7750	460	18.3
Nanoparticles: Cu	8900	385	400
Nanoparticles: Al_2O_3	3970	765	37
Nanoparticles: CuO	6300	553	69

3.6 Governing equations

3.6.1 Single phase fluid

The governing equations solved over computational domain are as follows

Continuity equation for fluid zone:

$$\nabla.(\rho\vec{v}) = 0 \tag{3.1}$$

Momentum equation for fluid zone:

$$\nabla.(\rho\vec{v}\vec{v}) = -\nabla P + \nabla.(\mu\nabla\vec{v}) \tag{3.2}$$

Energy equation for fluid zone:

$$\nabla.\left(\rho\vec{v}C_pT\right) = \nabla.(k\nabla T) \tag{3.3}$$

Energy equation for solid zone:

$$\nabla.(k\nabla T) = 0 \tag{3.4}$$

3.6.2 Two phase fluid

The governing equations solved over computational domain are as follows

Continuity equation for fluid zone:

$$\nabla.(\rho_m \overrightarrow{v_m}) = 0 \tag{3.5}$$

Momentum equation for fluid zone

$$\nabla.(\rho_m \overrightarrow{v_m}\overrightarrow{v_m}) = -\nabla P + \nabla.[\mu_m(\nabla\overrightarrow{v_m} + \nabla\vec{v}_m^T)] + \rho_m g - \nabla.\left(\sum_{k=1}^{n} \emptyset_k \rho_k \vec{v}_{dr,k}\vec{v}_{dr,k}\right) \tag{3.6}$$

Energy equation for fluid zone

$$\nabla.\sum_{k=1}^{n} \emptyset_k \rho_k \vec{v}_{,k} T_{Cp,k} = \nabla.(k_m \nabla T) \tag{3.7}$$

Volume fraction equation

$$\nabla.\left(\emptyset_p \rho_p \vec{v}_m\right) = -\nabla.\left(\emptyset_p \rho_p \vec{v}_{dr,p}\right) \tag{3.8}$$

The symbols ρ, v, μ, Φ, and k represent density, velocity, viscosity, volume fraction, and thermal conductivity of the fluid, respectively. The suffix 'm' denotes mixture, 'p' denotes particles, and 'dr' denotes drift.

3.7 Data reduction

In this section, the equations used to calculate fluid flow and cooling performance of microchannel heat sink (MCHS) is presented.

a. Hydraulic diameter (D_h)

$$D_h = \frac{4 \times W_{ch,i} \times H_{ch,i}}{2\left(W_{ch,i} + H_{ch,i}\right)} \tag{3.9}$$

Where, $W_{ch,i}$= width of single channel, $H_{ch,i}$ =height of the channels

b. Reynolds number (Re)

$$Re = \frac{\rho u_{avg} D_h}{\mu} \tag{3.10}$$

Where, μ is dynamic viscosity of fluid, D_h, u_{avg} and ρ are hydraulic diameter of channel, average fluid velocity and density of fluid flowing through the microchannel respectively.

c. Average Nusselt number $(Nu)_{avg}$

$$Nu_{avg} = \frac{h \times D_h}{k} \tag{3.11}$$

Similarly, heat transfer coefficient and wall heat flux were evaluated using the following equation

$$h = \frac{q_w^{''}}{(T_w)_{avg} - (T_{bf})_{avg}} \tag{3.12}$$

$$q_w^{''} = \frac{q^{''} \times A_b}{N \times A_s} \tag{3.13}$$

Here 'h' and 'k' indicate convective heat transfer coefficient and thermal conductivity of fluid. The total heat flux appliedq'', at the base of the channel, $q_w^{''}$heat convection from inner bottom and sidewalls of channel. Other parameters like A_b is area of bottom wall, $A_s$is sum of surface areas of bottom and sidewalls of channel and N is number of channels.

Average bottom wall temperature $(T_w)_{avg}$=$\frac{\sum_{x=1}^{n} T_{wx}}{n}$ (3.14)

Local bottom wall temperature$(T_w)_x$ was evaluated at n locations with incremental length of one unit.

Average bulk fluid temperature $(T_{bf})_{avg}$=$\frac{\sum_{x=1}^{n} T_{fx}}{n}$ (3.15)

Local bulk fluid temperature $(T_{bf})_x$ was evaluated at n locations with an incremental length of one unit.

Local Nusselt number (Nu_x) is evaluated at x location.

$$Nu_x = \frac{h_x \times D_{h_x}}{k_x} \tag{3.16}$$

Average Nusselt number $(Nu)_{avg} = \frac{\sum_{x=1}^{n} Nu_x}{n}$ (3.17)

Here, $D_{h_x} and\ k_x$ are local hydraulic diameter and local thermal conductivity respectively.

d. Friction factor (f)

And fanning friction factors were evaluated using the following equation:

$$f = \frac{\Delta P D_h}{2\,\rho L u_{avg}^2} \tag{3.18}$$

Where, ΔP is pressure drop in the channel, D_h is channel hydraulic diameter, L is channel length, u_{avg} is average velocity and ρ is density of cooling fluid.

e. Pumping power (*P*)[39]

$$P = \Delta p_{ch} \times Q_{tot} \tag{3.19}$$

Where,Δp_{ch} is pressure drop and Q_{tot} is total volumetric flow rate.

f. Overall thermal resistance (R_{th})

Overall thermal resistance was calculated using the following equations [39]:

$$R_{th} = \frac{(T_{max} - T_{min})}{q'' A_b} = \frac{(T_{max} - T_{in})}{q'' A_b} \tag{3.20}$$

Where,T_{max} and T_{min} ($T_{min} = T_{in}$ because lowest wall temperature are observed at inlet of the channel) are the highest and lowest bottom wall temperatures of heat sink.

g. Performance factor (PF)

To measure the overall performance, the performance factor is defined as [84]:

$$PF = \frac{(Nu_{ef}/Nu_{sf})}{(f_{ef}/f_{sf})} = \frac{E_{Nu}}{E_f} \tag{3.21}$$

Where, E_{Nu} is effective Nusselt number and E_f is effective friction factor. Nu_{ef} and Nu_{sf} are average Nusselt numbers of EFMC and SFMC respectively. f_{ef} and f_{sf} are the corresponding fanning friction factors.

h. Other performance parameters

To evaluate the performance of conventional and modified MCHS designs, thermal resistance ratio, ξ_R, temperature difference ratio, $\sigma_{\Delta T}$ and pumping power ratio, ψ_{Pr} are defined as in[85]:

$$\xi_R = \frac{R_M}{R_C} \tag{3.22}$$

$$\sigma_{\Delta T} = \frac{\Delta T_M}{\Delta T_C} \tag{3.23}$$

$$\psi_{Pr} = \frac{P_M}{P_C} \tag{3.24}$$

Here, ΔT is temperature difference between bottom wall and average bulk fluid, the subscripts C and M indicate conventional and modified MCHS designs respectively.

3.8 Numerical validation

The numerical procedure followed in the present study was validated with experimental result of Lee et al. [84] where, similar geometrical details and boundary condition were used for numerical simulation [84], [86]. The percentage deviations of numerical results with experimental values were plotted as shown in Figure 3.2. The results revealed that the maximum and minimum deviation of pressure were 7.5 % and 1.3 %, which correspond to Re-329 and Re-377 respectively. Similarly, the maximum and minimum deviation of wall temperature noted as 2 % and 0.96 % correspond to Re-561 and Re-329 respectively. Therefore, numerical results obtained were found to be in good agreement with experimental results.

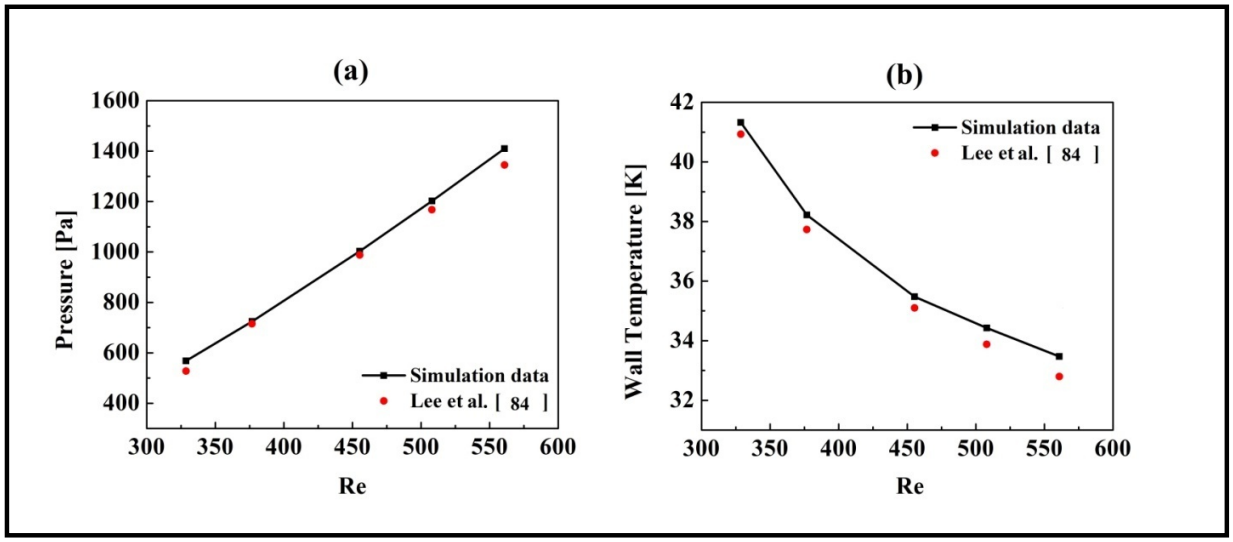

Figure 3.2 Variation of pressure and wall temperature with Reynolds number

CHAPTER 4

Optimization of double tapered microchannel heat sink geometry

This chapter describes thermal performance and fluid flow behaviour of three different geometrical microchannels in steady state laminar zone. For fair comparison, the same foot print area of straight, double taper and elliptical fin microchannels were modelled and numerically analyzed in the range of Re 100-768 and higher heat flux of 50-100 $\mathrm{W/cm^2}$. The different parameters such as average wall temperature, Nusselt number, friction factor, and performance factor variation with Reynolds number were measured for all the geometries and compared with straight fin microchannel. Finally, optimal channel geometry obtained was based on the performance factor for better heat transfer through the microchannel.

4.1 Computational modelling of microchannel heat sink

A microchannel heat sink with a footprint area of $L \times W = 25 \times 25\ mm^2$ was subjected to heat flux [87] of $q''_w = 50 - 100$ W/cm^2.as shown in figure 4.1(e). On this footprint area, forty taper channels ($N = 40$) were fabricated on copper block. The width and height were W_{in} and H_{in} at the inlet, W_{out} and H_{out} for the outlet of channel respectively. H (5.2 mm) represents the overall height of the heat sink. The width tapered ratio is W_x, $W_x = \left(\frac{W_{out}}{W_{in}}\right)$ and height tapered ratio is H_y, $H_y = \left(\frac{H_{out}}{H_{in}}\right)$. In this study, channel width and height vary linearly from inlet to outlet of the channel. The variation of channel width and height tapered ratio is from *0* to *1* and *1* to *3.9* respectively. This means taper is provided on both bottom wall as well as sidewalls of the channel as shown in Figure 4.1(a-c). All the geometrical dimensions of channel are specified in Table 4.1. Water was used as a cooling medium, whose thermal conductivity and viscosity were a function of temperature, as shown Table 3.2. The heat sink and coolant properties [83] are given in Table 3.3.

In this study, 1-D thermal resistance was used to simplify the analysis. From Figure 4.1(d) heat flux was applied at the base of heat sink, where the heat is transported in solid through conduction. And then it is transported from solid to fluid through convection. Therefore, the thermal resistance equation [39] is written as follows:

$$R_T = R_{cond} + R_{conv} = \frac{t}{A_c k_c} + \frac{1}{h_f A_s} \tag{4.1}$$

Where, R_T is total thermal resistance, R_{Cond} is conductive resistance, R_{Conv} is convective resistance, t is base thickness of microchannel, A_c is conductive area of solid and A_s is convective surface area of channel, k_c is thermal conductivity of heat sink (copper) and h_f is convective heat transfer coefficient of fluid.

Table 4.1 Dimensions of DTMC investigated numerically.

S.No	$\boldsymbol{W_i}$ $(\boldsymbol{mm})$	$\boldsymbol{W_o}$ $(\boldsymbol{mm})$	$\boldsymbol{W_x}$	$\boldsymbol{H_i}$ $(\boldsymbol{mm})$	$\boldsymbol{H_o}$ $(\boldsymbol{mm})$	$\boldsymbol{H_y}$
Case 1	*0.3*	*0.3*	*1*	*1.2*	*2.1*	*1.7*
					2.9	*2.4*
					3.8	*3.2*
					4.7	*3.9*
Case 2	*0.46*	*0.14*	*0.3*	*1.2*	*1.2*	*1*
	0.4	*0.2*	*0.5*			
	0.35	*0.24*	*0.7*			
	0.3	*0.3*	*1*			
Case 3	*0.46*	*0.14*	*0.3*	*1.2*	*2.1*	*1.7*
					2.9	*2.4*

					3.8	*3.2*
					4.7	*3.9*
	0.4	*0.2*	*0.5*	*1.2*	*2.1*	*1.7*
					2.9	*2.4*
					3.8	*3.2*
					4.7	*3.9*
	0.35	*0.24*	*0.7*	*1.2*	*2.1*	*1.7*
					2.9	*2.4*
					3.8	*3.2*
					4.7	*3.9*

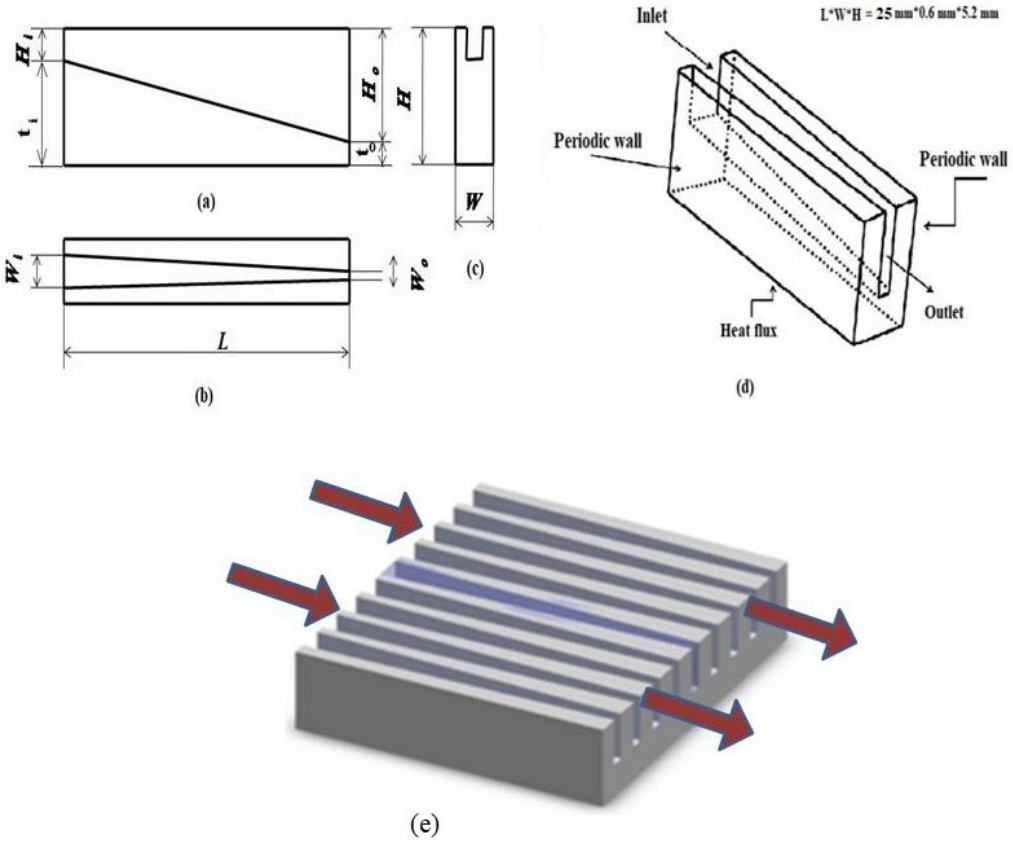

Figure 4.1 Schematic of double taper MCHS.(The figure is not drawn to scale) (a) front view (b) top view (c) side view (d) computational domain (e) heat sink

To perform computational analysis and reduce computational time, one complete channel width and half of the fin width on both sides of the channel was considered as shown in Figure 4.1(d). In this study, the geometrical model was prepared in SolidWorks; meshing and analysis were done in ANSYS FLUENT. The water enters the channels at a temperature of 308 K with a volume flow rate of 330-800 mL/min that corresponds to a Reynolds number 253 to 614. Besides this, the heat flux was applied at bottom wall of the channel was 100 W/cm^2. Periodic boundary conditions were applied on left and right side of the channel as shown in Figure 4.1(d). For all the cases, thermal performance parameters were compared on a constant volumetric flow basis.

4.2 Effect of height ratio on average bottom wall temperature, temperature difference ratio, thermal resistance ratio and pumping power

4.2.1 Average bottom wall temperature

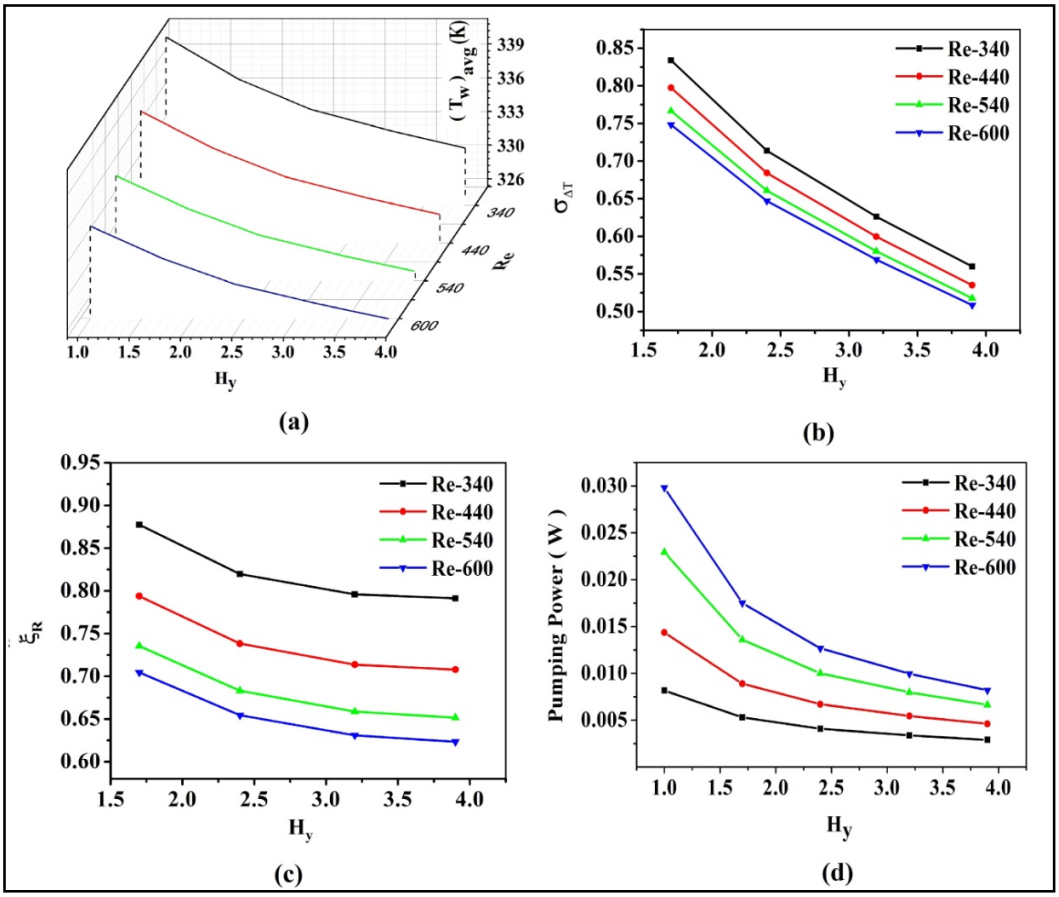

Figure 4.2 Effect of height tapered ratio and Re on (a) average bottom wall temperature, $(T_w)_{avg}$ (b) $\sigma_{\Delta T}$ (c) ξ_R and (d) pumping power, P

Figure 4.2(a) depicts the average bottom wall temperature as a function of height tapered ratio and Reynolds number (Re). At a constant Re-340, an increased height tapered ratio facilitates a larger convective surface area along the channel. With this, the given heat flux is distributed through the larger surface area minimizing the heat flux concentration per unit area. Thus, uniformity in temperature distribution is observed from temperature contours as shown in Figure 4.3(a) & (c) which is a result of quick transportation of heat

from solid wall to fluid core. For a constant Re-340, the average bottom wall temperature for various height taper ratios such as H_y-1.7, H_y-2.4, H_y-3.2, and H_y-3.9 was 337.65 K, 334.79 K, 332.70 K and 331.12 K respectively. The percentages of reduction of average bottom wall temperature corresponding to taper ratios are 5.77 %, 9.94 %, 12.98 %, and 15.29 % respectively. Hence the maximum reduction of average bottom wall temperature was observed at a height tapered ratio of H_y-3.9, Re-340, which is 15.29 % lower than straight microchannel (where an average bottom wall temperature of straight microchannel is 341.61 K). For the same height tapered ratio of H_y-3.9, an increasing Re from 340 to 600 leads to further reduction of average bottom wall temperature (9.41 %) by revamping additional heat carrying ability of the fluid. The average bottom wall temperatures for various Reynolds numbers 340, 440, 540 and 600 are 331.12 K, 328.41 K, 326.58 K and 325.65 K respectively as shown in Figure 4.2(a).

4.2.2 Temperature difference ratio

As illustrated in Figure 4.2(b), the variation of temperature difference ratio ($\sigma_{\Delta T}$) with height tapered ratio and Re. The temperature difference ratio ($\sigma_{\Delta T}$) is defined as the ratio of the temperature difference between the wall and fluid of a modified channel to that of a conventional microchannel. It is revealed that the height tapering brings down the temperature difference ratio rapidly. This is mainly due to reduction of thermal resistance. To explain the above phenomenon, flow field analysis was used. Figures 4.3(a) and (c) depict the average bottom wall temperature contours for various height taper ratios (H_y). As H_y increases, the average bottom wall temperature decreases significantly while the average fluid temperature rises slightly, resulting in reduction of the temperature gradient between the fluid and the wall. Therefore, lower temperature difference ratio is obtained for higher height taper ratio channel. The reduction of $\sigma_{\Delta T}$ for various height tapered ratios such as H_y-1.7, H_y-2.4, H_y-3.2 and H_y-3.9 was 0.83, 0.71, 0.62 and 0.55 respectively at Re-340. This is shown in Figure 4.2(b). For constant height tapered ratio H_y-3.9, increasing Re from 340 to 600 decreases $\sigma_{\Delta T}$ further by 0.55-0.50. Hence, it is apparent that the effect of Reynolds number on temperature difference ratio is quite small for height tapered microchannel.

4.2.3 Thermal resistance ratio

The variation of thermal resistance ratio (ξ_R) with height tapered ratio and Re as shown in Figure 4.2(c). The thermal resistance ratio (ξ_R) is defined as the ratio of the thermal resistance of a modified channel to that of a conventional microchannel. The increased height tapered ratio decreases both convective and conductive resistance. As shown in equation (4.1), convective resistance depends on both convective heat transfer coefficient and convective surface area of the heat sink, whereas conductive resistance depends on both substrate thickness and conductive area of channel. This increased height taper ratio lowers the fluid flow velocity as shown in Figure 4.3(b) & (d), which in turn lowers the convective heat coefficient. Although the convective heat transfer coefficient decreases, convective resistance decreases due to increased convective area. As a result, convective resistance decreases as height taper ratio increases. Furthermore, the decrease in average substrate thickness with height taper ratio reduces conductive resistance. Therefore, the reduction in overall thermal resistance significantly brings down the maximum bottom wall temperature of the channel as shown in Figures 4.3(a) and (c). The reduction inξ_R for various height tapered ratios H_y-1.7, H_y-2.4, H_y-3.2 and H_y-3.9 are 0.88, 0.82, 0.80 and 0.79 respectively at Re-340 as shown in Figure 4.2(c). For height tapered ratio H_y-3.9, the raise of Re from 340 to 600 decreases ξ_R further by 0.79-0.62.

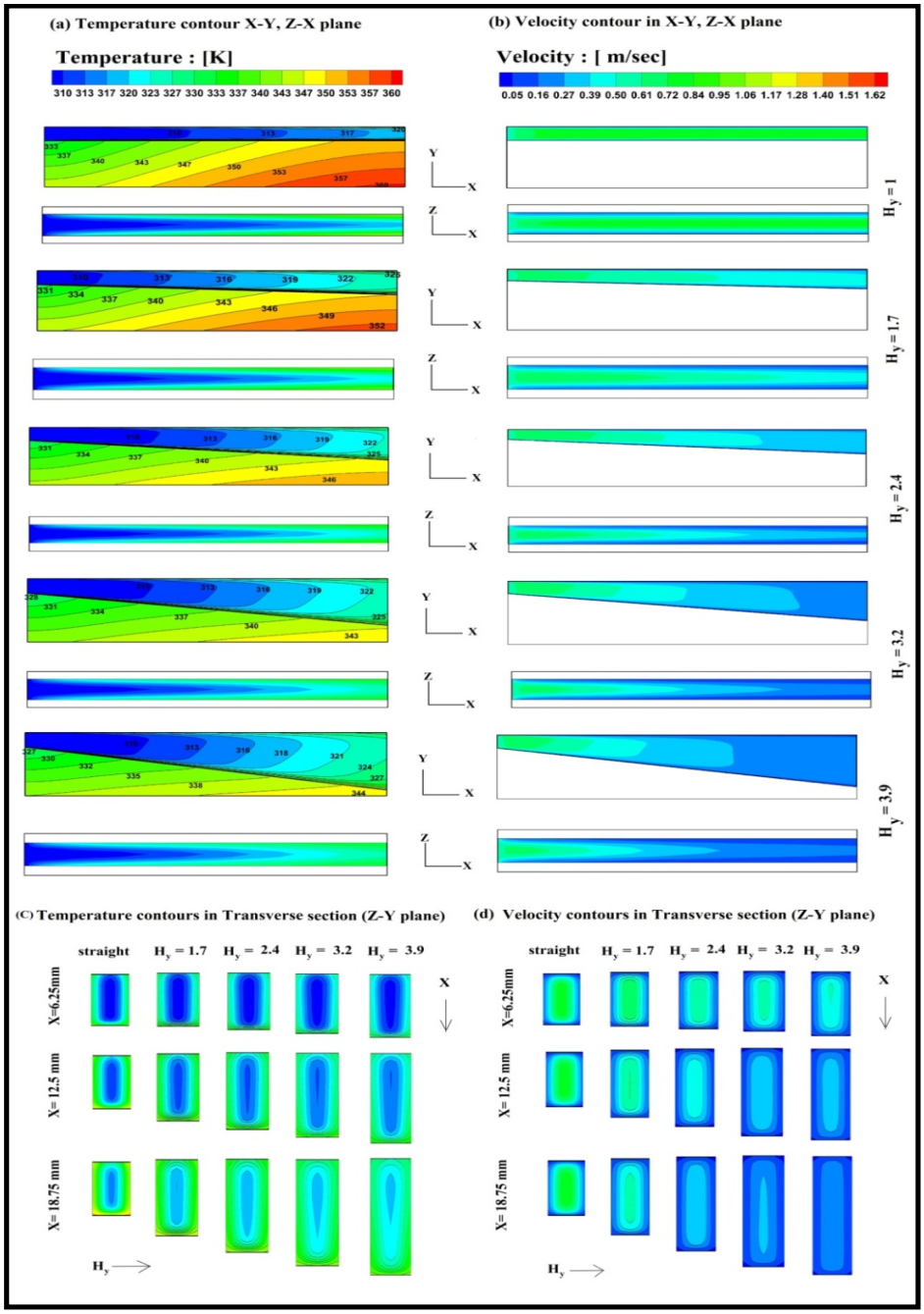

Figure 4.3 Temperature and velocity contours of height tapered MCHS at Reynolds number 340 (a) temperature contours in X-Y, Z-X plane (b) velocity contours in X-Y, Z-X plane (c) temperature contours in transverse (Z-Y plane) section (d) velocity contours in transverse (Z-Y plane) section

4.2.4 Pumping power

Figure 4.2(d) illustrates the effect of height tapered ratio on pumping power for various Reynolds number (340-600). It is observed from Figure 4.3(b) & (d), an increasing height tapered ratio decreases the velocity of the fluid. Due to lower velocity of fluid, inertia force is reduced, requiring less pressure force to cross the channel and resulting in lower pressure drop. This reduced pressure drop minimizes the pumping power required to pump the fluid in the channel. Therefore, pumping power ratio decreases with an increase in height tapered ratio. As shown in equation (Eq.3.24), pumping power ratio is defined as the ratio of the power required to pump fluid through a height tapered microchannel to the power required to pump fluid through a conventional straight microchannel. At Re-340, the pumping power ratios for various height tapered ratio channels such as H_y-1.7, H_y-2.4, H_y-3.2, and H_y-3.9 are 0.65, 0.50, 0.41, and 0.36 respectively. In this, a lower pumping power ratio implies higher pumping power reduction and vice versa. Hence, the maximum pumping power reduction is attained at a height tapered ratio of H_y-3.9 for Re-340.

Also, for a constant height taper ratio of H_y-3.9, increase in Reynolds number from 340-600 increases the pumping power ratio from 0.36 to 1. This is mainly due to an increase in fluid velocity with increasing Reynolds number. At Re-600, pumping power required to pump the fluid in the channel increases and becomes equal to power required in conventional straight microchannel. Therefore, Re higher than 600 is not advantageous.

4.3 Effect of width ratio on bottom wall temperature, temperature difference ratio, thermal resistance ratio and pumping power

4.3.1 Average bottom wall temperature

Figure 4.4(a) illustrates the variation of channel average bottom wall temperature with width tapering and Reynolds number (Re). It is observed from Figure 4.4(a) that the channel average bottom wall temperature first increases and then decreases with an increasing width tapering as shown in 4.5(a). This is mainly due to the predominant effect of conductive and convective resistance of heat sink. The average bottom wall temperature for various width taper ratios such as W_x-0.7, W_x-0.5, and W_x-0.3 are 338.76 K, 339.15 K and 338.04 K respectively. The reduction of average bottom wall temperature corresponding to width

taper ratios are 4.16 %, 3.04 %, and 5.21 % respectively, when compared to straight microchannel for a constant Re-340.

Similarly, for constant width tapering (W_x-0.3), an increasing Re decreases the average bottom wall temperature. The average bottom wall temperature for various Reynolds numbers 340, 440, 540 and 600 are 338 K, 334.8 K, 332.5 K and 331.2 K respectively. There is a 10.46 % reduction in average bottom wall temperature when Re is increased from 340 to 600. It is clear from the results that the reduction of average bottom wall temperature is more effective with rise of Re.

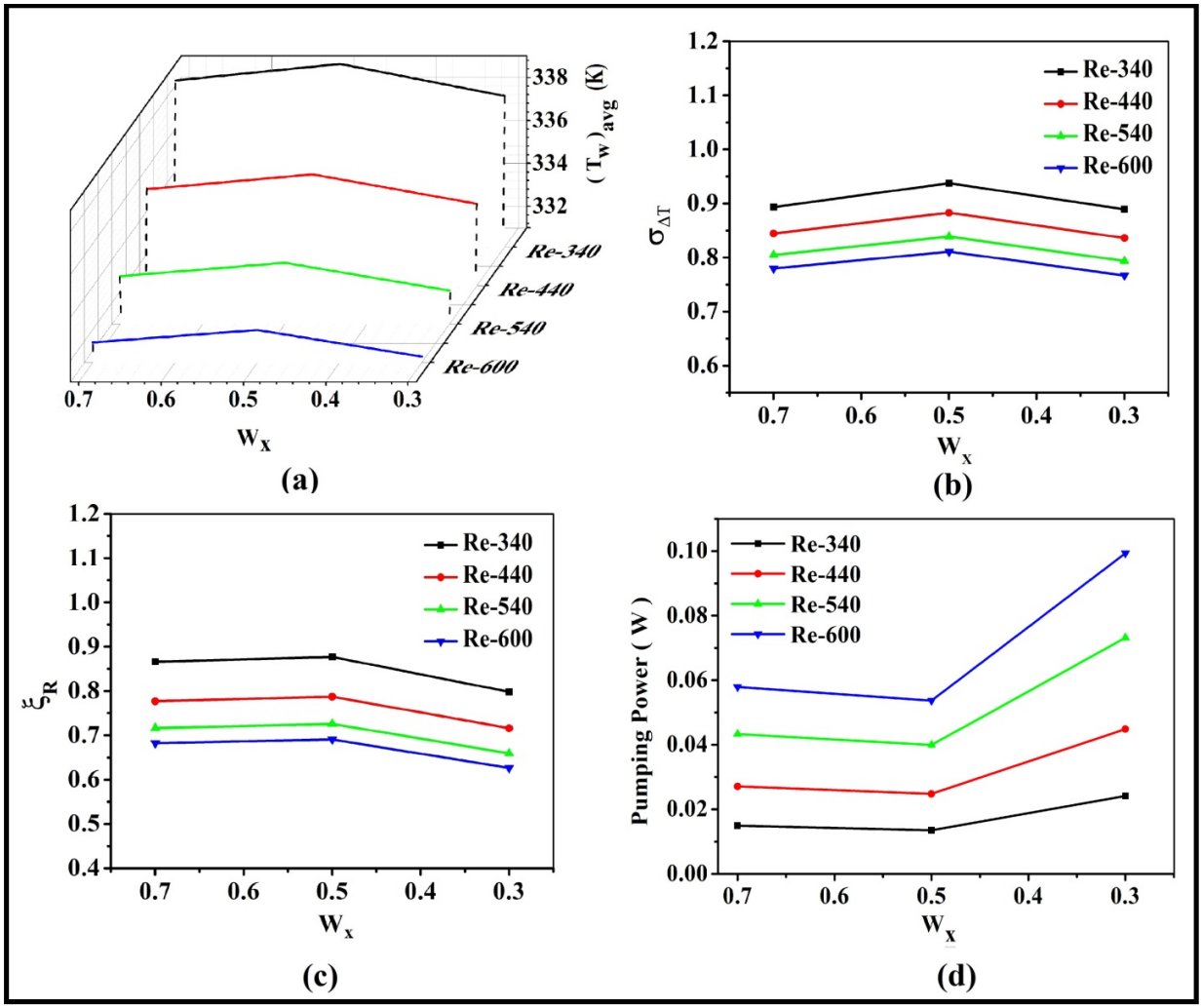

Figure 4.4 Effect of width tapered ratio and Re on (a) average bottom wall temperature, $(T_w)_{avg}$ (b) $\sigma_{\Delta T}$ (c) ξ_R and (d) pumping power, P

To explain the above phenomenon, flow field analysis was used. Figure 4.5 shows the temperature and velocity contours of heat sink and fluid in the mid-plane X-Y and Z-X. Besides, the temperature and velocity contours of fluid in transverse section (Z-Y plane) for a Reynolds number of 340 are shown. It is clear from Figures 4.5(b) and (d) that fluid is accelerated by increasing width tapering. This leads to reduction in boundary layer thickness and enhances the convective heat transfer coefficient. Moreover, as shown in equation (4.1) an increase in fin width along the length of channel further decreases convective resistance. Hence a uniform wall temperature is observed in the channel base along Y-direction by width tapering. This is helpful to maintain uniform temperature over the heat generating devices and enhance their performance.

4.3.2 Temperature difference ratio

Figure 4.4(b) shows the effect of width tapering on temperature difference ratio ($\boldsymbol{\sigma_{\Delta T}}$). It is evident from Figure 4.4(b) that temperature difference ratio is not monotonic, it first increases and then decreases with width tapering. The reason for this is discussed in above section. The reduction $\sigma_{\Delta T}$ for various width tapered ratios W_x-0.7, W_x-0.5, and W_x-0.3 are 0.89, 0.93, and 0.88 respectively at Re-340 as shown in Figure 4.4(b). For width tapered ratio of W_x-0.3, the increase in Re from 340 to 600 decreases $\sigma_{\Delta T}$ further by 0.88-0.76. It is evident that the effect of Reynolds number on temperature difference ratio is quite effective on width tapered microchannel.

4.3.3 Thermal resistance ratio

Figure 4.4(c) shows variation of thermal resistance ratio (ξ_R) with width tapering. It is revealed from Figure 4.4(c) that decreased W_x increases thermal resistance ratio first and then it decreases thermal resistance ratio. From equation (4.1), decreasing width taper ratio W_x, reduces conductive thermal resistance of tapered channel due to increase of conductive fin area A_c. Decreasing W_x decreases convective surface area A_s, while at the same instant width tapering decreases cross-sectional area of channel along the stream direction. The reduced cross-sectional area surges the fluid velocity in order to maintain the same flow rate through width tapered channel. As a result, the convective heat transfer coefficient is enhanced. Therefore the convective resistance may increase or decrease depending on the

relative magnitudes of convective surface area and convective heat transfer coefficient. For $W_x < 0.5$, the rate of increase of convective heat transfer coefficient is more than decrease of convective surface area and results in decrease in thermal resistance ratio. For $W_x > 0.5$, thermal resistance ratio decreases; this is in fact the combined effect of convective surface area and convective heat transfer coefficient.

The reduction of ξ_R for various width tapered ratios W_x-0.7, W_x-0.5, and W_x-0.3 are 0.87, 0.88, and 0.80 respectively at Re-340 as shown in Figure 4.4(c). For width tapered ratio W_x-0.3, the increase of Re from 340 to 600 decreases ξ_R further by 0.80-0.63.

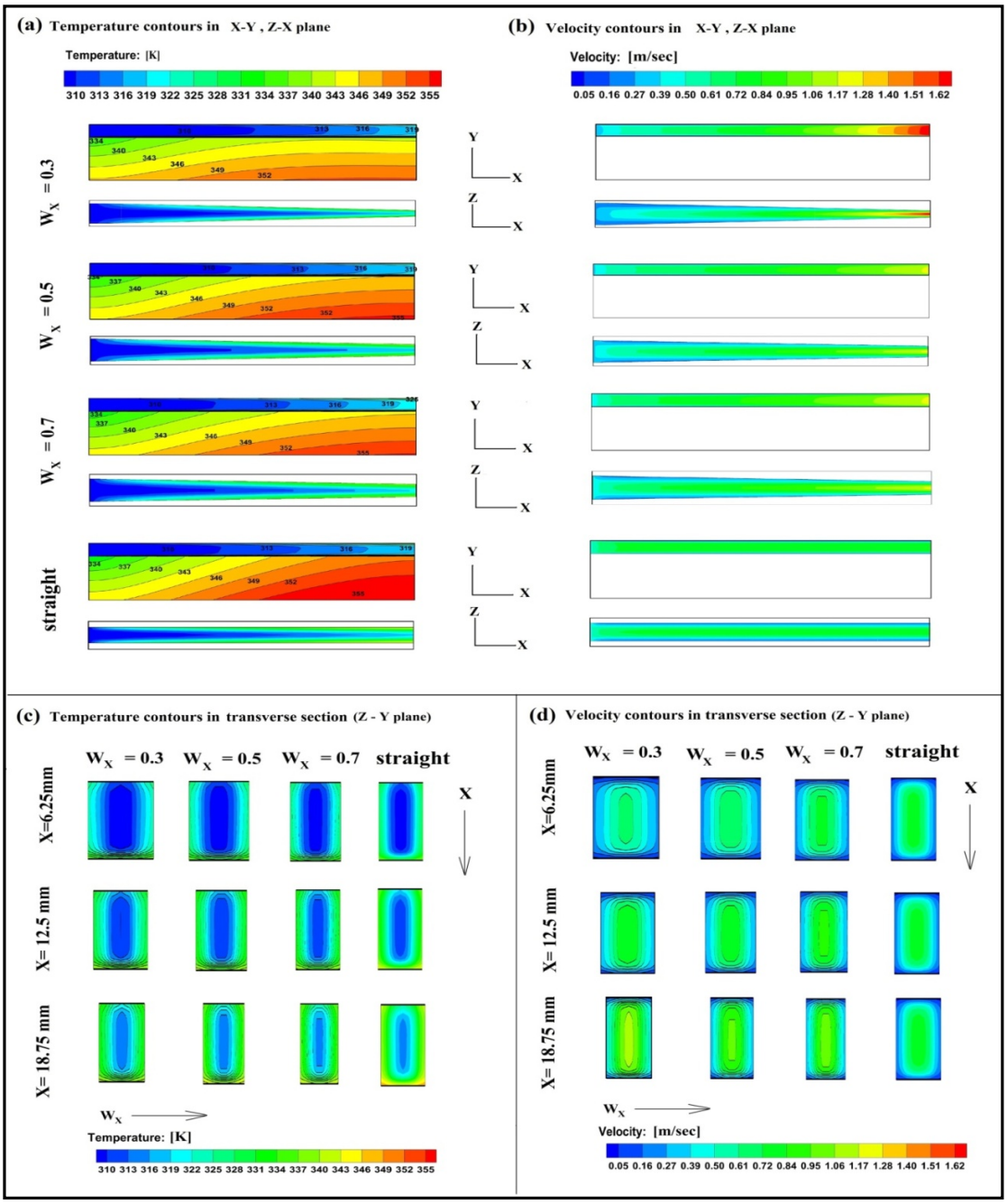

Figure 4.5 Temperature contours and velocity contours of width tapered MCHS (a) temperature contours in X-Y and Z-X plane (b) velocity contours in X-Y and Z-X plane (c) temperature contours in transverse section and (d) velocity contours in transverse section

4.3.4 Pumping power

Figure 4.4(d) demonstrates the effect of width tapered ratio on pumping power for various Reynolds numbers (340-600). It is observed from Figure 4.4(d) that a decreasing width tapered ratio increases the velocity of the fluid. Due to the higher velocity of fluid; the inertia force is increased, requiring more pressure force to cross the channel, resulting in a higher pressure drop. The increased pressure drop maximizes the pumping power required to pump the fluid in the channel. Therefore the pumping power ratio is increased with decreasing width taper ratio. As shown in equation (3.24), pumping power ratio is defined as the ratio of the power required to pump fluid through a width tapered microchannel to the power required to pump fluid through a conventional straight microchannel. At Re-340, the pumping power ratios for various width tapered ratio channels such as W_x-0.7, W_x-0.5, and W_x-0.3 were 1.82, 1.65, and 2.94 respectively. A pumping power ratio less than one indicates power reduction and pumping power ratio larger than one implies power consumption. For the same Reynolds number, among all the width tapered ratios, W_x-0.3 required maximum pumping power to pump fluid through the channel, which was 2.94 times that of the straight microchannel.

Additionally, for a constant width taper ratio of W_x-0.3, on increasing the Reynolds number from 340-600, further increases the pumping power ratio from 2.94 to 12.15. This is mainly due to an increased fluid velocity caused by increasing Reynolds number.

4.4 Effect of height and width ratio on bottom wall temperature, temperature difference ratio, thermal resistance ratio and pumping power

4.4.1 Average bottom wall temperature

A taper that is applied to both the bottom and side walls at the same time is referred to as double tapered microchannel. The influence of the height and width tapering on the average bottom wall temperature of the channel is depicted in Figure 4.6(a). It is observed from Figure 4.6(a) that a simultaneous width and height tapering decreases the average bottom wall temperature. Because of the reduced cross-sectional flow area and base thickness of the channel, the velocity of the fluid increases and the maximum bottom wall

temperature decreases dramatically. As a result, there is a rapid transfer of heat from channel wall to fluid core as shown in Figure 4.7(a-d).

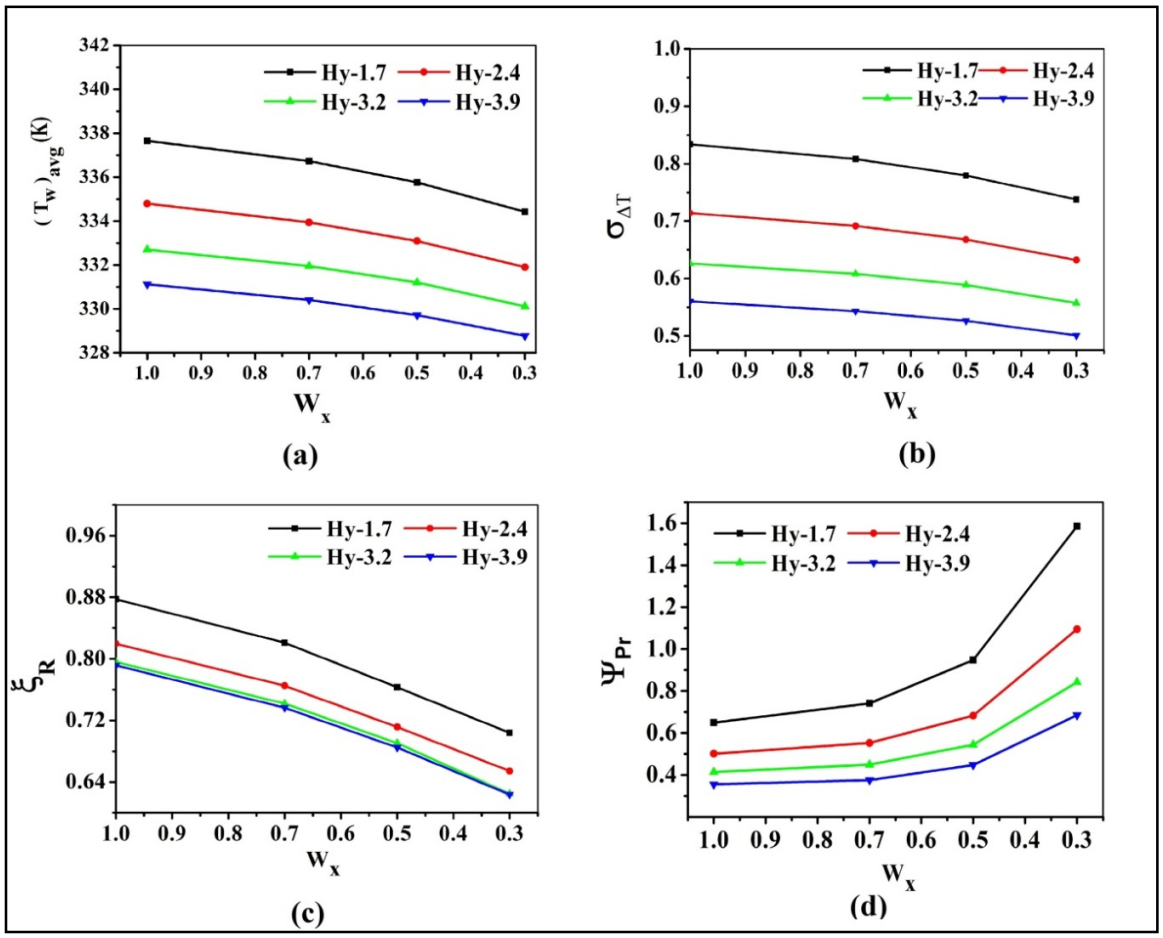

Figure 4.6. Effect of width and height tapered ratio at Re 340 on (a) average bottom wall temperature,$(T_w)_{avg}$ (b) $\sigma_{\Delta T}$ (c) ξ_R (d) pumping power, P

The average bottom wall temperature was reduced by different amounts for various DTMCs, such as Wx-1 & Hy-3.9, Wx-0.7 & Hy-3.9, Wx-0.5 & Hy-3.9, and Wx-0.3 & Hy-3.9 at Re-340, with reductions of 331.12 K, 330.40 K, 329.71 K, and 328.77 K respectively. The percentage reduction in average bottom wall temperature for these DTMCs compared to a straight microchannel was 15.29%, 16.33%, 17.34%, and 18.72% respectively. Therefore, the DTMC of Wx-0.3 & Hy-3.9 at Re-340 exhibited the lowest average bottom wall temperature of 328.77 K among all the DTMCs considered.

4.4.2 Temperature difference ratio

Figure 4.6(b) revealed the combined effects of both H_y and W_x on variation of temperature difference ratio ($\sigma_{\Delta T}$). It can be seen that $\sigma_{\Delta T}$ decreases with simultaneous height and width tapering. The reason for this has already been discussed in the previous section. At Re-340, the maximum reduction $\sigma_{\Delta T}$ for various DTMC such as W_x-1 & H_y-3.9, W_x-0.7 & H_y-3.9, W_x-0.5 & H_y-3.9, and W_x-0.3 & H_y-3.9was0.56, 0.54, 0.52, and 0.50 respectively, shown in Figure 4.6(b). As a result, at Re-340, the lowest $\sigma_{\Delta T}$ of 0.5 is reported for DTMC W_x-0.3 & H_y-3.9 followed by the next lowest $\sigma_{\Delta T}$ of 0.52 for DTMC W_x-0.5 & H_y-3.9.

4.4.3 Thermal resistance ratio

Figure 4.6(c) depicts the variation of thermal resistance ratio (ξ_R) with both height and width tapered ratio. The height tapering decreases bottom wall thickness and reduces conductive thermal resistance. Width tapering increases velocity of the fluid and minimizes thermal and hydrodynamic boundary layer thickness. It results in a reduction of convective fluid and conductive solid thermal resistances. Therefore, the thermal resistance ratio is decreased by the combined effect of width and height tapering. The maximum reduction of thermal resistance ratio for various DTMC such as W_x-1 & H_y-3.9, W_x-0.7 & H_y-3.9, W_x-0.5 & H_y-3.9, and W_x-0.3 & H_y-3.9 was 0.79, 0.74, 0.68, and 0.62 respectively, at Re-340 as shown in Figure 4.6(c). Therefore, the maximum reduction in thermal resistance was spotted at0.62 for DTMC W_x-0.3 & H_y-3.9 at Re-340, followed by next maximum reduction in thermal resistance of 0.68 for W_x-0.5 & H_y-3.9 at the same Reynolds number.

4.4.4 Pumping power

Figure 4.6(d) shows a variation of pumping power ratio with both width and height tapering. Figure 4.6(d) clearly shows that the pumping power ratio increases with simultaneous height and width tapering. This is due to an increase in fluid velocity in the channel as depicted in Figures 4.7(b) and (d). As the velocity of the fluid rises, the inertia force increases, requiring more pressure force to cross the channel, resulting in a greater pressure drop. An increased pressure drop surges the pumping power required to pump the fluid through the channel. Therefore, the pumping power ratio increases with simultaneous

height and width tapering. In this, a lower pumping power ratio implies higher pumping power reduction and vice versa. The pumping power ratio for various DTMC such as W_x-1 & H_y-3.9, W_x-0.7 & H_y-3.9, W_x-0.5 & H_y-3.9, and W_x-0.3 & H_y-3.9 are 0.35, 0.37, 0.44 and 0.68 respectively at Re-340. It can be concluded from the above results that the minimum and maximum power reduction were observed at DTMC W_x-0.3 and H_y-3.9 and DTMC W_x-1 and H_y-3.9 respectively for the same Reynolds number when compared to the straight microchannel.

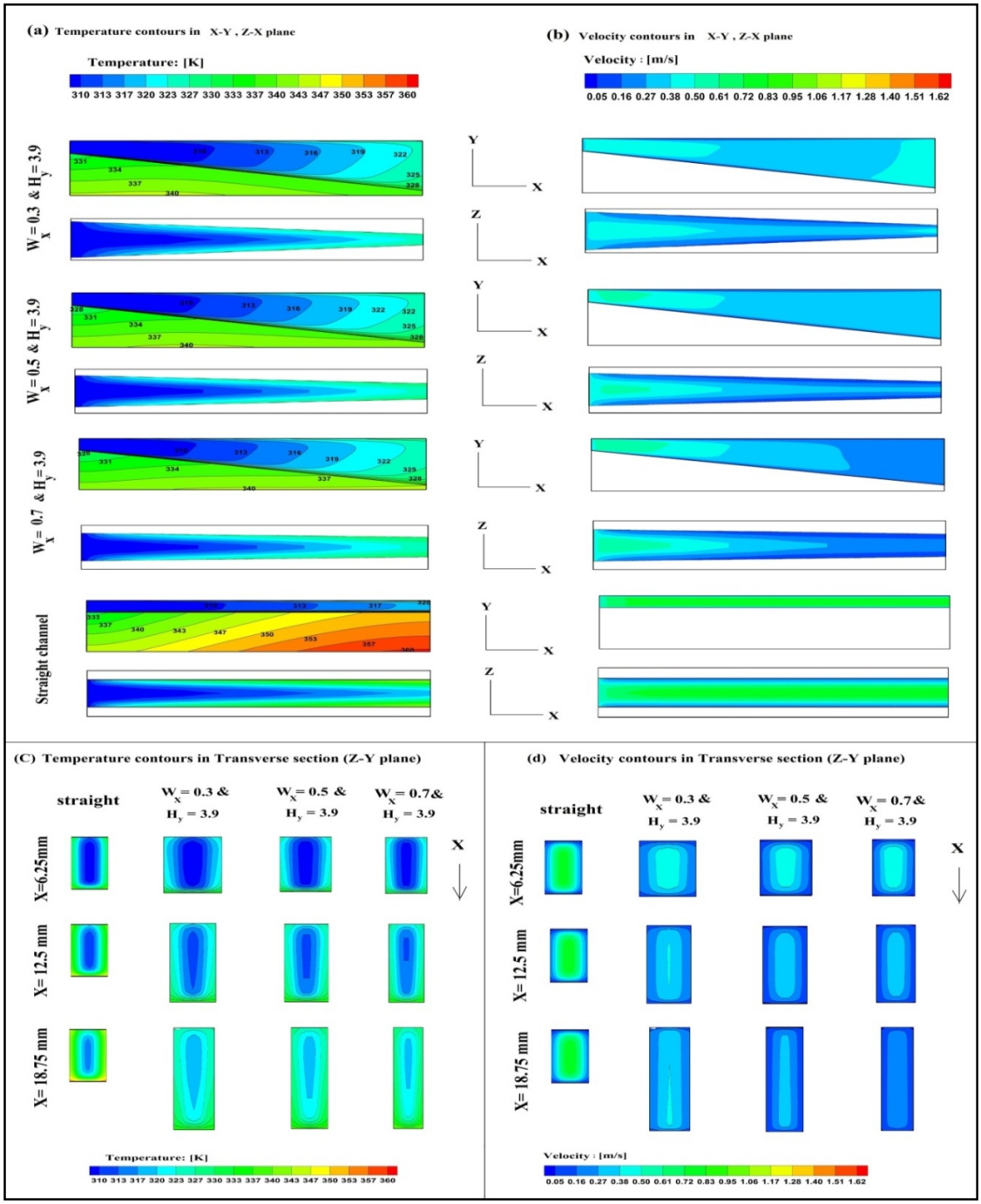

Figure 4.7 Width tapered MCHS at constant H_y-3.9 (a) temperature contours in X-Y and Z-X plane (b) velocity contours in X-Y and Z-X plane (c) temperature contours in transverse section and (d) velocity contours in transverse section

The best microchannel dimensions are determined based on performance parameters like thermal resistance ratio, temperature difference ratio, pumping power ratio and uniformity of temperature in the channel wall. It is clear from Figures 4.8(a-d) and Table 4.2 that temperature difference ratio and thermal resistance ratio are lowest for DTMC Wx-0.3 & H_y-3.9 at Re-340, but it requires more power to pump the fluid through the channel than other DTMCs. Among all, the DTMCsW_x-0.5 & H_y-3.9 at Re-340 has a 35.2 % lower pumping power than DTMC W_x-0.3 & H_y-3.9 with little compromise in thermal resistance ratio of 9.6 % and temperature difference ratio of 4 %. Therefore, DTMC W_x-0.5 & H_y-3.9 combination yields the best results. Furthermore, a uniform wall temperature is observed along the Y-axis in the channel wall depicted in Figure 4.8(a). This uniform temperature is one of the major advantages, which can improve the functionality and reliability of high heat flux generating devices.

Table 4.2 Performance parameters for various width tapered ratios, at height tapered ratio of 3.9 and Re 340.

W_x	**Pumping Power ratio**	**Pumping Power reduction (%)**	**Temperature difference ratio**	**Temperature difference rise (%)**	**Thermal Resistance ratio**	**Thermal Resistance rise (%)**
0.3	0.68	-	0.50	-	0.62	-
0.5	0.44	35.2	0.52	4	0.68	9.6
0.7	0.37	45.5	0.54	8	0.73	17.7
1	0.35	48.5	0.55	10	0.79	27.4

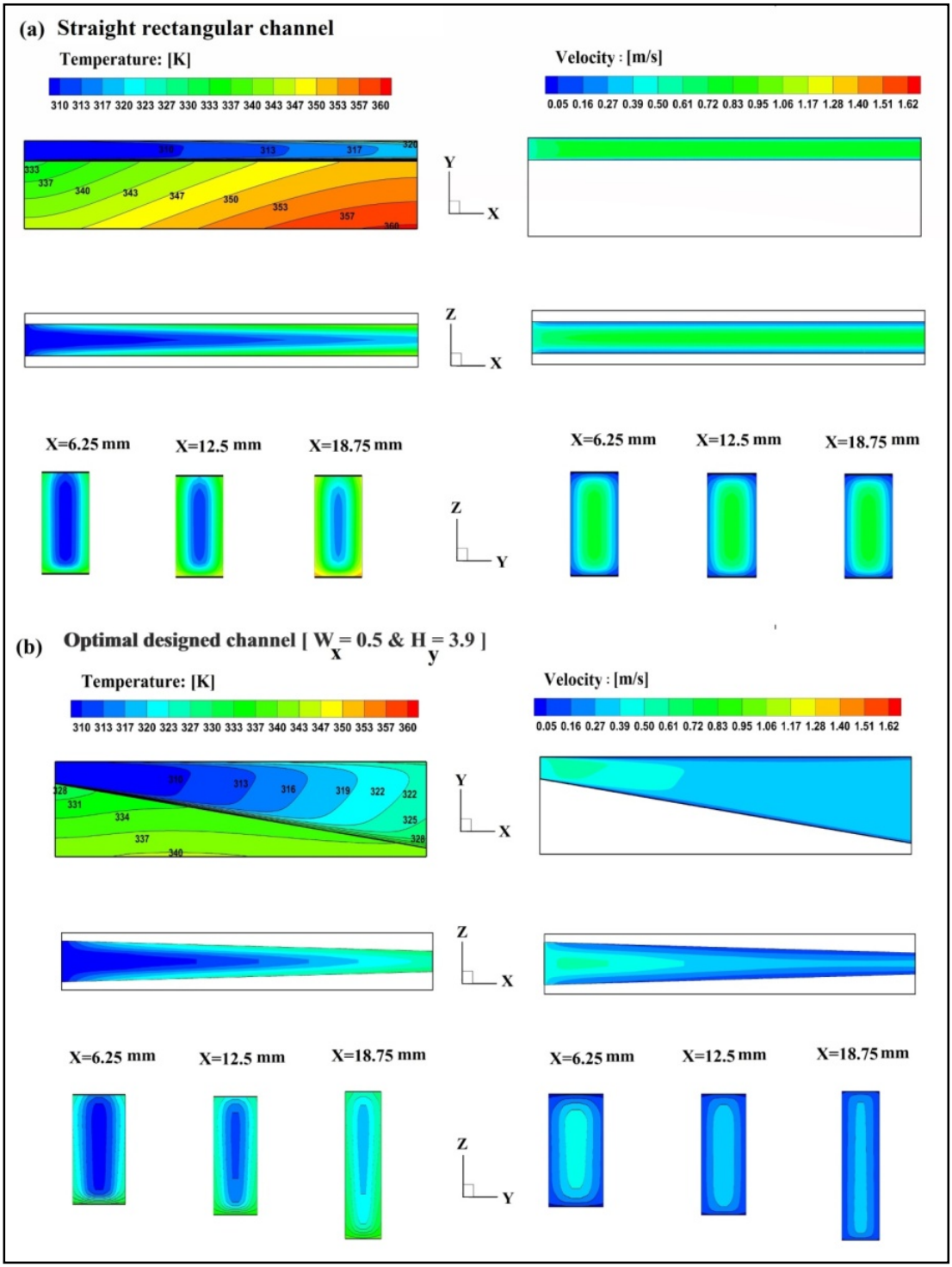

Figure 4.8 Temperature and velocity contours of (a) straight and (b) best design channel (DTMC)

4.5 Conclusions

Thermal performance and fluid flow characteristics of double taper microchannel were studied numerically. The individual and combined effects of height and width tapering over a range of flow rates Re 340 to Re 600 were investigated. In this analysis, the wall temperature, thermal resistance ratio, temperature difference ratio and pumping power ratio of channel were evaluated and the following important findings are drawn from the current study.

- The height tapering brings the bottom wall temperature lower than that of straight microchannel by lowering thermal resistance. The maximum reduction of average bottom wall temperature was15.29 % for a height ratio of H_y-3.9 and Re-340. Other parameters like temperature difference ratio, thermal resistance ratio, and pumping power ratio were0.55, 0.79, and 0.36 respectively.

- For the same height taper ratio of H_y-3.9, increasing the Reynolds number from 340 to 600 leads to lowering of temperature difference ratio (0.55-0.50) and thermal resistance ratio (0.79-0.62) are lowered. However, the same amount of power is required to pump the fluid through the channel as in a straight channel.

- The reduced width ratio initially raises thermal resistance ratio and then lowers it. The maximum reduction in average bottom wall temperature was 5.21 % at width ratio W_x-0.3 and Re-340. Other parameters like, temperature difference ratio, thermal resistance ratio and pumping power ratio were 0.88, 0.8 and 2.94 respectively. However, to pump the fluid through W_x-0.3 channel, 2.94 times more pumping power was required than in a straight channel.

- For the same width tapered ratio of W_x-0.3, increasing the Reynolds number from 340 to 600 resulted in a significant reduction of temperature difference ratio (0.88-0.76) and thermal resistance ratio (0.80-0.63). However, to pump the fluid through the channel, 12.15 times more pumping power was required than for a straight channel.

- The combined effect of width and height tapering reduces the thermal resistance below individual width and height tapering channels. Because of the reduced cross-sectional

flow area and base thickness of the channel, the velocity of the fluid increases and the maximum bottom wall temperature decreases dramatically. As a result, thermal resistance is reduced.

- The double taper microchannel (DTMC) W_x-0.3 & H_y-3.9 at Re-340 has an average bottom wall temperature reduction of 18.72 %, temperature difference ratio of 0.5, thermal resistance ratio of 0.62 and pumping power ratio of 0.68. Although the temperature reduction and thermal resistance ratio are better, it requires 35.2 % more pumping power than the optimal DTMC W_x-0.5 & H_y-3.9 channel.

- The optimal DTMC W_x-0.5 & H_y-3.9 at Re-340 has an average bottom wall temperature reduction of 17.34 %, a temperature difference ratio of 0.52, a thermal resistance ratio of 0.68 and a pumping power ratio of 0.44. A little compromise of temperature difference ratio of 4 % and thermal resistance ratio of 9.6 % for DTMC W_x-0.5 and H_y-3.9 combination yields the best results. Moreover, it has a uniform temperature at the base of heat sink.

CHAPTER 5

Numerical study of elliptical fin microchannel heat sink

The previous chapter described the thermal performance and the fluid flow behaviour of a double tapered microchannel in a steady state laminar zone. Simultaneous shrinkage of side walls and expansion of bottom wall along the downstream direction reduced pumping power, bottom wall temperature, and enhanced thermal performance. This is mainly caused by the converging and diverging effect of fluid as it passes through the double taper microchannel. The converging and diverging effect of double tapered microchannel enhanced fluid mixing in the channel and reduced boundary layer thickness. Therefore, better heat transfer was anticipated with this channel. Further, the converging and diverging flow concept motivated the establishment of novel geometry like the elliptical fin microchannel, which naturally induces flow patterns in the channel. Another important concept introduced was the effect of secondary flow on elliptical microchannels, which is deduced from oblique fin microchannels.

The present chapter describes the thermal performance and the fluid flow behaviour of an elliptical fin microchannel in steady state laminar zone. Initially, the fin is positioned in-line with fluid flow and then it is oriented from 0º to 12º with an interval of 2º about the centre of the elliptical fin. The fluid flow and heat transfer characteristics for these channels were then analysed and compared with straight fin microchannel in the range of Re 100-768 and higher heat flux of 50-65 W/cm^2. In addition, other parameters such as average wall temperature, Nusselt number, friction factor and performance factor variation with Reynolds number was investigated and discussed in detail.

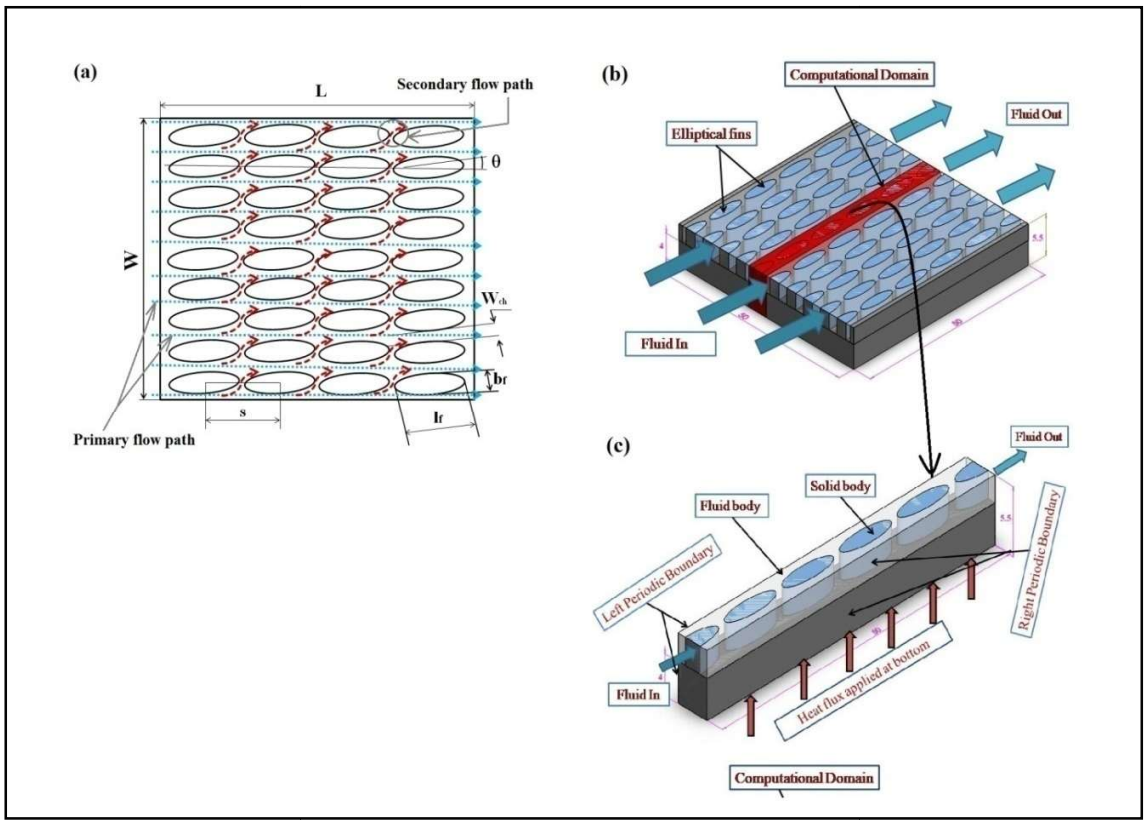

Figure 5.1 Schematic of elliptical MCHS (The Figure is not drawn to scale) (a) top view (b) 3D view(c) computational domain

5.1 Computational modelling

Figure 5.1 depicts a 3D view of elliptical fin microchannel (EFMC) heat sink with 50 mm × 50 mm × 5.5 mm size. Total of forty-nine elliptical fin rows with a lateral spacing of 620 µm and twenty fins with a longitudinal spacing of 2600 µm were modeled on the substrate. The elliptical fin has a height of 1500 µm, and semi-major axis and minor axis of 1260 µm and 190 µm respectively. This design was a substitute for the straight fin microchannel (SFMC) heat sink of same dimensions. Initially, the fin was positioned in line with fluid flow and then it was oriented from 0º to 12º about the centre of the elliptical fin with respect to fluid flow direction to analyze the hydrodynamic and heat transfer characteristic of fluid through the channel. The complete geometrical details of both microchannel heat sinks are shown Table 5.1. Water was used as cooling fluid, and its

thermal conductivity and viscosity were a function of temperature. Additionally, heat sink and coolant properties are provided in Table 3.2.

Table 5.1 Dimensions of SFMC and EFMC were investigated numerically.

Characteristic	**Straight channel**	**Elliptical channel**
Material	Copper	
Foot print, Width × length (mm)	50 × 50	
Main channel width, W_{ch} (µm)	620	
Channel depth, H (µm)	1500	
Fin width, W_f (µm)	380	
Aspect ratio, α	2.4	
Fin rows, N	49	
Fins per row	-	20
Fin centre distance, S (µm)		2600
Semi-major axis, l_f (µm)	-	1260
Semi-minor axis, b_f (µm)	-	190
Orientation angle, θ (deg)	-	0-12

5.2 Flow characteristics

5.2.1 Pressure drop

Figure 5.2 shows that the effect of elliptical fin orientation angle and Reynolds number (Re) on pressure drop for heat fluxes of 50 W/cm^2 and 65 W/cm^2. For constant Re,

increasing the orientation angle of the elliptical fin about the fluid flow direction (0º-12º) surges the pressure drop. This surge in pressure drop depends on flow obstruction area and fluid velocity. The higher elliptical fin angle has higher flow obstruction area and vice versa. This higher flow obstruction area offers more resistance to fluid flow and hence causes higher pressure drag across the fin. In addition, higher fluid velocity at the entry of larger angled fin retards the fluid velocity abruptly and causes greater momentum loss, which results in higher pressure drop in the channel.

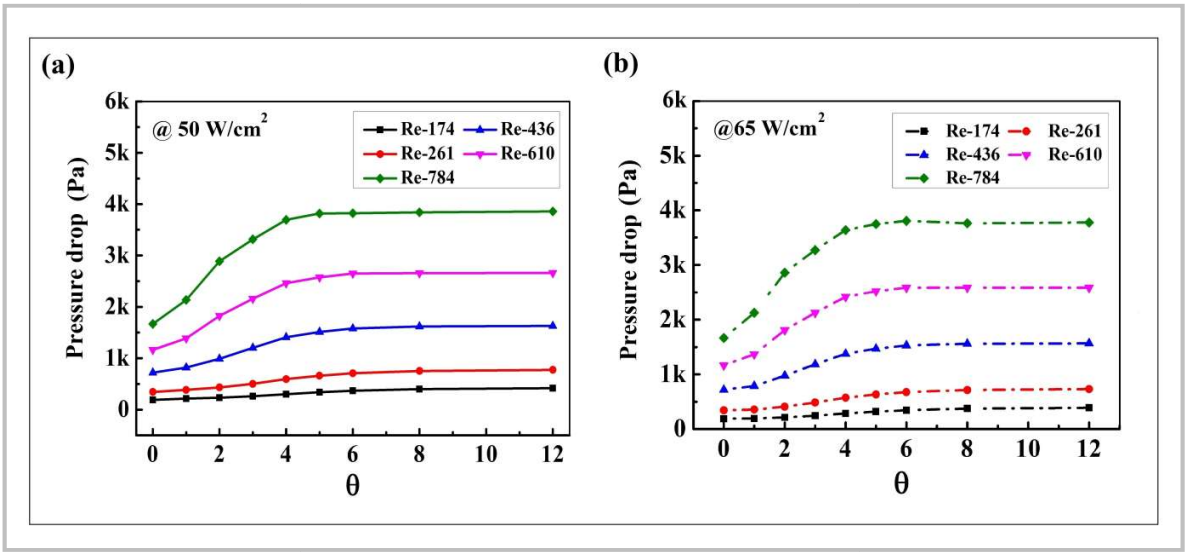

Figure 5.2 Pressure drop for various angles of elliptical fin arrangement with flow direction for heat flux of (a) 50 W/cm^2 (b) 65 W/cm^2

For both heat fluxes, at constant Re, the gradual rise in pressure drop is observed with an increasing elliptical fin angle (0°-12°), whereas pressure drop increases rapidly with an increase in Re (174-784), as shown in Figure 5.2. The maximum and minimum pressure drop of EFMC was 190 Pa and 3855 Pa corresponding to 0º and 12º respectively for a heat flux of 50 W/cm^2. The pressure drop which corresponds to highest performance factor is 15 % higher than that of SFMC. Moreover, the pressure drop percentage for various EFMCs over SFMC for flow ranges of Re-174 to 784 is given in Table 5.2. The negative sign implies a pressure drop that is lower than that of SFMC.

Table 5.2 Pressure drop % for various EFMC's over SFMC.

Type of channel	Pressure drop									
	Heat flux 50 W/cm^2					Heat flux 65 W/cm^2				
	Re-174	**Re-261**	**Re-436**	**Re-610**	**Re-784**	**Re-174**	**Re-261**	**Re-436**	**Re-610**	**Re-784**
0^o EFMC	-25.31	-21.74	-16.66	-14.21	-11.02	-16.05	-13.68	-9.87	-7.38	-5.74
2^o EFMC	-8.44	-1.64	15.00	38.32	54.07	-5.20	3.20	22.48	43.87	61.71
4^o EFMC	18.59	35.45	63.32	88.73	97.08	27.00	44.52	72.58	91.97	105.54
6^o EFMC	44.84	61.08	82.81	103.65	107.11	53.50	69.81	91.63	105.54	115.24
8^o EFMC	58.09	71.27	87.38	104.22	104.90	66.09	79.39	95.65	105.60	112.61
12^o EFMC	64.44	76.18	88.85	104.48	105.71	72.71	83.59	96.49	106.44	113.57

5.2.2 Local pressure

Figure 5.3A shows pressure drop variation along the channel length for straight and 2º EFMC at a heat flux of 50 W/cm^2 and 65 W/cm^2. The elliptical fin oriented 2º to fluid stream reported a steep decrease in pressure drop along the channel length when compared to straight fin. Besides, the pressure curve is associated with a local dip followed by a local rise due to periodically changing flow area from inlet to outlet of the channel, as shown in Figure 5.3A.

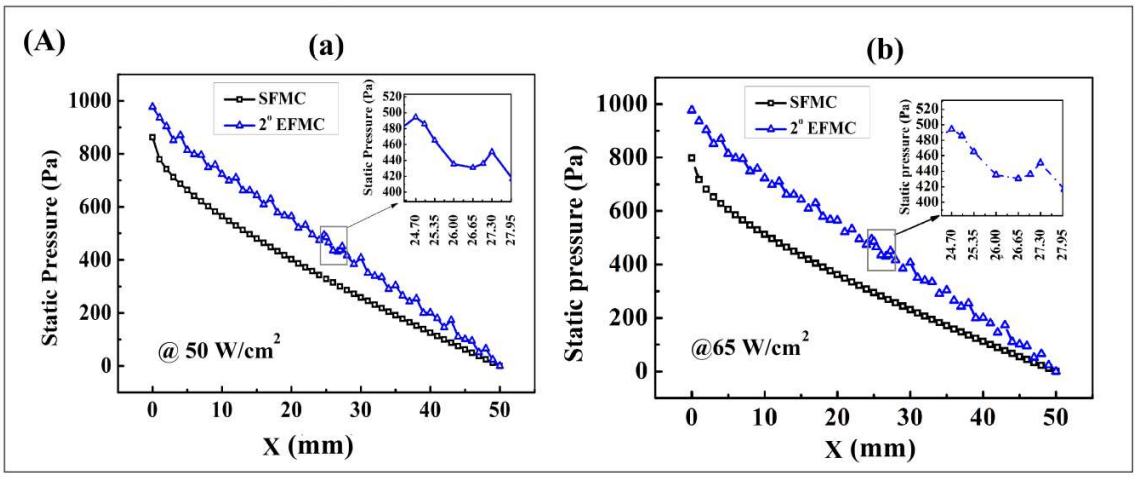

Figure 5.3 (A) The effect of local static pressure along with downstream of flow at Re 436 for (a) 50 W/cm^2 and (b) 65 W/cm^2 (B) pressure contours at various locations (in Y-Z plane).

To predict the flow characteristics across single elliptical fin, a total of five planes (in Y-Z plane) were selected and pressure contours were plotted at those locations, starting at a distance of 24.7 mm from the entrance and an incremental length of 0.65 mm along channel length, covering a unit elliptical fin. These contours were compared with contours of straight

fin channel for the same location as shown in Figure 5.3B. The pressure values which correspond to 24.7 mm, 25.35 mm, 26 mm, 26.65 mm and 27.3 mm location are 494 Pa, 465 Pa, 435 Pa, 430 Pa and 450 Pa respectively. It was observed from the contours and graph that the pressure at the leading edge of the elliptical fin was high and then decreased along the fin up to the trailing edge after which it suddenly rose at the leading edge of the subsequent fin. This was because the fluid experiences converging and diverging flow when it passes over a unit elliptical fin from leading to trailing edge. Also, the fluid starts retarding and approaching zero at the leading edge of subsequent fin contributing to further pressure rise in the channel. Similarly, for the heat flux of 65 W/cm^2, slightly higher values of local pressure drops were observed, as shown in Figure 5.3A(b).

5.2.3 Friction factor

Figure 5.4 illustrates the effect of elliptical fin angle on friction factor for various Reynolds numbers. Friction factor value determines the flow resistance in channel. Higher value of friction factor implies higher flow resistance and vice versa. Friction factor mainly depends on the relative values of pressure drag force and velocity of fluid. The friction factor decreases with an increase of Re for both SFMC and EFMC's as shown Figure 5.4 and it can be explained from fanning equation (Eq.3.18). An increasing Re, increases fluid velocity and this velocity becomes more dominant than pressure drag force, resulting in decrease of friction factor. The friction factors for 2º EFMC at various Re-174, Re- 261, Re-436, Re- 610 and Re-784 are as 0.041, 0.033, 0.028, 0.271 and 0.0269 respectively. It can be concluded from the results that the 2º EFMC showed a constant friction factor for Re greater than 436 for heat fluxes 50 W/cm^2.

For constant Re, at heat flux of 50 W/cm^2, an increasing elliptical fin orientation angle increases friction factor which means flow resistance increased with an increase in fin angle. This is because higher angled EFMCs are associated with higher pressure drag which leads to higher friction factor in the channel. The same trend is observed at heat flux of 65 W/cm^2 which can be seen from Figure 5.4(b). The maximum friction factor 0.0837 is observed in 12º EFMC at Re 174 and for heat flux of 50 W/cm^2.

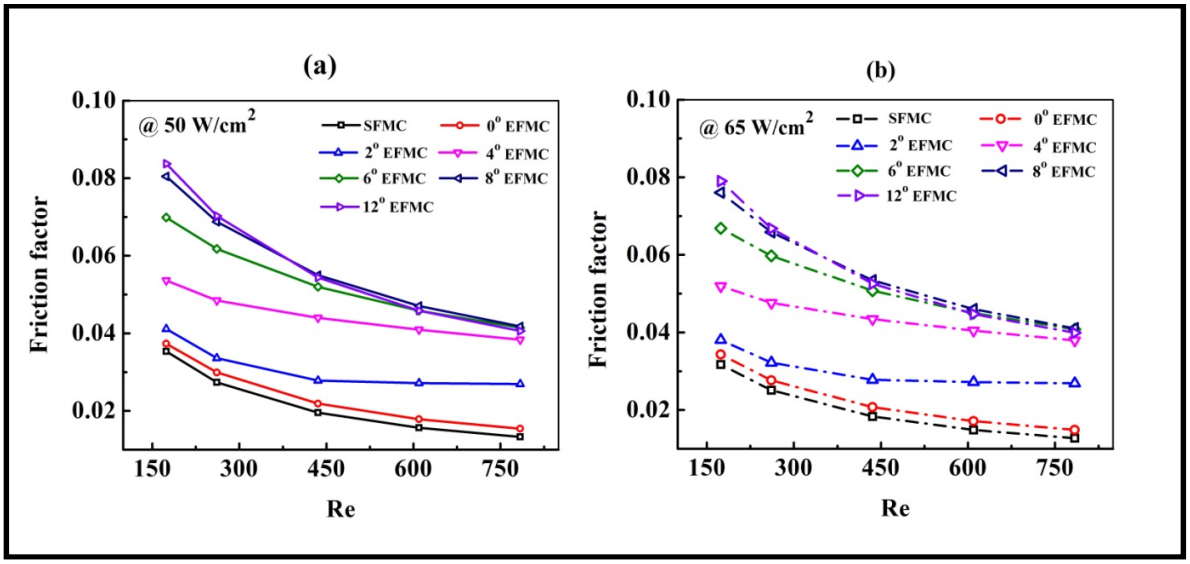

Figure 5.4 The friction factor of straight fin and elliptical fin microchannels for (a) 50 W/cm^2 b) 65 W/cm^2

5.3 Heat transfer characteristics

5.3.1 Average wall temperature

The effect of average wall temperature versus Reynolds number (Re) for various elliptical fin angles is shown in Figures 5.5(a) and (b) for two different heat fluxes (50 W/cm^2 and 65 W/cm^2). In general, the average wall temperature decreases for all

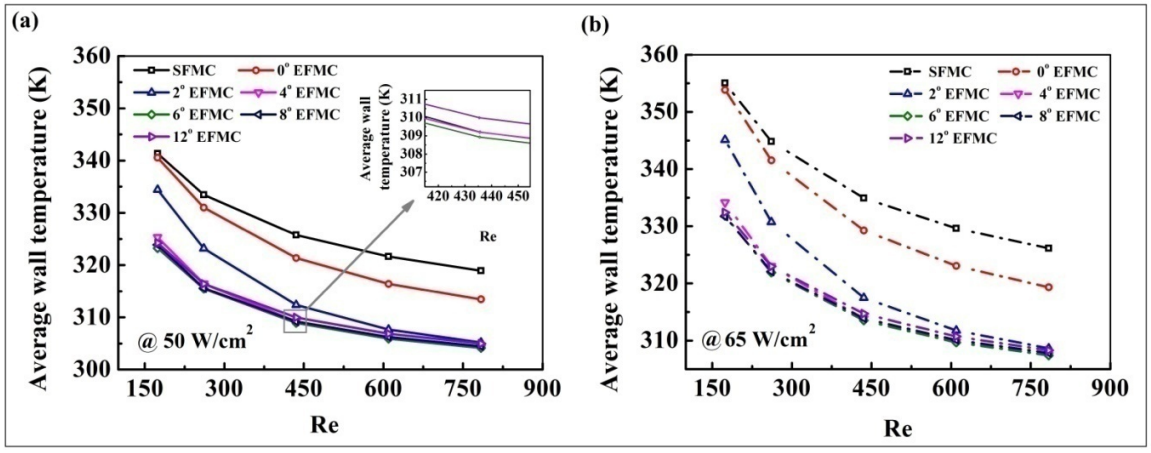

Figure 5.5 Variation of average wall temperature for various angles of elliptical fin arrangement with flow direction for (a) 50 W/cm^2 (b) 65 W/cm^2

configurations and heat fluxes with Re, whereas this decrease in the average wall temperature of angled elliptical fin was found to be higher when compared to SFMC. This is because of the same reason explained in the previous section. For a constant Re, by increasing the elliptical fin angle from 0º to 6º the wall temperature drops down and then it rises gradually for further increasing fin angle. This is because directing the secondary flow into the mainstream interrupted the boundary layer and promoted better mixing in the channel. Hence, low wall temperatures were identified for 0º-6º elliptical fins. However, a further variation of the elliptical fin angle from 6º to 12º increases the wall temperature for both heat fluxes (50 W/cm^2 and 65 W/cm^2). This is mainly due to retarded fluid velocity caused by the widening of the secondary channel flow area as shown in Figure 5.8C.

Also, it is observed from Figures 5.5(a) & (b) that the reduction of average wall temperature decreases with both fin angle and Re. The average wall temperature for SFMC was 325.76 K (52.76 ºC) at Re 436 and heat flux of 50 W/cm^2. For the same Reynolds number and heat flux, 0º, 2º, 4º, 6º, 8º, and 12º EFMC showed an average wall temperature of 321.34 K (48.34 ºC), 312.36 K (39.36 ºC), 309.21 K (36.21 ºC), 308.93 K (35.93 ºC), 309.20 K (36.20 ºC) and 309.99 K (36.99 ºC), respectively. The percentage of wall temperature reduction corresponding to the above angles was 8.37 %, 25.39 %, 31.37 %, 31.89 %, 31.39 %, and 29.89 % respectively. For the same heat flux, the highest and lowest wall temperature reduction were noted as 32.30 % (305.92 K) at 6º elliptical fin corresponding to Re 610 and 1.18 % (340.56 K), and at 0º elliptical fin angle corresponding to Re 174 respectively. A similar trend was observed for heat flux of 65 W/cm^2 as shown in Figure 5.5(b).

5.3.2 Local wall temperature

Figure 5.6A depicts the local wall temperature profile of straight and 2º elliptical fin stream wise for heat fluxes of 50 W/cm^2 and 65 W/cm^2. At the channel inlet, local wall temperature is almost the same for straight and elliptical fins. However, the local wall temperature of the 2º elliptical fin along the stream direction falls below the local wall temperature of the straight fin.

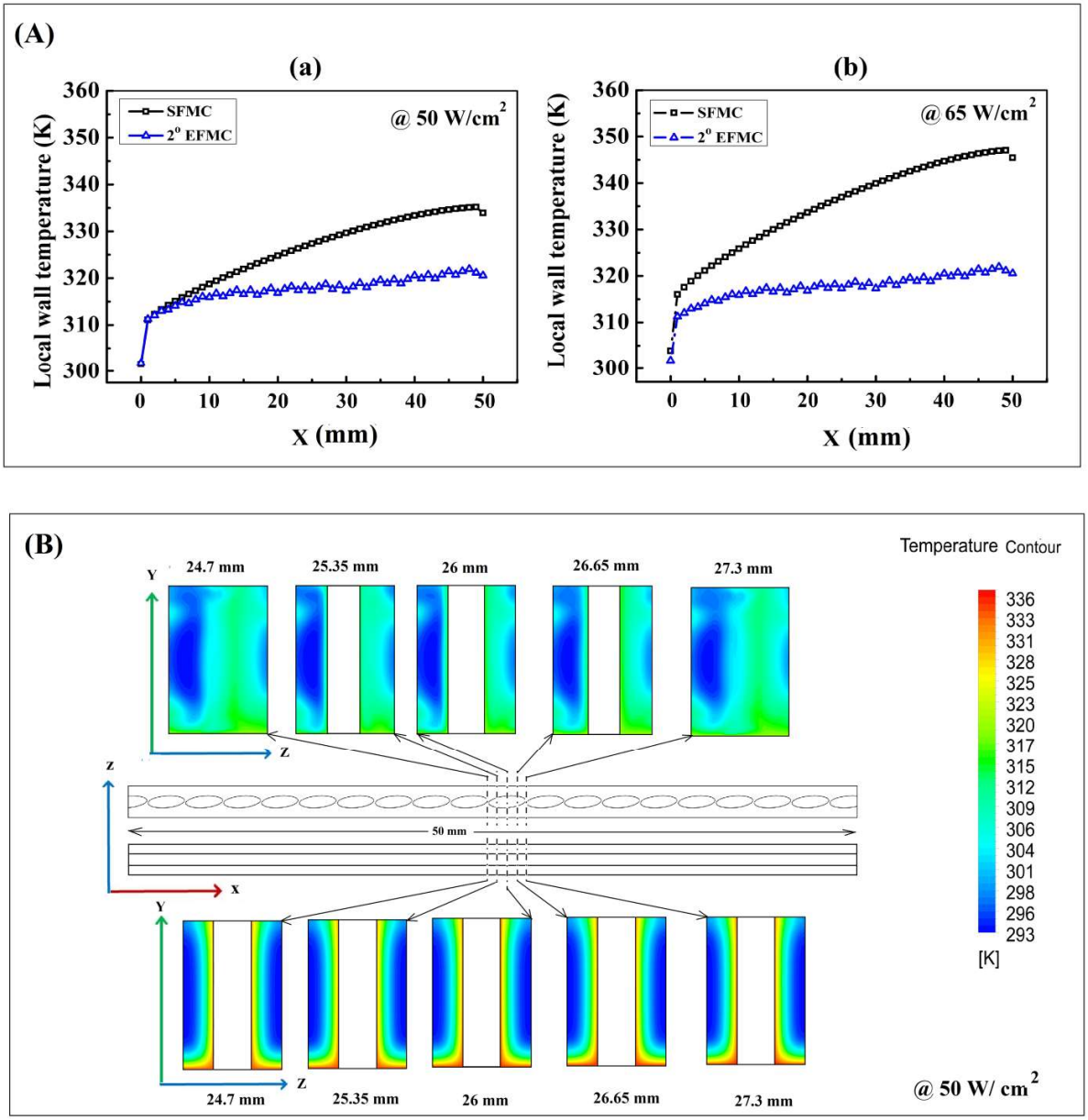

Figure 5.6 (A) The effect of local wall temperature along with the downstream of flow at Re 436 for (a) 50 W/cm^2 and (b) 65 W/cm^2 (B) temperature distribution at various locations (in Y-Z plane)

It is also observed from Figure 5.6A that wall temperature rise was gradual from inlet to outlet in EFMC. The wall temperature increase reduced by 13.32 ^{o}C for EFMC at Re of 436 for heat flux of 50 W/cm^2 relative to SFMC. For the same Re, and at heat flux of 65

W/cm^2, the wall temperature increase reduced by 22.78 ^{o}C for EFMC relative to SFMC. Therefore, elliptical fin channel can be used for higher heat flux applications. In addition to this, the temperature contours were plotted in planes perpendicular to stream direction (in the Y-Z plane) placed equally between the leading edge and trailing edge of an elliptical fin to cover one single fin. Starting with a plane of 24.7 mm from the inlet a total of five locations were selected with an incremental length of 0.65 mm. These contours were compared with contours of straight fin channel for the same location as shown in Figure 5.6B. It is also clear from contours that uniform fluid temperature distribution was noted in EFMC against SFMC. The reason for that is discussed in the above sections. The optimum average wall temperature was 312.36 K (39.36 ºC) at Reynolds number 436 for a heat flux of 50 W/cm^2.

5.3.3 Average Nusselt number

It can be observed from Figure 5.7A that the average Nusselt number (Nu_{avg}) increases by increasing elliptical fin angle from 0º to 6º and then it decreases by further increasing fin orientation angle for all Re. Orienting fin angle from 0º to 12º leads to diversion of the fluid stream from primary channel to secondary channel, which in turn disrupts boundary layer development. Apart from that, re-establishment of boundary layer starts at the beginning of each elliptical fin indicated in Figure 5.7B(b). It reduces thermal and hydraulic boundary layer thicknesses as shown in Figure 5.7B(b) and promotes better mixing of fluid in the channel. However, for fin angles oriented beyond 6º, a greater volume of fluid flows in the secondary channel than the primary channel due to the widening of secondary channel and narrowing of the primary channel with an increase of fin angle (Figure 5.7C). This leads to retardation of fluid in the secondary channel resulting in an increase of temperature gradient between channel walls and fluid. Therefore, Nu_{avg} increases with an increase of fin angle up to 6º, beyond which it deteriorates. For heat flux of 50 W/cm^2, highest Nu_{avg} of 28.61 is obtained for 6º at Re 784 which is 215 % higher when compared to SFMC. For the same heat flux condition, an optimal Nusselt number Nu_{avg} of 16.64 is observed at 2^{o} for Re 436, (which is 116 % higher compared to that of SFMC) that corresponds to highest performance factor (1.52).

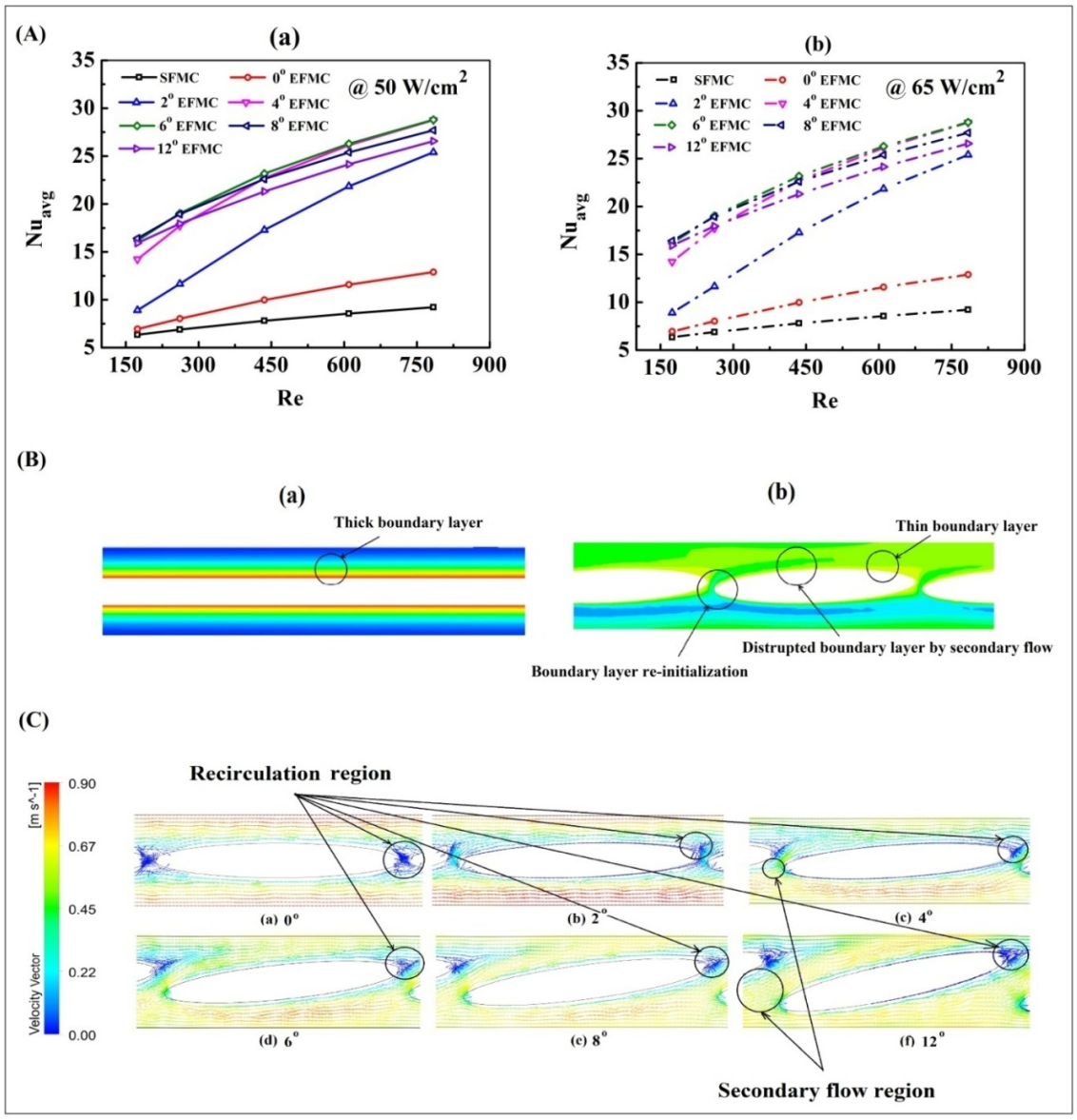

Figure 5.7(A) Variation of average Nusselt number with flow direction for different angles of elliptical fin arrangement for (a) 50 W/cm^2 (b) 65 W/cm^2 **(B)** Temperature contours at mid plane (X-Z), Re- 436 for (a) straight fin microchannel (SFMC) (b) 2^o elliptical fin microchannel (EFMC) **(C)** Velocity vectors of various elliptical fin microchannel (X-Z plane, 23 mm from inlet) at Re - 436, heat flux 50 W/cm^2

Also, for all Re, the rise of Nu is lower for 0º compared to other elliptical fin orientations considered in the study. This is because of strong recirculation prevailing at the trailing edge of the elliptical fin blocks the secondary flow, which can be seen clearly from Figure 5.8C. Therefore, there is very poor fluid mixing in 0º angled EFMC. The same trend is observed for both heat flux conditions such as 50 W/cm^2 and 65 W/cm^2 as shown in Figure 5.8A(a) & (b). Nusselt number enhancement % for various EFMCs (flow ranges from Re-174 to 784) is also presented in Table 5.3.

Table 5.3 Nusselt number enhancement % for various EFMCs over SFMC.

Type of channel	Nusselt number									
	Heat flux 50 W/cm^2					Heat flux 65 W/cm^2				
	Re-174	Re-261	Re-436	Re-610	Re-784	Re-174	Re-261	Re-436	Re-610	Re-784
0º EFMC	8.8	15.8	27.7	35.8	41.0	9.3	16.5	27.9	35.2	39.8
2º EFMC	35.6	40.6	116.0	153.9	176.2	40.3	69.3	121.6	155.1	175.4
4º EFMC	119.4	120.0	191.2	207.2	214.8	123.9	157.2	190.9	205.2	211.9
6º EFMC	152.8	138.0	198.3	209.3	215	154.7	176.0	197.1	207.0	212.3
8º EFMC	157.7	137.8	191.6	198.9	203.3	158.5	174.8	189.9	196.5	200.4
12º EFMC	139.5	122.8	170.7	179.5	185.8	150.8	160.5	173.2	182.1	188.1

5.3.4 Local Nusselt number

Figure 5.8 shows the variation of local Nusselt number along the stream direction for straight fin and elliptical fin (2º). A total of 50 locations were selected from inlet to outlet of channel with an incremental length of 1mm as shown in Figure 5.8(c). The equation for local Nusselt number is provided in the data section (Eq.3.16). It can be seen from Figure 5.8(a) & (b), that the Nusselt number is large at the inlet of the channel for both SFMC and

EFMC since the boundary layer is initiated at the inlet where its thickness is very small. In subsequent flow, the boundary layer

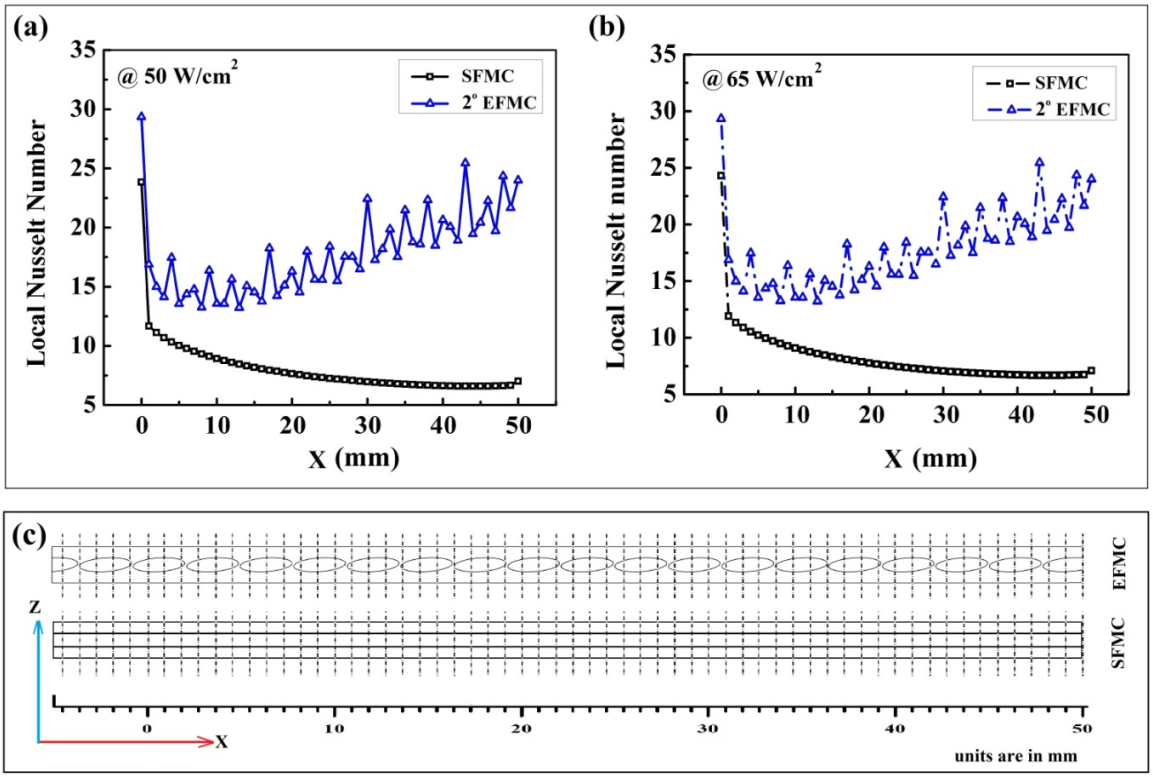

Figure 5.8 The effect of Nusselt number along with the downstream flow for straight fin microchannel (SFMC) and 2° elliptical fin microchannel (EFMC) at Re 436 for (a) 50 W/cm^2 and (b) 65 W/cm^2 (c) 50 locations long the channel length in elliptical fin microchannel.

thickness increases and becomes constant along with downstream in the case of a straight fin. Elliptical fins oriented at an angle induce secondary flow in the channel that disrupts the boundary layer development at the trailing edge of each fin (Figure 5.7B). Furthermore, flow area along the flow stream is varied continuously that causes fluctuation in fluid velocity (Figure 5.7C). Therefore Nusselt number varies locally along the downstream of the channel. Optimum average Nu is noted for 2° elliptical fin as 16.64 at a Reynolds number of 436 and heat flux of 50 W/cm^2. The trend is identical to the heat flux of 65 W/cm^2 with little increment, as shown in Figure 5.8(b).

5.3.5 Velocity and temperature contours

Figure 5.9 represents the velocity and temperature contours of straight and EFMC at the mid-plane of fluid along the channel length. It is clear from Figure 5.9 that high velocity gradient from the wall to the fluid core in the case of straight fin channel can result in large boundary layer thickness. In the case of elliptical fin channel lower boundary layer thickness is reported against SFMC. Lower boundary layer thickness promotes more heat transportation from wall to fluid core. The resulting decrease of velocity and temperature gradient from the wall to the fluid core is shown in Figure 5.6. On the contrary, the heat dissipation capabilities (fall of Nusselt number) of the EFMC heat sink deteriorated at angles more than 6º, which is clearly shown in Figure 5.7A. This is because the secondary flow passage is wider than the primary passage which is attributed to resistance in fluid flow. In addition to this, fluid entry losses are larger at higher angles.

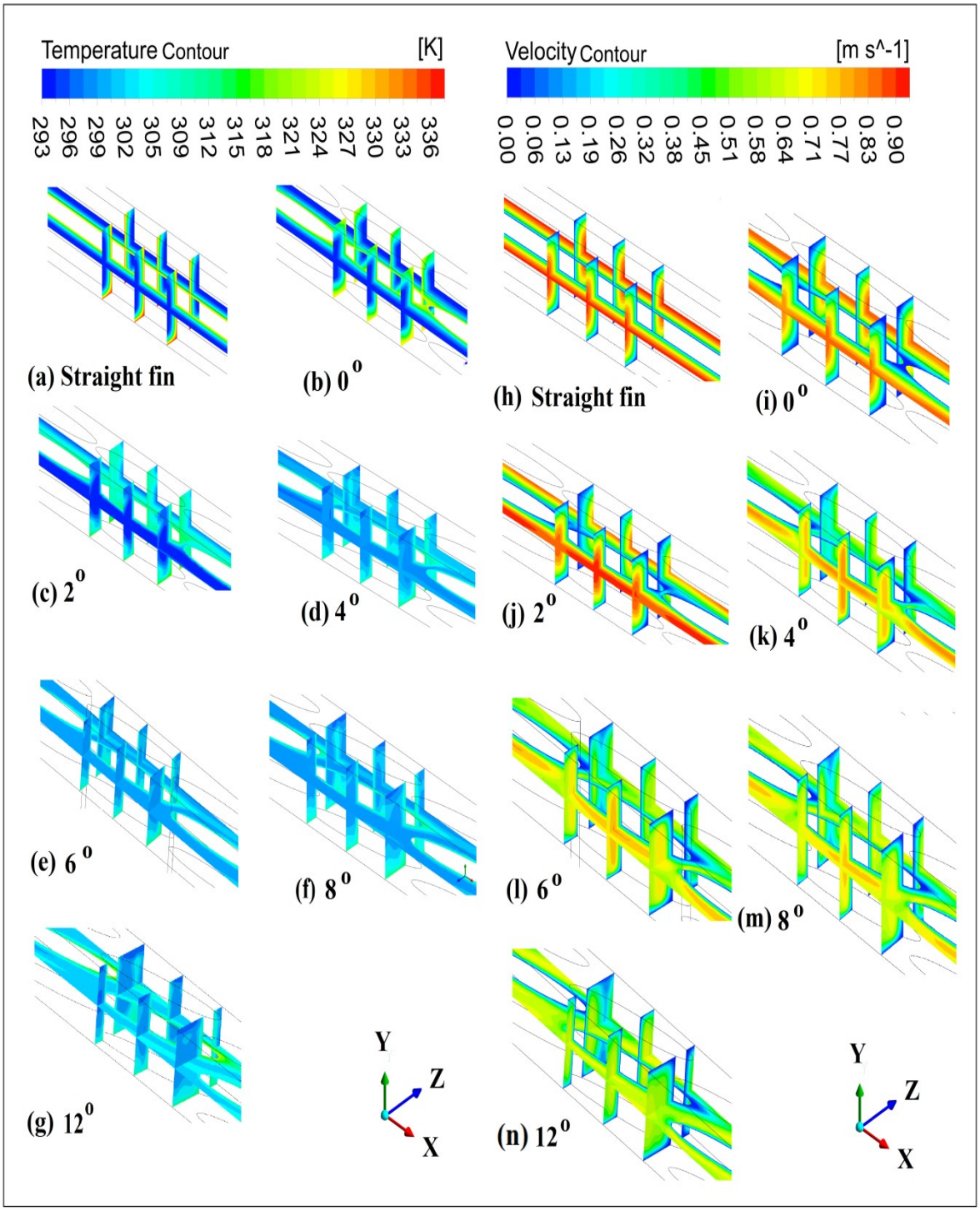

Figure 5.9 Temperature and velocity distribution of straight and elliptical fin at Reynolds number 436, heat flux of 50 W/cm^2 (23 mm-29 mm from inlet)

5.3.6 Performance factor

Figure 5.10 illustrates the influence of elliptical fin angle on the cooling performance of the heat sink. It is to be noted that the performance of EFMC is sensitive to Reynolds number (Re) and fin angle. As the fin angle increases, the performance factor starts increasing and reaches to peak, and tends to decrease thereafter. This behaviour is found to be similar for all Re.

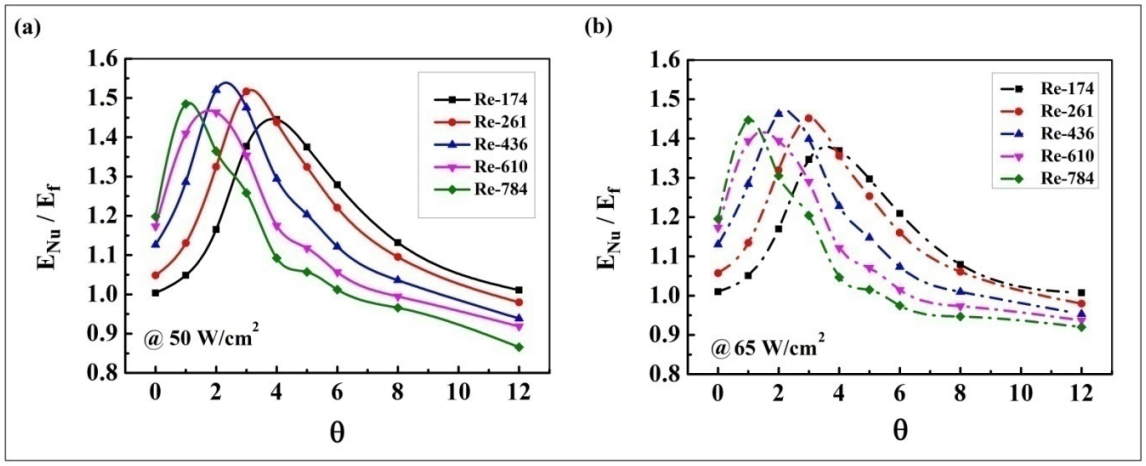

Figure 5.10 The effect of performance factor for various angles of elliptical fin arrangement with flow direction for (a) 50 W/cm^2 b) 65 W/cm^2

It is interesting to note from Figure 5.10 (a), that at lower Re, peak performance factor (PF) value shifted to higher angle side and for higher Re, peak performance factor shifted to lower angle side. This was mainly due to a rise in friction factor that is more dominant than an increase in Nu at higher Re. PF for various orientations of elliptical fin 0º, 2º, 4º, 6º, 8º, and 12º at Re 436 and heat flux of 50 W/cm^2 are 1.13, 1.52, 1.29, 1.12, 1.04, and 0.94 respectively. The highest performance factor 1.52 was noted at Re of 436 when the fins are positioned 2º to fluid flow at a heat flux of 50 W/cm^2. Whereas 4 º EFMC showed better PF for lower Re (≤261). A similar trend was observed for a heat flux of 65 W/cm^2 as shown in Figure 5.10 (b).

5.4 Conclusion

Thermal performance and flow characteristics of elliptical fin microchannel with different orientations (0º - 12º) and two different heat fluxes (50 W/cm^2 and 65 W/cm^2) were investigated and compared with straight fin microchannel. The present design originates secondary fluid paths and boundary layer re-initialization at each fin. This resulted in enhancement of heat transfer capabilities in the channel. Some of the key points are as follows:

- For both heat fluxes, at constant Re, a gradual rises in pressure drop was observed with an increasing elliptical fin angle (0°- 12°), whereas a rapid increase in pressure drop was noticed with increase in Re (174-784). Also figured out that pressure penalty corresponding to highest performance factor (1.52) was as low as 15 %.
- Average wall temperature of the channel declined by increasing elliptical fin angle from 0º- 6º, but on further increasing the fin angle, it shot up. The highest percentage of wall temperature reduction was 32.30 % at 6º elliptical fin orientation, which corresponds to Re and heat flux are 610 and 50 W/cm^2 respectively. For the same heat flux, 2º elliptical fin orientation showed optimum wall temperature reduction of 25.39 % at Re of 436.
- Nusselt number was augmented with fin angle (0º - 6º) because of the thin boundary layer and re-initialization. However, Nusselt number deteriorated for fin angle more than 6º due to decrease in fluid velocity in the secondary channel; it was caused by the combined effect of widening of secondary flow region and narrowing of the primary flow region**.**
- Among all the orientations considered in the study, elliptical fin oriented to 2º outperformed against straight fin microchannel heat sink with Nu increment of 116 %, average wall temperature reduction of 25.39 %, and a performance factor of 1.52 at Re 436 and heat flux of 50 W/cm^2.
- For lower Reynolds number (≤ 261), at both heat flux conditions, the 4º elliptical fin microchannel showed better performance factor compared to other elliptical fin orientations.
- Elliptical fin microchannel can be used for higher heat fluxes application without compromising their reliability and functionality due to lower rise in wall temperature compared to straight fin microchannel.

CHAPTER 6

Parametric analysis of elliptical fin microchannel heat sink

This chapter describes the impact of important parameters, such as fin ellipticity ratio, fin orientation angle, fin height and fin to fin centre distanceon thermal performance in steady state laminar zone. Numerical analysis was performed for a range of Re 100-768 and higher heat flux of 65 $W/cm^2$and this was compared with straight fin microchannel. In addition, other parameters such as average wall temperature, Nusselt number, friction factor and performance factor variation with Reynolds number were investigated and discussed in detail.

6.1 Numerical Modelling

Figure 6.1 depicts a 3D view of elliptical fin microchannel (EFMC) heat sink of 50 mm × 50 mm × 5.5 mm size. A total of forty-nine elliptical fin rows with a lateral spacing of 620 µmand twenty fins with a longitudinal spacing of 2600 µm were modeled on the substrate. The elliptical fin has a height of 1500 µm, the semi-major axis and minor axis of 1260 µm and 190 µm respectively. This design is a substitute for the straight fin microchannel (SFMC) heat sink of the same dimensions. The complete geometrical details of both the microchannel heat sink were shown Table 6.1.Water was used as cooling fluid, and thermal conductivity and viscosity were a function of temperature. Additionally, heat sink and coolant properties are provided in Table 3.2.

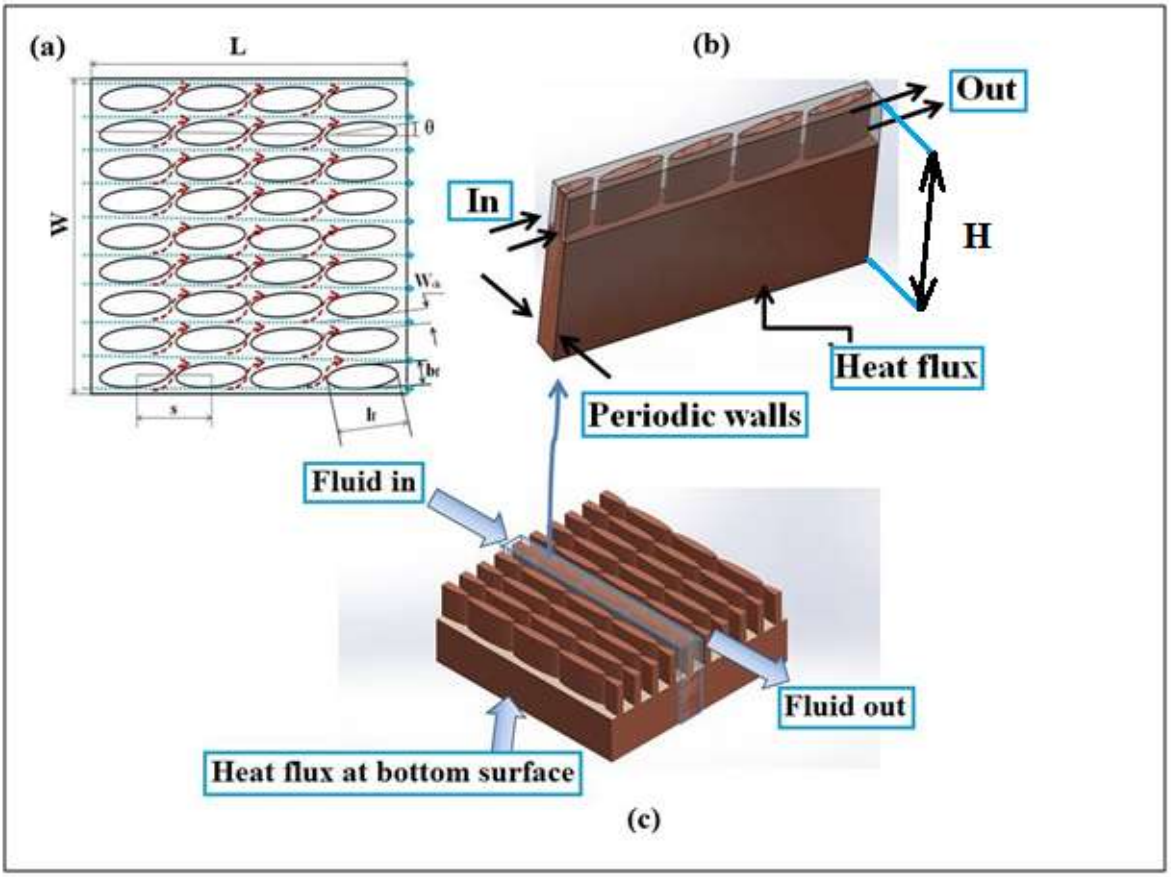

Figure 6.1 Geometry of elliptical fin microchannel (not scaled) (a) 2D view (b) computational domain (c) 3D Microchannel heat sink

Initially in this study, five distinct ellipticity ratio (ER) microchannel models (ER-0.15, ER-0.175, ER-0.20, ER-0.225 and ER-0.25) as shown in Figure 6.2 were modeled and analyzed while maintaining a constant fin volume, in order to find the best performing ellipticity ratio microchannel model. Then for the best ellipticity ratio microchannel, the fin orientation angle

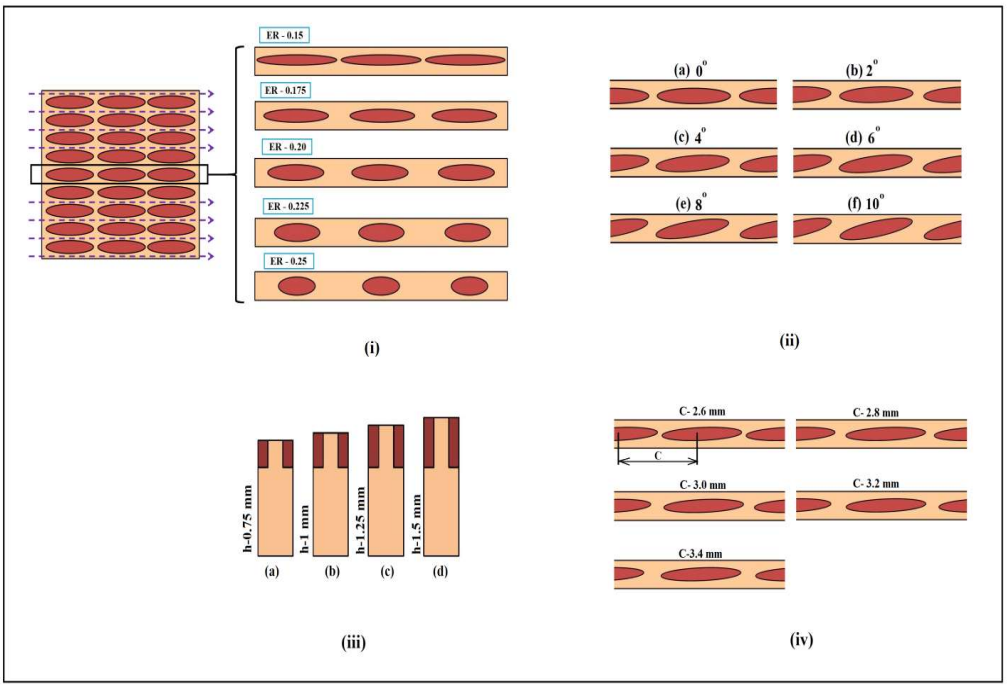

Figure 6.2 Effect of various parameters on elliptical fin microchannel (not scaled) (i) ellipticity ratio (ii) fin orientation angle (iii) fin height (iv) fin to fin centre distance

was varied from 0° to 12° with increment of 2° to get optimum performance angle as shown in Figure 6.2 (ii). Consequently, for optimum angled microchannel, the fin height was varied from 750 µm to 1500 µm with increments of 250 µm as illustrated in figure 6.2 (iii). Finally, for best fin height microchannel model, the centre distance between the fins was altered from 2600 µm to 3400 µm with an increment of 200 µm as shown in figure 6.2 (iv) to obtain the best elliptical fin microchannel model.

Table 6.1 Dimensions of EFMC were investigated numerically.

Characteristic	**Straight channel**	**Elliptical channel**
Material	Copper	
Foot print, Width × length (mm)	50 × 50	
Main channel width, W_{ch} (μm)	620	
Channel depth, H (μm)	1500	
Fin width, W_f (μm)	380	
Fin rows, N	49	
Fins per row	-	20
Fin centre distance, S (μm)		2600
Semi-major axis, l_f (μm)	-	1260
Semi-minor axis, b_f (μm)	-	190
Orientation angle, θ (deg)	-	0-12
Ellipticity ratio	-	0.15-0.35
Aspect ratio, α		0.8-9.6

6.2 Effect of ellipticity ratio

In this section, five elliptical fin microchannel (MC) models with different ellipticity ratio (ER) were studied numerically by investigating the effect of ER on hydrothermal performance. ER is termed as the ratio of minor axis to major axis of the elliptical fin. The five elliptical fin MC models (ER-0.15, ER-0.175, ER-0.2, ER-0.225, and ER-0.25) were compared with straight fin MC. In addition to that, other parameters like average wall temperature, Nusselt number and friction factor variation with Reynolds etc., were examined and discussed in detail.

6.2.1 Pressure drop characteristics

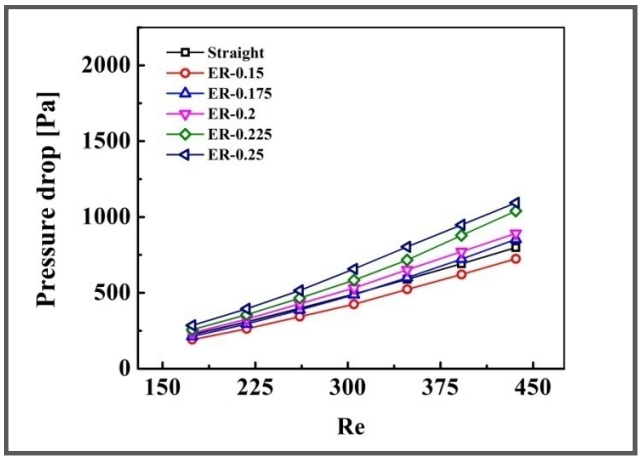

Figure 6.3 Effect of ellipticity ratio on pressure drop

Figure 6.3 shows that pressure drop variation for Reynolds number (Re) range of 174-436. The pressure drop in the channel increases with an increase in Re and ER. This increase in pressure drop with ER is due to an increase of fin profile resistance and flow separation that induces large wake region behind the fin. Therefore, the smallest ER (0.15) MC model shows lower pressure drop while the largest ER (0.25) model shows higher pressure drop. This is mainly due to the formation of very large wakes behind the fin leads to high disturbance and increases pressure drop in the channel. Hence, a higher pressure drop is observed for large ER MC models.

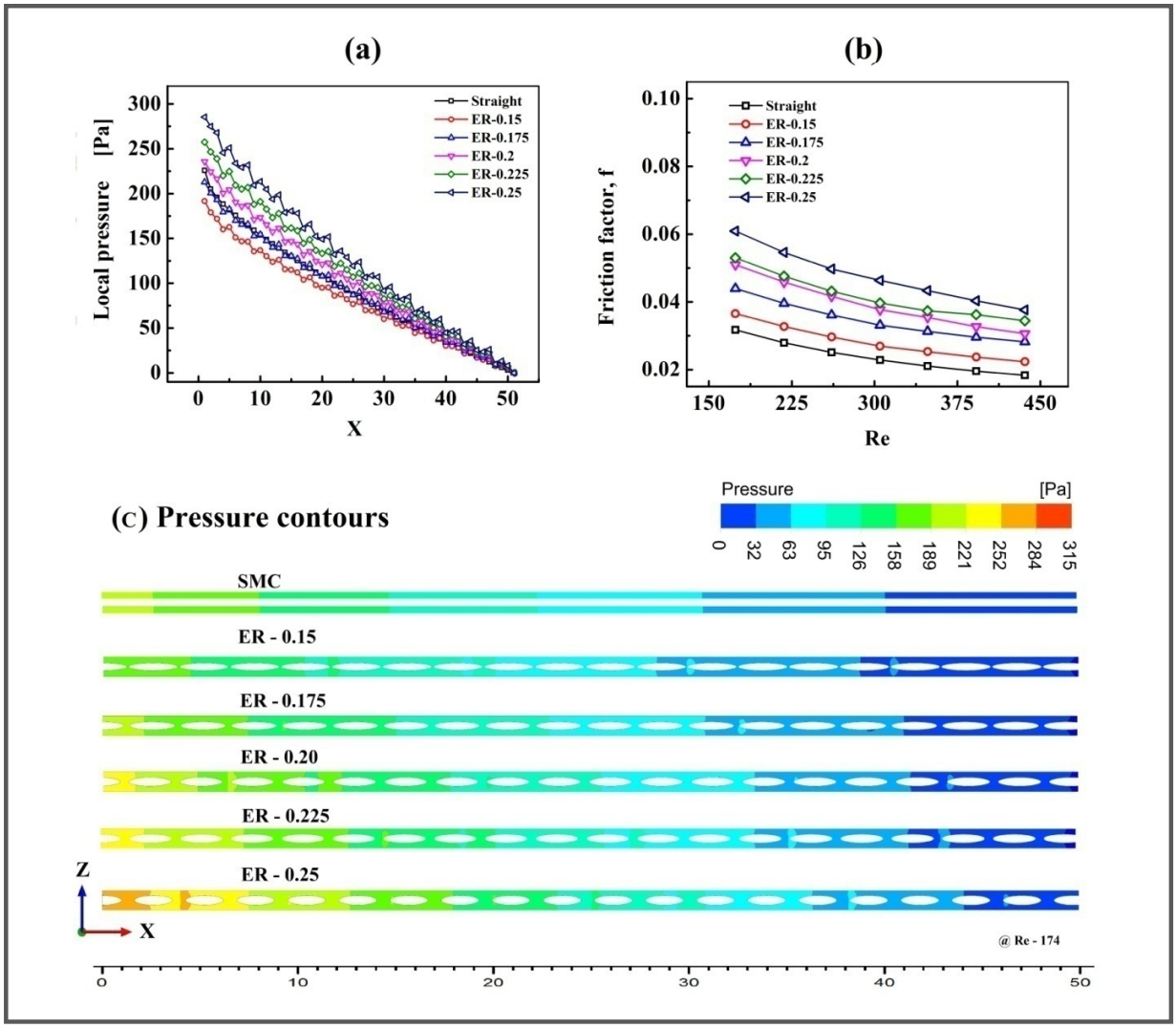

Figure 6.4 (a) pressure variation along the channel length (b) effect of friction factor with Re (c) pressure contours of elliptical fin models and straight fin.

Figure 6.4 depicts the pressure variation in the entire channel. For all Elliptical MC models and straight MC, the pressure along the channel length decreases globally as can be seen from pressure contours shown in Figure 6.4(c). But there was local rise and fall of pressure along the channel length in elliptical MC models. This is because the fluid experiences contraction and expansion while it passes over elliptical fins. Therefore local rise and fall of pressure was observed along the channel. It was also noted that the local pressure curve was steeper for higher ER MC than lower ER MC. Similarly, the friction factor increases with ER and reduces with Re as shown in Figure 6.4(b). This rise in ER

increased flow resistance caused by flow obstruction at each fin. Hence, friction factor increases with ER. The friction factors of elliptical fin models ER-0.15, ER-0.175, ER-0.20, ER-0.225 and ER-0.25 model were 0.036, 0.043, 0.050, 0.053 and 0.060 for Re 174 respectively.

6.2.2 Velocity streamlines

Figure 6.5 represents velocity stream lines for various ellipticity ratios along the channel length. Increase in ER reduces fin length and increases fin width resulting in decrease of fin to fin gap along the length and reduction of fluid flow passage through the main channel. This increase in ER accelerates the fluid velocity in the channel and promotes formation of wake regions behind the fin which in turn reduces boundary layer thickness by mixing the fluid adequately within the laminar region. Hence, heat carrying capacity of fluid increases with increase in ER. But for higher Re of 392 and 436 at an ER of 0.25, average wall temperature declines drastically due to the formation of very large wake region, which disturbs the flow greatly and leads to higher pressure drop in the channel.

In addition to this, for a constant ER, an increase in velocity of fluid also improves the heat dissipating capacity but there is a chance of formation of large wake region, which leads to higher pressure drop in the channel. Therefore, higher velocities were not considered in this study either.

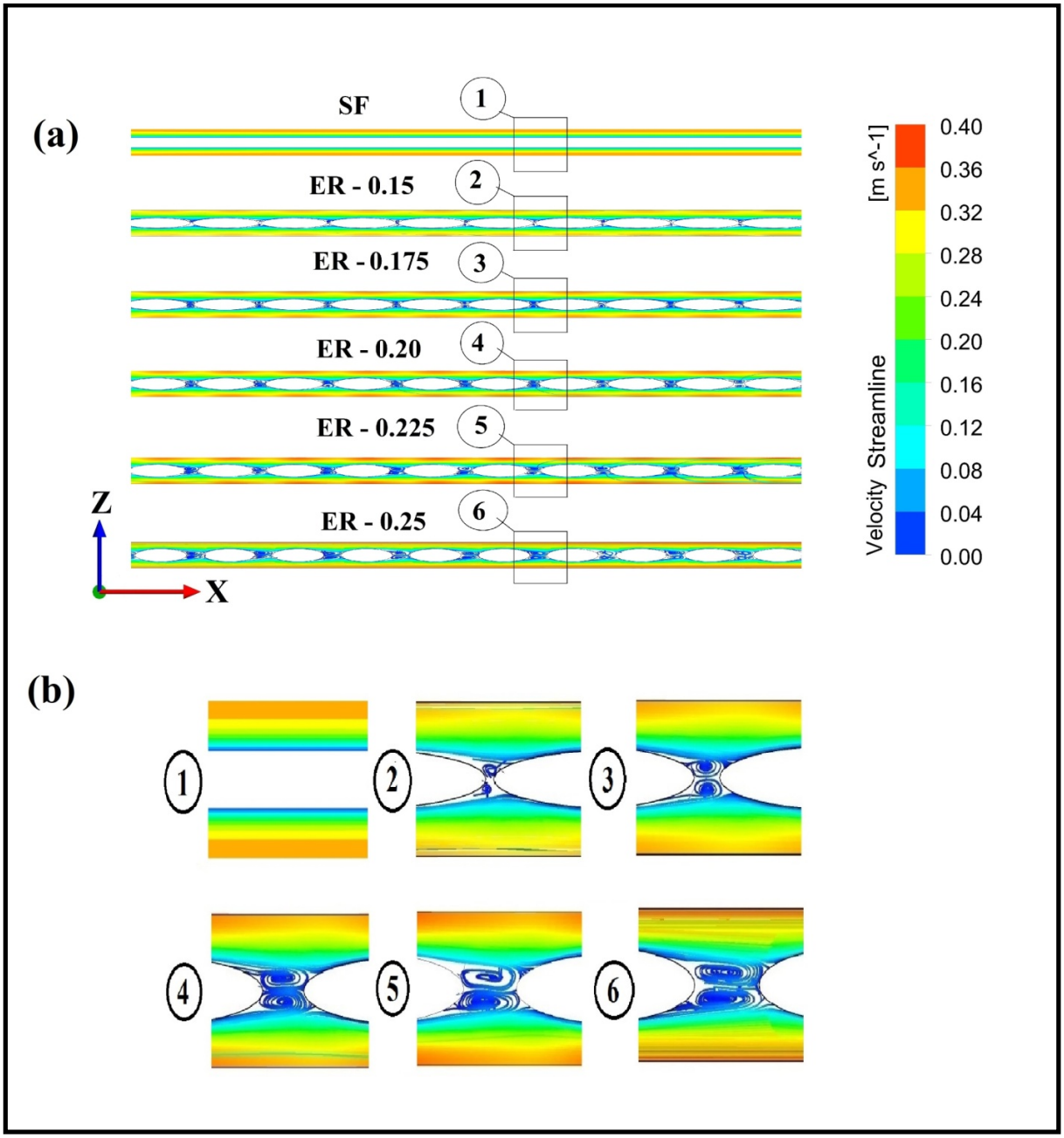

Figure 6.5 (a) velocity stream lines of elliptical fin models and straight fin (b) enlarged view of velocity stream lines between fin gaps

6.2.3 Thermal characteristics

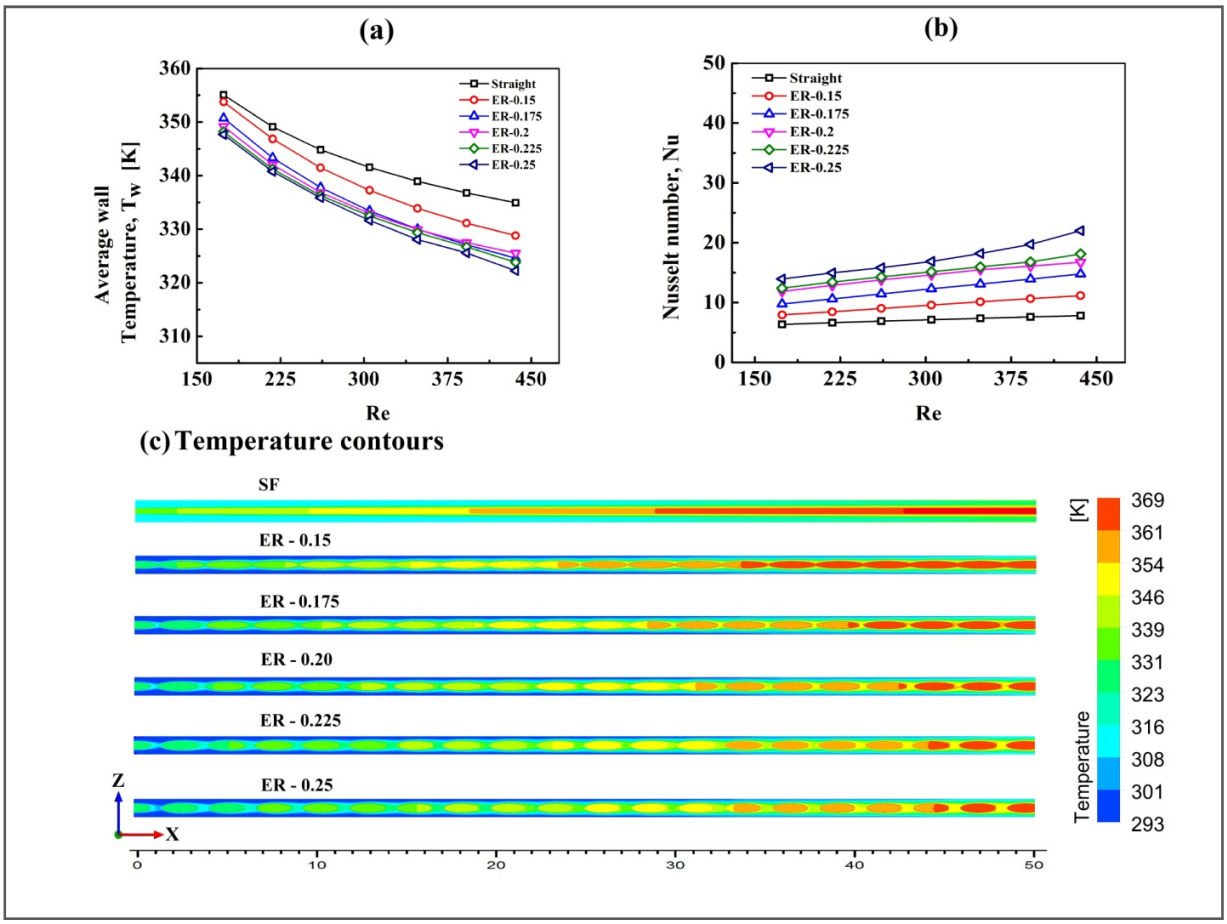

Figure 6.6 (a) effect of ER and Re on wall temperature (b) effect of ER and Re on Nusselt number (c) temperature contours of elliptical fin models and straight fin.

Figure 6.6(a) shows the average wall temperature variation with Reynolds number (Re) and ER. For a constant ER, increase in Re decreases the average wall temperature of the channel. This is due to an upswing in fluid velocity, which absorbs high heat from the channel. Thus heat dissipating capacity of fluid is rapidly augmented in the channel. Moreover an increase in ER further decreases average wall temperature due to intensified fluid mixing in the channel. The maximum temperature reduction for elliptical fin models ER-0.15, ER-0.175, ER-0.20, ER-0.225 and ER-0.25 over straight fin MC was 1.58 %, 5.28 %, 7.17 %, 8.38 % and 9 % respectively. It can also be noted from figure 6.6(a) that the decrease in average wall temperature was more prominent with Reynolds number compared to ER. Similarly, an increasing ER would enhance Nusselt number as depicted from Figure

6.6(b). An increase in Reynolds number rapidly improves Nusselt number due to increase in of fluid velocity with Re. The Nusselt numbers for different ERs (ER-0.15, ER-0.175, ER-0.20, ER-0.225 and ER-0.25) at Re of 174 were 7.9, 9.7, 11.8, 10.3 and 13.9 respectively. For the same Re, the percentage increase in Nusselt number for various ellipticity ratios ER-0.15, ER-0.175, ER-0.20, ER-0.225 and ER-0.25 was 24.96 %, 53.8 %, 86.9 %, 67 %, 95.3 % and 119.6 % respectively over straight fin MC. The maximum Nusselt number of 22 was reported for ER-0.25 at Re of 436, which is 182 % more than that for straight microchannel.

6.2.4 Performance factor

Performance factor is defined as the ratio of relative Nusselt number of elliptical to straight fin MC by relative friction factor of elliptical to straight fin MC. Figure 6.7 shows that at a constant Re of 174, the performance factor improved initially with ER (up to ER-0.2) and then it deteriorated for increasing ER. This was mainly because the rise in relative Nusselt number was more dominant than the rise in relative friction factor when ER < 0.2. Thereafter, (ER > 0.2) the rise in relative friction becomes more dominant than relative Nusselt number which results in a decrease in performance factor compared to ER-0.2 model. Out of all MC models, ER-0.20 model showed the highest performance factor. The performance factor of ER-0.20 model for various Reynolds numbers Re-174, Re-218, Re-261, Re-305, Re-348, Re-392 and Re-436 was 1.163, 1.184, 1.205, 1.238, 1.250, 1.269, and 1.285 respectively.

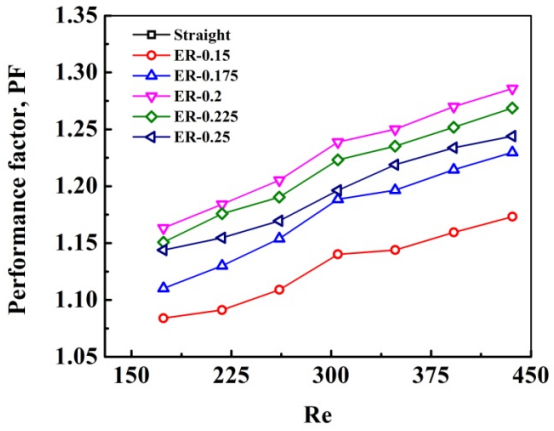

Figure 6.7 Effect of ER and Re on performance factor

Moreover, for larger ERs (ER > 0.225), increasing Reynolds number from 174 to 436 improved the PF gradually after which it declined rapidly. The performance factor of ER-0.25 model for various Re-174, Re-218, Re-261, Re-305, Re-348, Re-392 and Re-436 was 1.143, 1.154, 1.159, 1.160, 1.149, 1.139, and 1.130 respectively. This was due to rapid rise of friction factor of elliptical fin MC caused by the development of strong flow recirculation regions in the channel.

6.3 Effect of Fin orientation angle

From the previous section, the best ellipticity ratio microchannel model (ER-0.2) was determined. For this best ellipticity ratio microchannel model, the orientation angle was varied from 0^o to 12^o with an increment angle of 2^o, in order to examine the effect of orientation angle on thermal performance. Results revealed that the best ellipticity ratio model with a 2^o orientation angle exhibited the highest thermal performance among all angles tested, achieving a maximum performance factor of 1.37. Additionally, several other parameters, such as the average wall temperature, Nusselt number, and friction factor variation with Reynolds number, were thoroughly analyzed. Similar trends were observed with a slight variation in performance and other parameters when the elliptical fin of the best ellipticity ratio microchannel was oriented to 2^o, as discussed in Chapter 5.

6.4 Effect of Fin height

The best angled elliptical fin microchannel model (orientation angle 2^o and ER-0.2) was obtained from the previous section. For this angled elliptical fin microchannel model, fin height was altered from 0.7 5 mm to 1.5 mm at equal intervals of 0.25 mm. This resulted in a total of four elliptical fin MC models, which were then compared with a straight fin MC to assess the impact of fin height on hydrothermal performance. Additionally, several other parameters, including the average wall temperature, Nusselt number, and friction factor variation with Reynolds number were thoroughly examined.

6.4.1 Pressure drop characteristics

Figure 6.8 shows the effect of fin height on pressure drop variation. For all Reynolds number, the pressure drop decreases with increasing fin height and vice versa. This reduction in pressure drop for various fin heights is due to expansion of inlet channel area.

Therefore, to maintain constant Re, the fluid velocity was lowered at the entry of the channel which resulted in reduction in pressure. Moreover, the rise in fin height augments the contact area of the channel. Therefore frictional resistance increased with fin height as shown in Figure 6.8(b). For a constant Reynolds number of 174, pressure drop for EFH-0.75 mm, EFH-1 mm, EFH-1.5 mm, and EFH-1.25 mm was 500 Pa, 379 Pa, 320 Pa, and 279 Pa respectively. The percentage of fall in pressure drop with fin height is 54.8 %, 40 %, 29.5 % and 19 %, which corresponds to EFH-1.5 mm, EFH-1.25 mm, EFH-1 mm and EFH-0.75 mm over straight fin MC (SFM- 1.5 mm) respectively. An increase of pressure drop with fin height was evidenced from the pressure contours drawn at Reynolds number of 174.

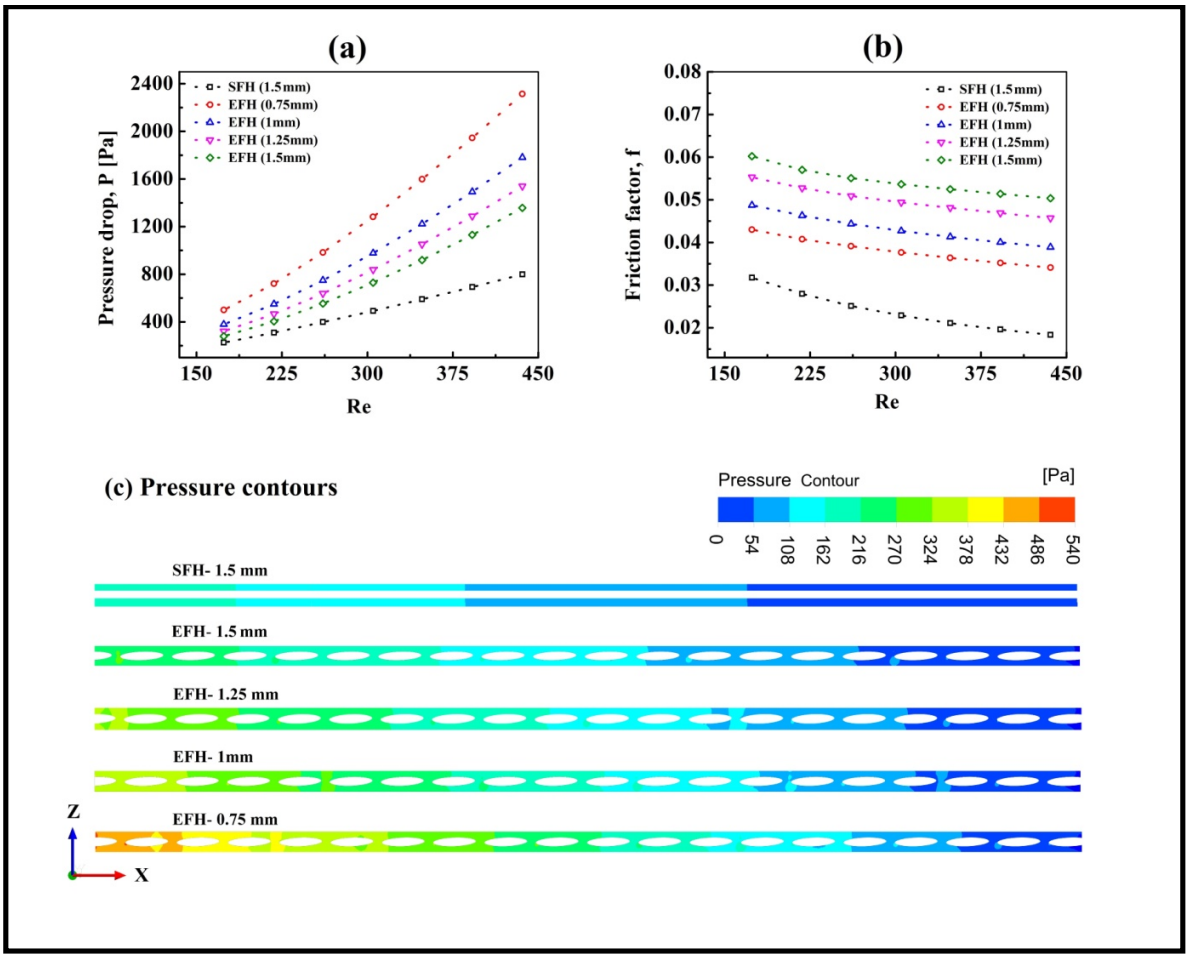

Figure 6.8 *(*a) pressure variation along the channel length (b) effect of friction factor with Re (c) pressure contours of elliptical fin models and straight fin.

It is also observed from Figures 6.8(a) and 6.8(c) that, at lower Reynolds number, the effect of fin height on pressure drop variation is minimal but for higher Reynolds numbers, the slope of pressure drop curve increases more quickly. This is because pressure drop is directly proportional to square of fluid velocity (eq. 3.18). Thus, pressure drop increases rapidly with Reynolds number. The maximum and minimum pressure drop were identified as 2314 Pa (EFH-0.75 mm at Re 436) and 225 Pa (SFM-1.5 mm at Re 174).

6.4.2 Thermal characteristics

From Figure 6.9, among the four MCs with different elliptical fin height, the wall temperature of channel increases with decreasing fin height. It indicates that decreasing fin height dampens wall temperature due to reduction in convective wall area of the channel. This reduction in convective area increases the wall temperature. Thus, higher wall temperatures were observed for lower height fin models as shown in Figures 6.9(a) & (c).

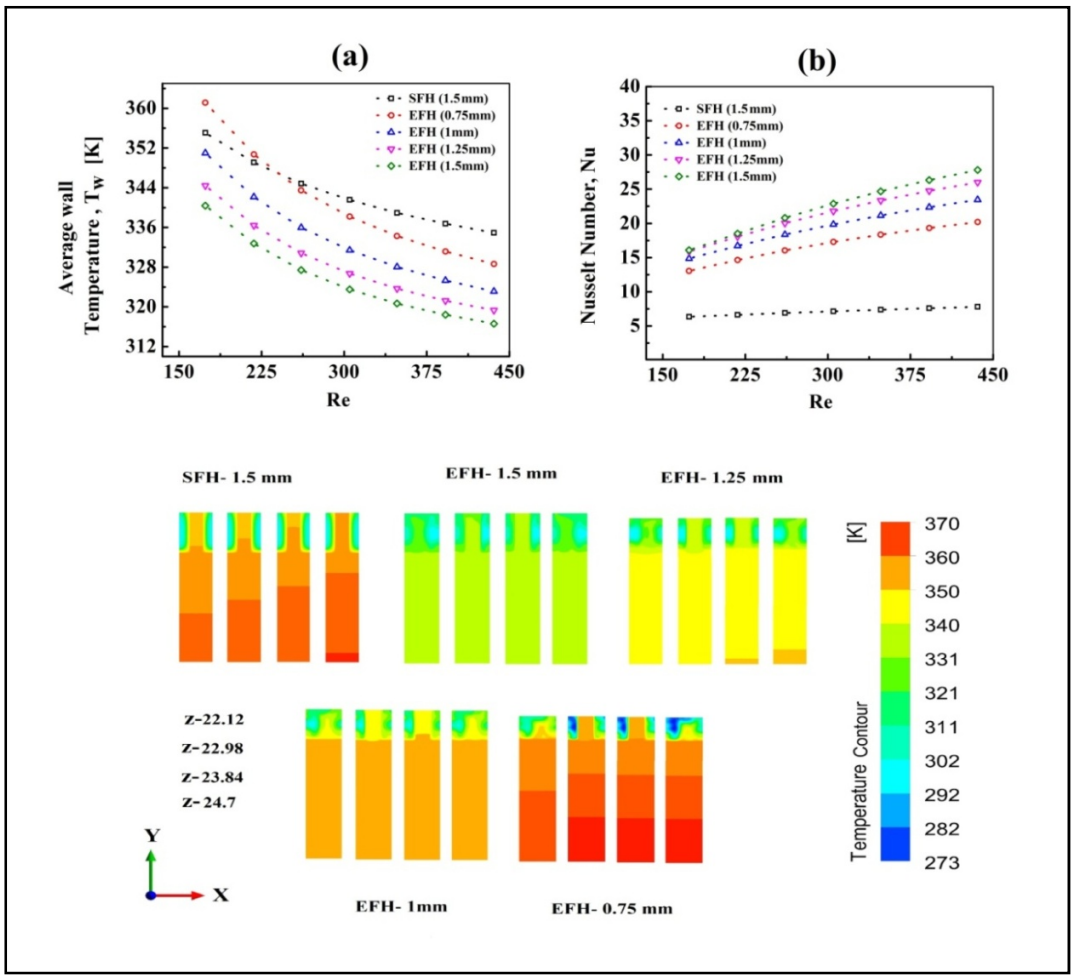

Figure 6.9 (a) effect of fin height on wall temperature for various Re (b) effect of fin height on Nusselt number for various Re (c) temperature contours of elliptical fin models and straight fin.

The percentage of wall temperature reduction for different elliptical fin height models over straight MC at Re 174 are 23.6 %, 17.2 %, 6.5 % and -9.8 % which correspond to EFH-1.5 mm, EFH-1.25 mm, EFH-1 mm and EFH-0.75 mm. In this, negative sign indicates wall temperature increment over straight fin MC, which implies that a fin height of < 1 mm channel is not beneficial to reduce wall temperature.

It is also observed form Figure 6.9(a) that the wall temperature of the channel further reduced by increasing Re. Among four elliptical fin models, EFH-1.5 mm model at Re-436 shows the maximum wall temperature reduction of 43.7 %. Similarly, increasing fin height

could enhance the Nusselt number and this enhancement reduces for further fin heights. The Nusselt number for different fin heights and for EFH-0.75 mm, EFH-1 mm, EFH-1.25 mm, and EFH-1.5 mm at Re 174 was 13, 14.7, 15.8, and 16 respectively. The maximum Nusselt number of 27.8 was reported for EFH-1.5 mm at Re 436, which is 256 % more than the straight microchannel. In addition to this, an increasing Reynolds number rapidly improves the Nusselt number due to the rise of fluid velocity with Re.

6.4.3 Performance factor

The performance factor vs elliptical fin height (EFH) with respect to Reynolds number is illustrated in Figure 6.10. The performance factor increases initially with an increase in Reynolds number and then declines with further increase in Reynolds number. This is because the rise in effective Nusselt number with Re more prominent than effective friction factor.

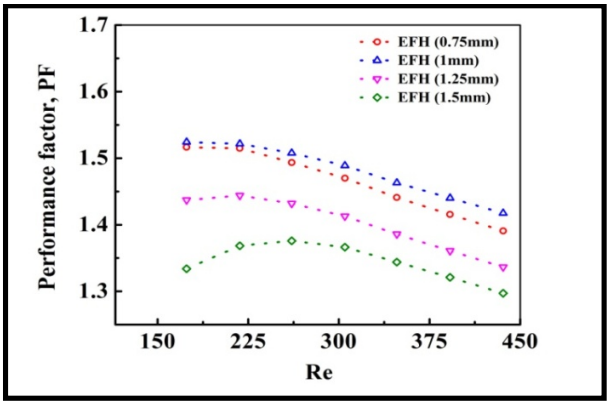

Figure 6.10 Effect of EFH on performance factor for various Re

Similarly, an increasing EFH enhances the performance factor up to EFH of 1 mm, and thereafter the performance factor declines rapidly. The effective friction factor shoots up with increasing EFH compared to effective Nusselt number. Therefore, the performance factor is reduced. At a Reynolds number of 174, the performance factors for EFH of 1.5 mm, 1.25 mm, 1 mm, and 0.75 mm are 1.33, 1.43, 1.52, and 1.51, respectively. The fin height of 1 mm exhibited the maximum performance factor out of all the analyzed fin heights.

6.5 Effect of fin centre to centre distance

From the above results, the best elliptical fin height (1 mm) microchannel model was selected. For the best EFH MC model, the centre distance was varied from 2.6 mm to 3.4 mm with an increment length of 0.2 mm. A total of five elliptical fin MC models were developed to study the effect of centre to centre distance on thermal performance and the same was compared with straight fin MC. Besides, other parameters like average wall temperature, Nusselt number and friction factor variation with Reynolds number were examined and discussed in detail.

6.5.1 Pressure drop characteristics

Figure 6.11 illustrates the effect of fin to fin centre distance, Re on pressure drop, and its comparison with SF microchannel. As fin to fin centre distance increases, secondary flow area between two successive fins increases and that accommodates fewer fins in a given channel length. The reduction of number of fins along the channel length reduces the pressure energy losses in a given channel. Therefore lower pressure drop is associated with larger fin to fin centre distances. In addition to this, pressure drop increases rapidly with increasing Reynolds number.

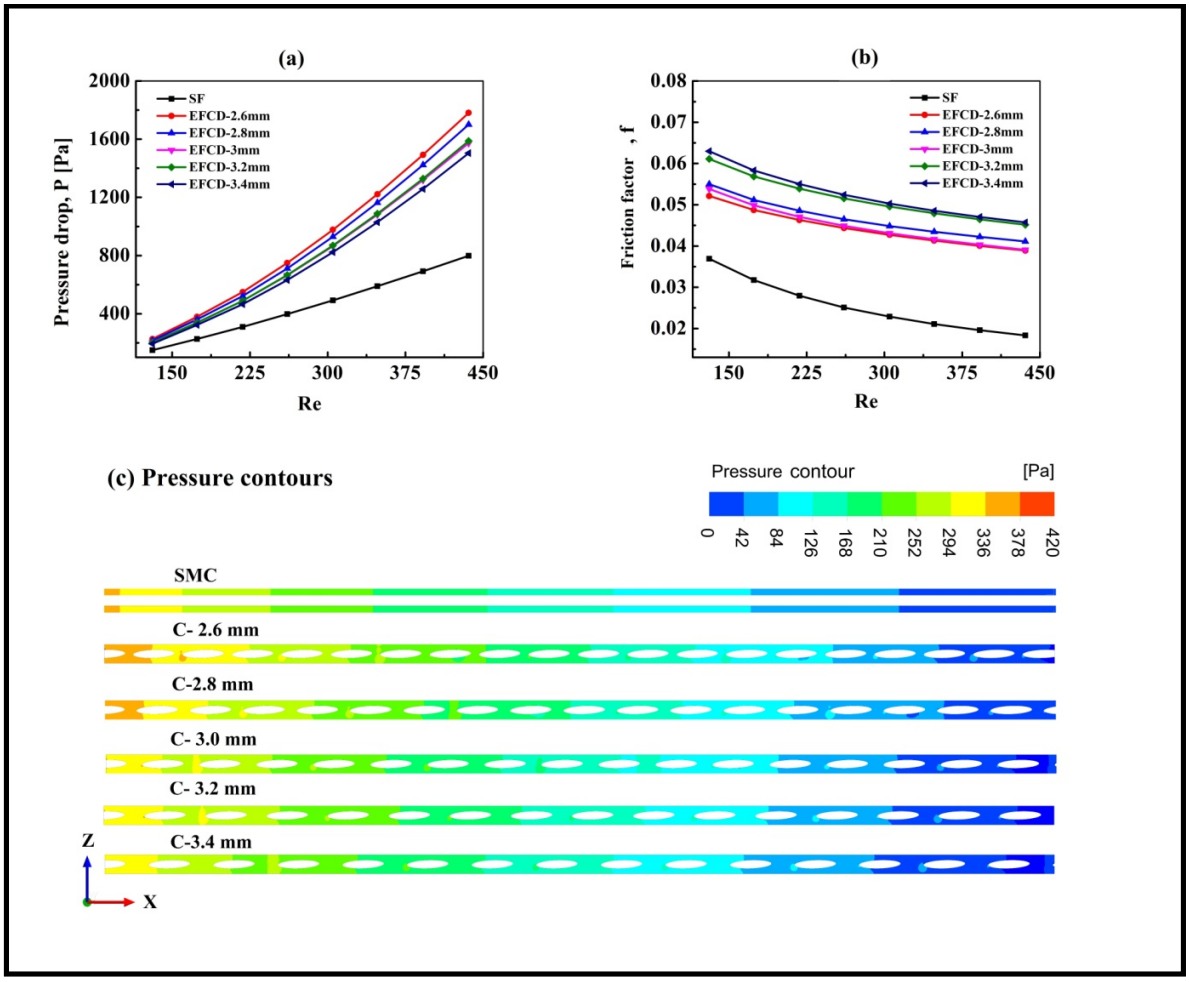

Figure 6.11(a) pressure variation along the channel length (b) effect of friction factor with Re (c) pressure contours of elliptical fin models and straight fin.

From the fanning friction factor equation (3.18), the friction factor is inversely proportional to the square of fluid velocity and channel length, directly proportional to the product of pressure drop and hydraulic diameter. In this, the velocity of fluid is one crucial parameter that affects friction factor. An increased centre distance between two successive fins gradually increases the friction factor as shown in Figures 6.11(a) and 6.11(c). This is due to reduction in the fluid velocity in the channel. Whereas, for all fin to fin centre distances, the rise in Re boosts the fluid velocity and results in decrease in the friction factor.

6.5.2 Thermal characteristics

The effect of fin to fin centre distances on wall temperature and Nu with Re, is depicted in Figure 6.12. The wall temperature of various elliptical fin models shows lower wall temperature compared to straight fin MC. This is the result of boundary layer re-initialization and thinning of boundary layer thickness. The wall temperature of elliptical fin MC is further minimized by reducing fin to fin centre distance. This reduction in fin to fin centre distance enhances heat convective area and fluid mixing; it reduces wall temperature of the channel. This is evident from the temperature contours drawn in X-Z plane along the channel length, as shown in Figures 6.12(a) & (c). The wall temperature reduction of elliptical fin centre distance (EFCD) of 3 mm over straight fin are 2.5 °C, 2.1 °C, 4.3 °C, 6.3 °C, 7.7 °C, 8.5 °C, 9.1 °C and 9.6 °C for Re of 131, 174, 218, 261, 305, 348, 392 and 436 respectively. The maximum and minimum wall temperature reduction of 19% and 0.7 % were observed when the centre distance between fins was EFCD-2.6 mm (at Re 436) and EFCD-3.4 mm (at Re 131) respectively.

The Nusselt number (Nu) of elliptical MC initially increases with increasing centre distance between the fins and then it decreases. This Nusselt number variation mainly depends on convective heat transfer area and fluid mixing within the channel. As the centre distance increases, fluid mixing becomes more effective than reduction in convective heat transfer area, resulting in higher Nusselt number, but further increase in centre distance (>3 mm) reduces both convective area and fluid mixing, and shows lower Nusselt number. (The fluid mixing is more rapid with fluid velocity and their contours are shown in Figure 6.13). The maximum Nusselt number (Nu) 26 is obtained at Re 436 for elliptical fin model whose fin to fin centre distance is 3 mm. The percentage of enhancement of Nusselt number for the above fin model over straight fin model was 159 %, 180 %, 194 %, 206 %, 215 %, 222 %, 228 % and 233 % for Re 131, 174, 218, 261, 305, 348, 392 and 436 respectively.

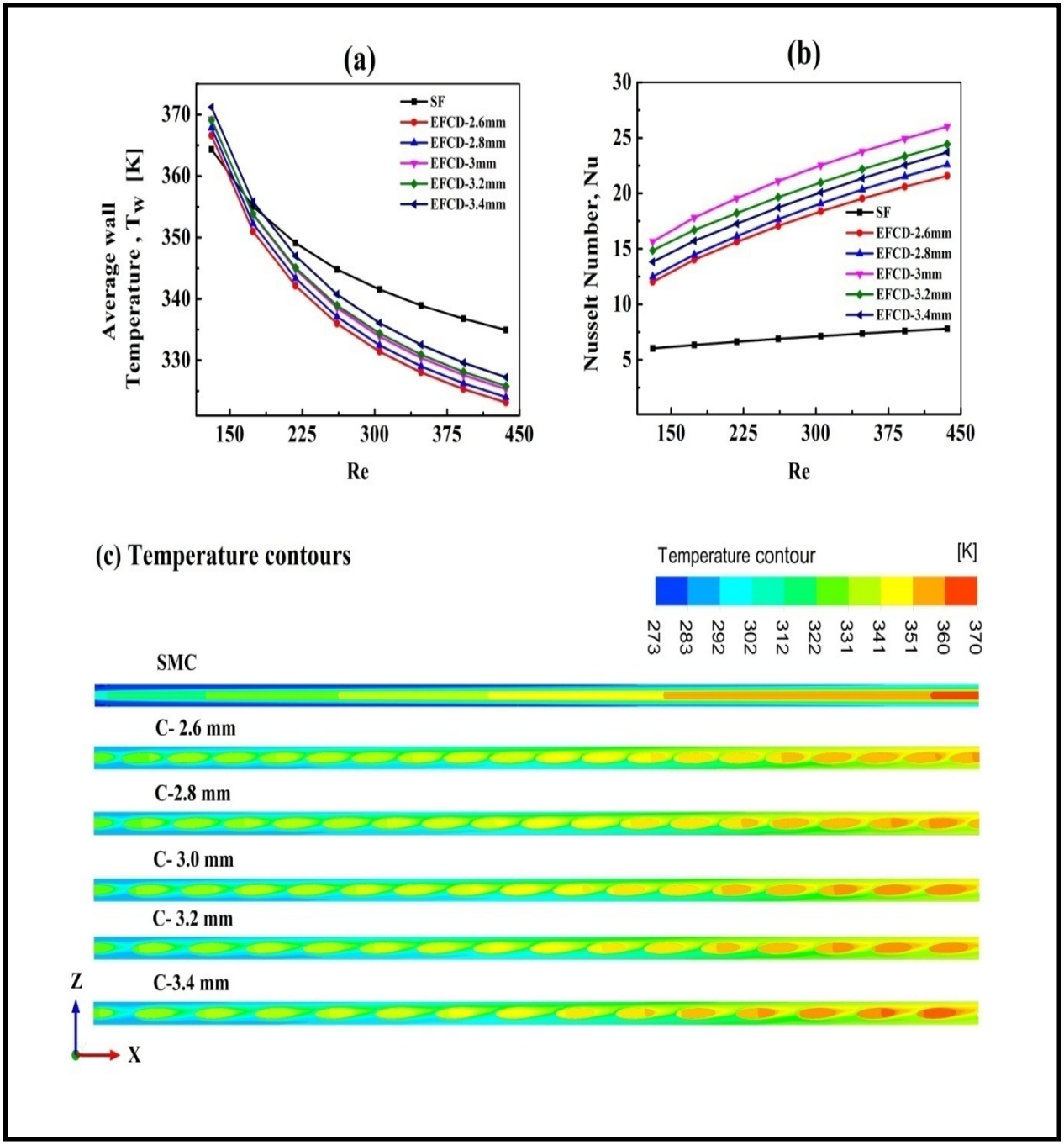

Figure 6.12 (a) effect of fin to fin centre distance on wall temperature for various Re (b) effect of fin to fin centre distance on Nusselt number for various Re (c) temperature contours of elliptical fin models and straight fin.

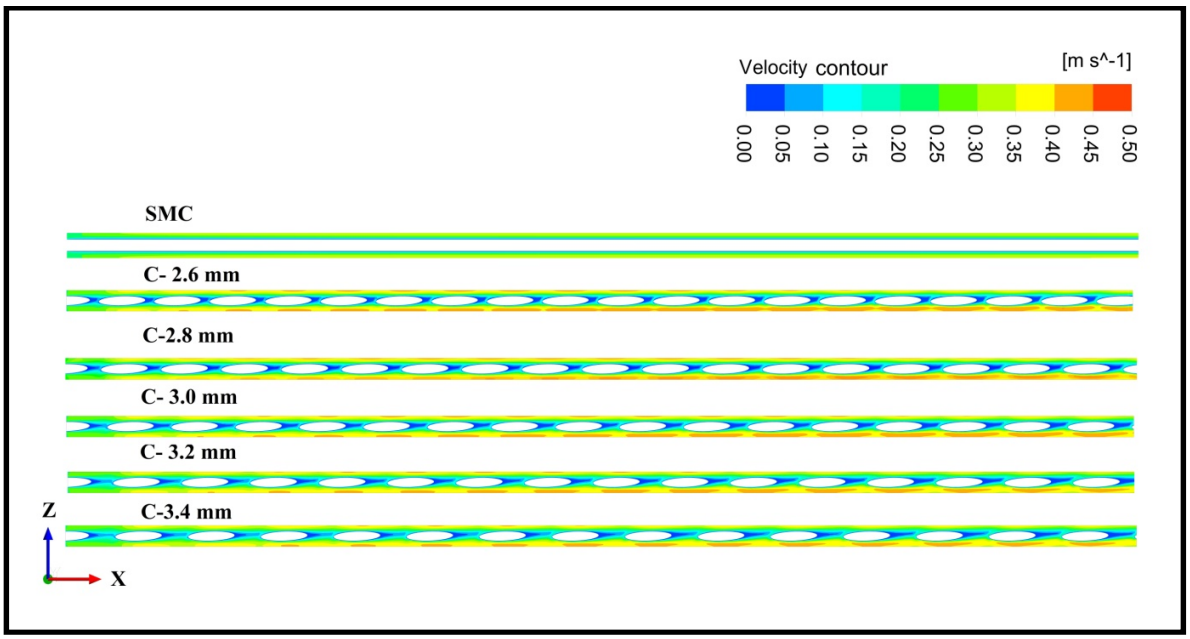

Figure 6.13 Velocity contours of elliptical fin models and straight fin.

6.5.3 Performance factor

Figure 6.14 shows the performance factor vs fin to fin centre distance with respect to Reynolds number. The performance factor increases initially with the rise of Reynolds number and then declines with a further increase in Re. This is because of the rise in effective Nusselt number when Re is more prominent than effective friction factor.

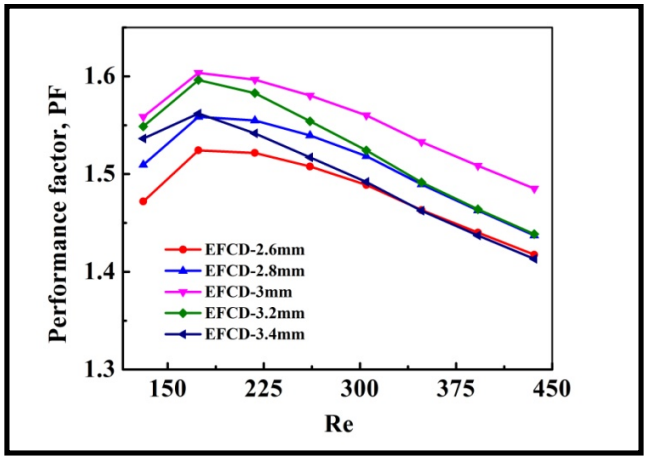

Figure 6.14 Effect of fin to fin centre distance on performance factor for various Re

Similarly, increasing centre distance enhances the performance factor up to a centre distance of 3mm, but thereafter the performance factor declines rapidly, as convective heat transfer area reduces with an increase of centre distance. In addition to this, the effectiveness of fluid mixing also reduces with an increase in centre distance. Therefore, the performance factor deteriorates. The maximum performance factors for various centre distances such as 2.6 mm, 2.8 mm, 3.0 mm, 3.2 mm and 3.4 mm are 1.52, 1.55, 1.61, 1.59, and 1.56 at Re 174 respectively.

6.6 Conclusions

Parametric analyses of elliptical fin microchannel were carried out by varying ellipticity ratio, fin orientation, channel depth and fin to fin centre distance. In order to illustrate the effectiveness of different parameters on hydrothermal performance, the same was compared with straight fin MC. Other parameters like average wall temperature, Nusselt number and friction factor variation with Reynolds number etc., were examined and discussed in detail.

- Performance factor augments initially with an increase in ER (up to ER-0.20) and then it reduces with further increase in ER > 0.20. For all Re, Maximum performance factor was observed for ER-0.20 model, when compared to other ER models (ER-0.15, ER-0.75, ER-0.20, ER-0.225, and ER-0.25).The performance factor of ER-0.20 model at various Reynolds numbers of Re-174, Re-218, Re-261, Re-305, Re-348, Re-392 and Re-436 was 1.163, 1.184, 1.205, 1.238, 1.250, 1.269, and 1.285 respectively.

- The increase in ER also reduces average wall temperature due to intensified fluid mixing in the channel. The temperature reduction for elliptical fin models ER-0.15, ER-0.175, ER-0.20, ER-0.225 and ER-0.25 over straight fin MC was 1.58 %, 5.28 %, 7.17 %, 8.38 % and 9 % respectively.

- For Re of 218 and heat flux of 65 W/cm^2, performance factor of optimized ER model (ER-0.20) enhances initially at a fin orientation angle ($\leq 2°$) and it declines with increase of fin orientation angle. The highest performance factor of 1.37 was noted, when the fin was oriented at 2° to the flow stream. Besides, the average wall temperature reduction for

10º, 8º, 6º, 4º, 2º and 0º EFMC over straight MC was 26.11 %, 27.45 %, 27.55 %, 26.95 %, 21.45 % and 2.96 % respectively.

- An optimum angled Elliptical fin model was then examined by altering fin heights (EFH-1.5 mm, EFH-1.25 mm, EFH-1 mm, and EFH-0.75 mm) to augment heat transfer rate. It revealed that performance factor enhances initially with fin height and then it reduces with further increase in fin height. Among all microchannel models, the 1 mm height elliptical fin microchannel model showed highest performance factor of 1.52 at Re of 174. But their performance drastically trimmed down with increasing Reynolds number. The percentage of wall temperature reduction for different elliptical fin height models (EFH-1.5 mm, EFH-1.25 mm, EFH-1 mm and EFH-0.75 mm) over straight MC at Re 174 was 23.6 %, 17.2 %, 6.5 % and -9.8 % respectively.

- Finally, an optimum fin to fin centre distance was evaluated for optimized fin height model for enhanced heat transfer characteristics. The maximum Performance factor 1.61 was observed at Re -174, when the fin to fin distance was 3 mm. The wall temperature reduction corresponding to this maximum performance factor was 2.57 % over straight microchannel. For Re 436, the percentage of wall temperature reduction for various fin to fin centre distances was 19 %, 17.6 %, 15.52 %, 14.69 % and 12.4 % for EFCD-2.6, EFCD-2.8, EFCD-3.0, EFCD-3.2, and EFCD-3.4 respectively. The maximum and minimum wall temperature reduction 19 %, 0.93 % was observed when the centre distance between fins was EFCD-2.6 mm (at Re 436) and EFCD-3.4 mm (at Re 131).

CHAPTER 7

Numerical study of nanofluids on optimized elliptical fin microchannel heat sink

This chapter investigates the impact of nanofluids on the thermal performance of an optimized elliptical fin microchannel heat sink operating under steady state laminar flow conditions. The study focuses on two different heat sink materials, namely steel and copper, and examines various parameters including the type of nanofluid used (CuO-water and Al_2O_3-water) and particle concentration (ranging from 0.15 % to 1 %). Numerical analysis was conducted within the range of Re 100-768 and at a heat flux of 65 W/cm^2. The study compared the performance of nanofluids with that of water, and investigated other parameters such as average wall temperature, Nusselt number, friction factor, and performance factor variation with Reynolds number and volume fraction of nanofluid. The findings are discussed in detail.

7.1 Effect of heat sink material on Nu and thermal resistance

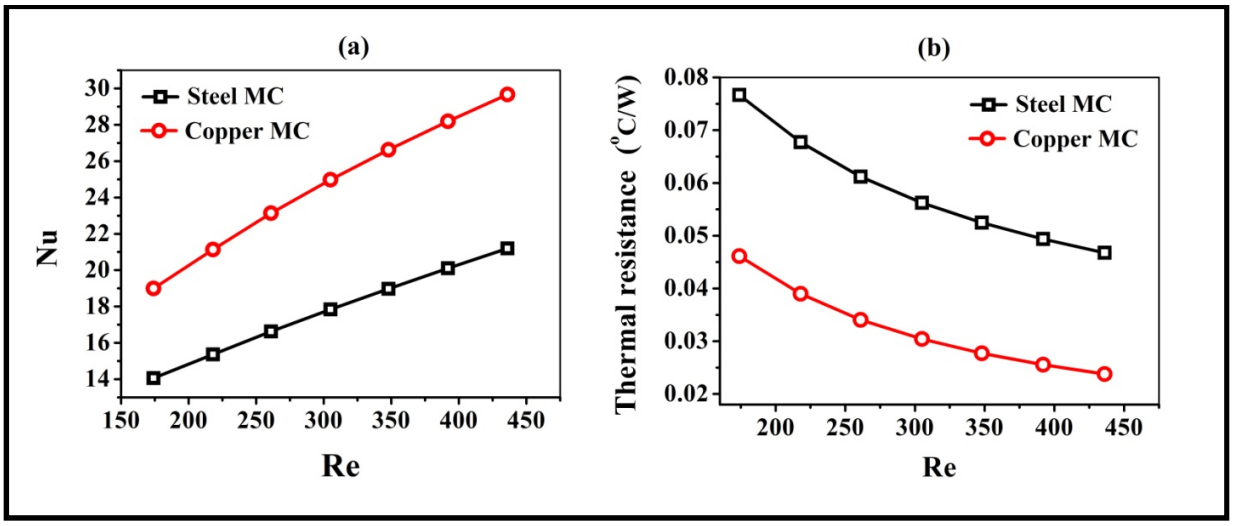

Figure 7.1 Effect of heat sink material on (a) Nu (b) thermal resistance

Figure 7.1(a) & (b) illustrates the effect of heat sink material on Nusselt number and thermal resistance for various Re. The copper microchannel heat sink has more ability to

transfer higher heat fluxes due to larger thermal conductivity compared to steel. Therefore, copper heat sinks shows higher Nusselt number compared to steel. For both heat sinks, an increase in Re linearly increases their Nusselt number due to reduction in thermal resistance as shown in Figure 7.1(b).

7.2 Effect of two different nanofluids on friction factor and Nu

Figure 7.2(a) shows that the effect of various nanofluids (CuO-Water and Al_2O_3-Water nanofluid) on friction factor and Nu for various Reynolds number when compared to pure water. The volume concentration of CuO-Water and Al_2O_3-Water nanofluids of 0.5 % and particle diameter of 40 nm was considered in this analysis. As seen in Figure 7.2(a), friction factor reduces with an increase in Re and this behaviour is analogous to that of water in SFMC and EFMC. Since friction factor varies inversely with the square of fluid velocity, as shown in equation 3.18. The use of nanofluids in microchannel marginally raises friction factor. As the nanoparticles are so small, nanofluids with low concentrations do not cause significant pressure penalty, as evident from Figure 7.2(a). The minimum increase in friction factor was seen for CuO-Water nanofluid over water and Al_2O_3-Water nanofluid.

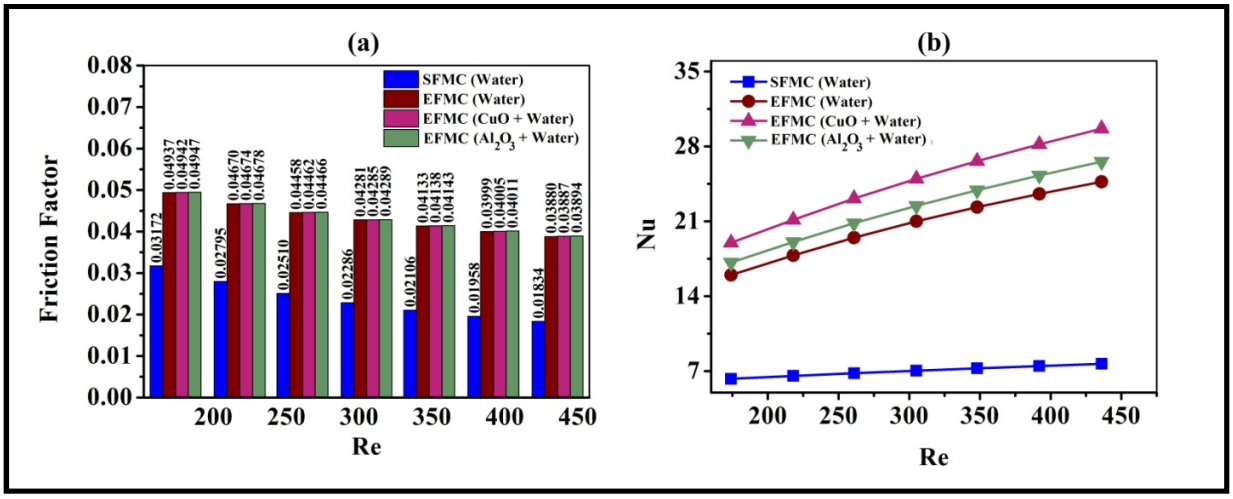

Figure 7.2 Effect of nanofluids on (a) friction factor (b) Nu.

In Figure 7.2(b), the Nusselt numbers for various types of nanofluids that flow through

EFMC are presented for different Re. It is evident from Figure 7.2(b) that an increase in Re improves Nusselt number of all nanofluids, which is similar to that of water. This is mainly due to an increase in the velocity of the fluid that is flowing through the channel. As a consequence of this, heat carrying capacity of fluid was enhanced. In addition to this, CuO-Water nanofluids show the largest heat transfer capacity when compared to aluminium oxide nanofluid. This is because CuO-Water nanofluids have higher conductivity. It is also evident from Figure 7.2(b) that the utilization of high conductivity fluids in the MC resulted in a reduction of the maximum wall temperature.

The impact of different types of nanofluids on wall temperature and thermal resistance for various Re in EFMC are shown in Figure 7.3. It is evident from Figure 7.3(b) that an increase in Re reduces the thermal resistance of all nanofluids, which was similar to that of water. An accelerated fluid carries a large quantity of heat fluxes from the heat sink by reducing the thermal boundary layer thickness. Furthermore, addition of nanoparticles to base fluid reduces thermal resistance. This reduction can be achieved more quickly with CuO-Water nanofluids than with Al_2O_3-Water nanofluids due to better thermal characteristics. As a result, maximum reduction in wall temperature of heat sink as depicted in Figure 7.3(a), when compared to Al_2O_3-Water nanofluid and water alone. Hence, higher conductivity in nanofluids such as CuO-Water nanofluid yields better thermal performance.

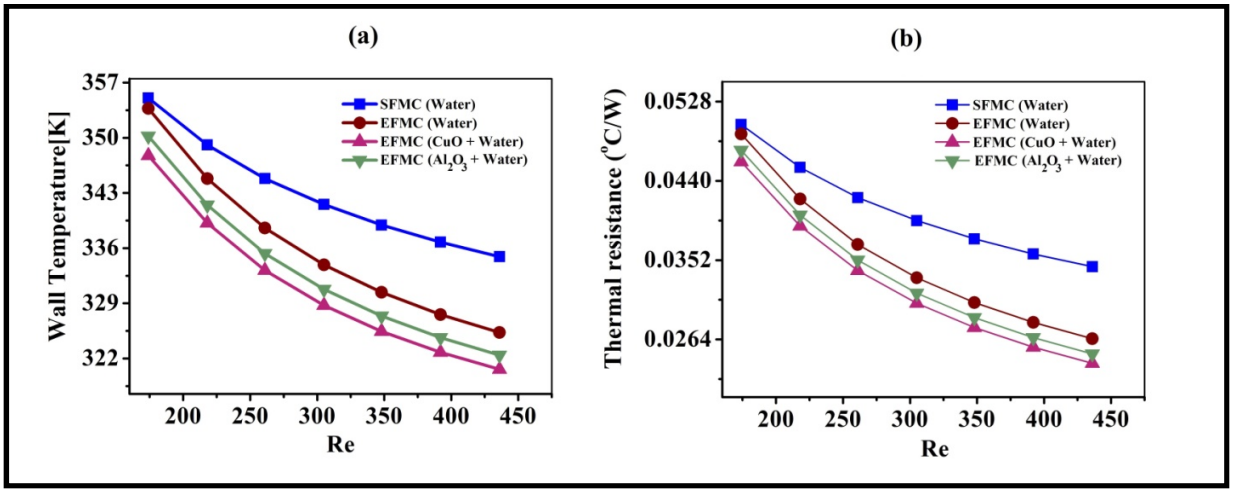

Figure 7.3 Effect of nanofluids in EFMC and SFMC on (a) thermal resistance (b) PF.

7.3 Effect of volume fraction and Re on flow characteristics

The pressure drop for pure water and CuO-water nanofluid at different nano particle concentrations is demonstrated in Figure 7.4. It indicates that with the enhancement of nano particle concentration the pressure drop increases across the micro channel as seen in pressure contours 7.4(c). The pressure drop is maximum and minimum for 1 % and 0.125 %

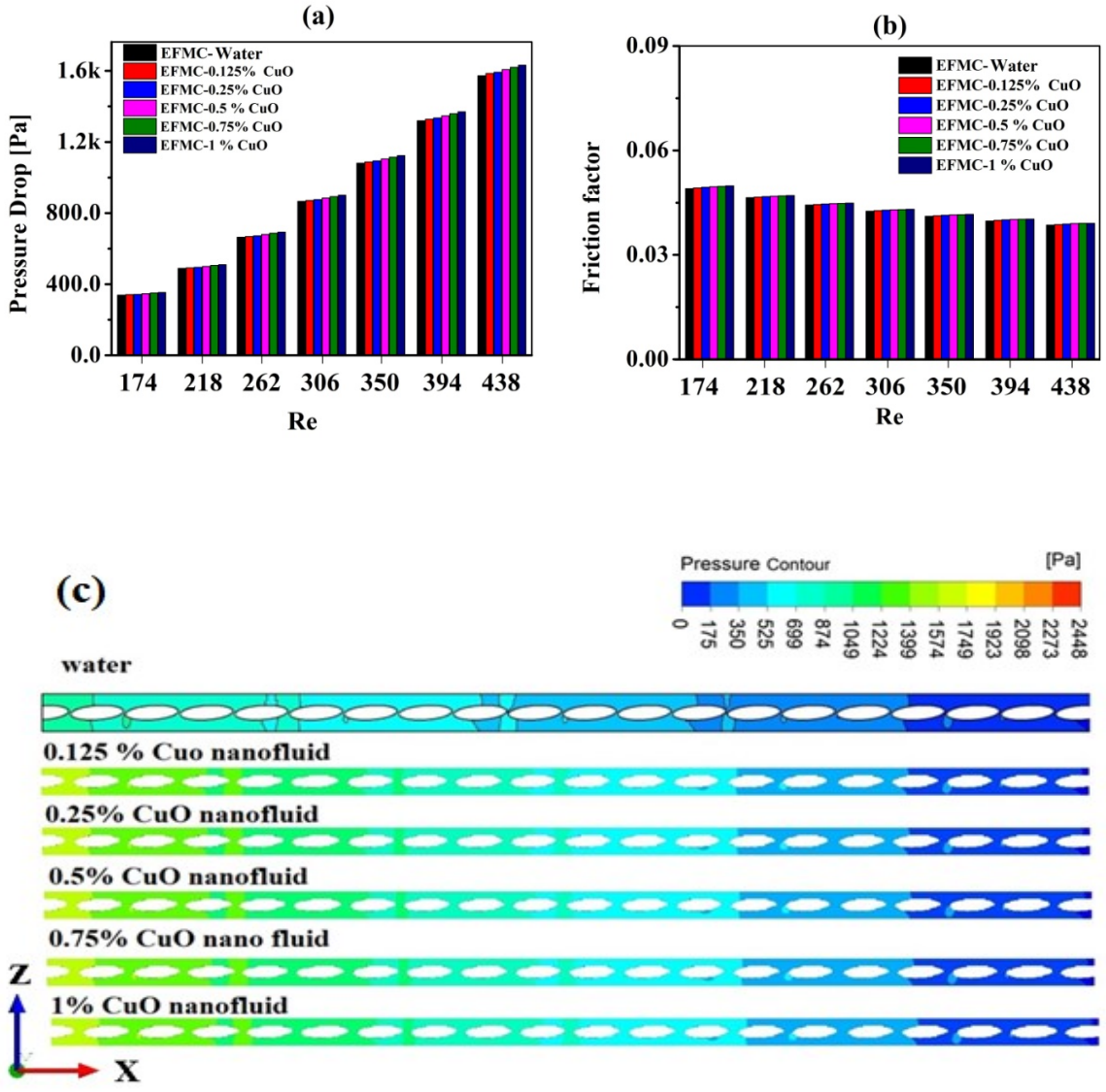

Figure 7.4 Effect of pure water and CuO-water nanofluid concentrations in EFMC on (a) pressure drop (b) friction factor (c) temperature contours.

volume concentration of CuO nanoparticles respectively. It can be further inferred that with increasing Reynolds number, the pressure drop increases due to increase in the velocity of nanofluid. The maximum rise in pressure drop has been recorded as 4.4 % for Re 174 at 1 % volume concentration of CuO nanoparticles over water. Thus, in EFMC the percentage rise in pressure drop for CuO-water nanofluid and pure water are almost same for each Reynolds number. Therefore, CuO-water nanofluids have been proven to be a good cooling fluid, even though pressure drop in EFMC rises with volume fraction of CuO-water nanofluid.

Figure 7.4(b) depicts the effect of friction factor with volume fraction of nanofluid and Re. The friction factor for fluids can be determined using fanning equation 3.18. Friction factor is directly proportional to pressure drop but inversely proportional to the square of the velocity of the flowing fluid due to which the latter has a more predominating effect on the friction factor than pressure drop. With an increase in velocity, the friction factor significantly decreases. Figure 7.4 show that friction factor is maximum for 1% volume concentration of CuO nano particles and minimum for pure water. It can also be observed that friction factor decreases with an increase in Reynolds number. The friction factor has been recorded to be maximum at Re of 174 and minimum at Re of 438. As such, it can be concluded that although CuO nano particles enhance the friction factor along the length of EFMC, the enhancement is negligible when compared to water for the same Reynolds number.

7.4 Effect of volume fraction and Re on heat transfer characteristics

Figure 7.5(a) depicts the impact of CuO particle concentration on wall temperature of the microchannel. For a constant Re 174, an increase in particle concentration of CuO significantly reduces the wall temperature of heat sink. A reduction in wall temperature of 2.2 % to 12 % was observed with an increase in nanoparticle concentration of 0.125 % to 1 %. It is also noted that an increase in Re from 174-438 further reduces the wall temperature by 2 %.

Figure 7.5(b) depicts that with an increase in the particle concentration of CuO from 0.125 % to 1 % there is a significant enhancement in Nusselt number. For a constant Re of 174, Nu is marked to be maximum (22.4) for a volume concentration of 1 % and minimum for pure water (16). Moreover, it can also be inferred that with an increase in Reynolds

number, increases Nusselt number. This happens because the convective heat transfer coefficient increases with an increase in the velocity of the flowing fluid. For a given 1 % CuO-water nanofluid, Nu further increased by increasing Reynolds number from 174 to 438. The maximum Nu of 35 is achieved with 1 % CuO-Water nanofluid at Re 438, which is 42 % higher than pure water in EFMC. Therefore, it can be concluded that nanofluid is undoubtedly superior to water for enhancing heat transfer in EFMC.

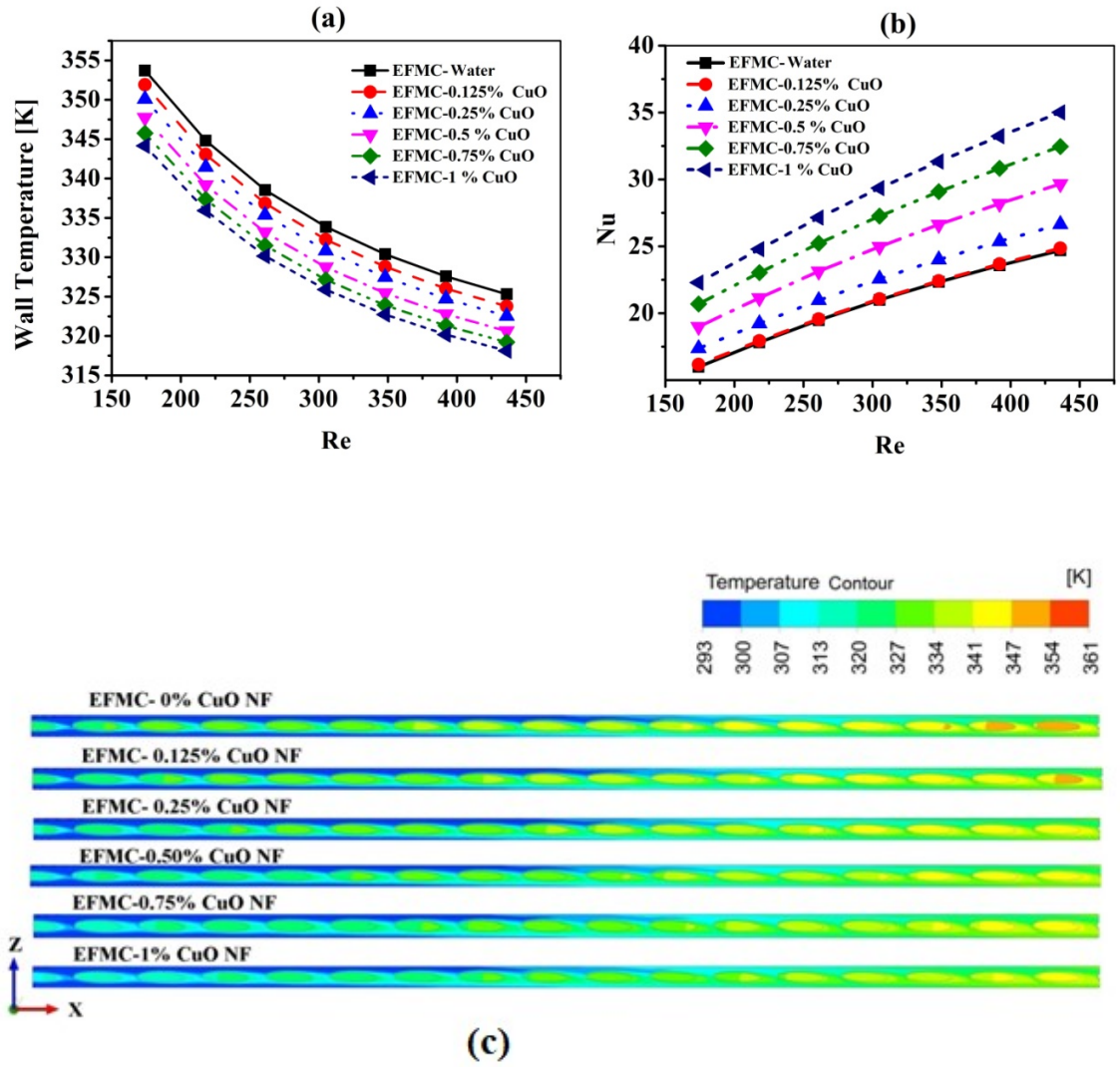

Figure 7.5 Effect of pure water and CuO-water nanofluid concentrations on (a) wall temperature (b) Nu in EFMC at different Re (c) temperature contours

Fig 7.6(a) shows that with an increase in nanoparticle concentration of CuO, the pumping power increases due to an increase in the density of the nanofluid. The pumping power is maximum for 1 % volume concentration and minimum for pure water. However, there was no significant difference in pumping power. It is noticeable that pumping power rises by a significant amount with an increase in the Re. The pumping power required is higher for achieving higher velocity of the flowing fluid. The maximum rise in pumping power of 4.4 % was observed for 1 % CuO-water nanofluid at Re 438.

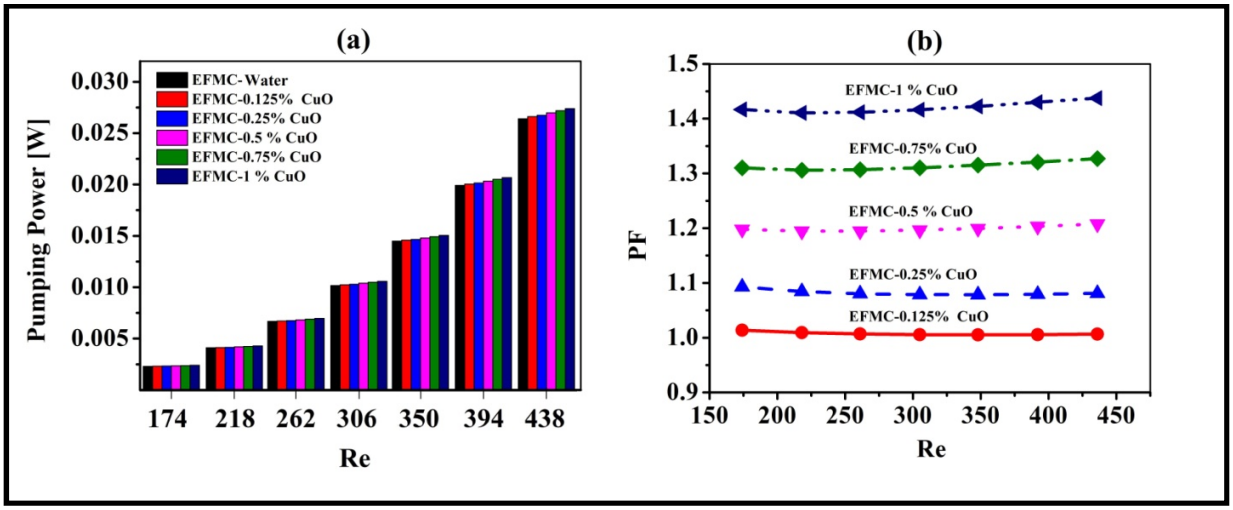

Figure 7.6 Effect of pure water and CuO-water nanofluid concentrations on (a) pumping power (b) PF in EFMC at different Re.

Figure 7.6(b) shows the variation of PF for various volume fractions of CuO nanofluid and Re. The PF increases with arise in nanoparticle concentration in base fluid. This is because the rise in effective Nu is more prominent than a rise in effective friction factor. It is also seen in Figure 7.6(b) that higher volume fraction of CuO nanofluid shows higher PF. At higher concentrations, the thermal conductivity of nanofluid increases, which in turn leads to an increase in convective heat transfer capacity of nanofluids. The maximum performance factor enhancement of 43 % was noted at Re 438 for 1 % CuO-Water nanofluid. It is also clear from Figure 7.6(b) that an increase in Re does not have a significant impact on PF.

The thermal resistance can be determined using equation 3.20. Figure 7.7 highlights that thermal resistance ratio is inversely proportional to nanoparticle concentration and Re.

With an increase in CuO nanoparticle concentration from 0.125 % to 1 %, there is a noticeable decrease in the thermal resistance ratio. This happens because the maximum wall temperature of EFMC decreases with increasing CuO nanoparticle concentration. It is also observed that the thermal resistance of the nanofluid further decreases with an increase in Re. For higher Reynolds number, the reduction in thermal resistance ratio is more rapid due to increased Brownian motion of particle with velocity and as a consequence, thermal transport increases as well. The highest reduction in thermal resistance of 17 % was noted for 1 % volume concentration of CuO-water nanofluid at Re of 438.

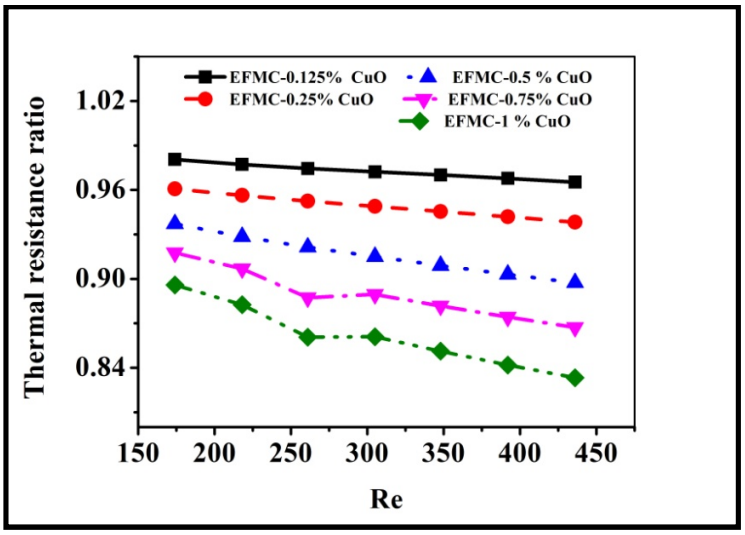

Figure 7.7 Effect of pure water and CuO-water nanofluid concentrations on thermal resistance ratio in EFMC.

7.5 Conclusions

In this study the effect of flow and heat transfer characteristics of optimized EFMC heat sink on heat sink material (steel and copper), types of nanofluid (CuO-Water and Al_2O_3-Water) and particle concentration (0.15 %, 0.25 %, 0.5 %, 0.75 %, 1 %)was examined by volume of fluid method using commercial software ANSYS fluent. In addition, other parameters such as average wall temperature, Nusselt number, friction factor and performance factor variation with Reynolds number and particle concentration were evaluated. Based on the results, the following conclusion can be made:

- The copper heat sink has faster heat transfer rate than steel due to higher conductivity. As a result, lower thermal resistance noted in the heat sink through dissipating of a significant amount of heat flux to working fluid. For both heat sinks, a rise in Re increases the heat transfer rate.

- In comparison to CuO-water, Al_2O_3-water and pure water, the copper oxide water nanofluids were more prominent to transport higher heat fluxes. Adding highly conductive nanoparticles to fluid improves its convective heat transfer more quickly by reducing resistance in the heat flow path.

- Increase of nanoparticle concentration to base fluid increases pressure drop in microchannel. But the rise in pressure drop by increasing the volume concentration of CuO-Water nanofluid from 0.125 % to 1 % can be up to 4.4 %. Though the increase is very small, the maximum reduction in wall temperature was found to be 14 % (7.2 ^{o}C) when compared to conventional fluid at Re of 438. Moreover, for the same Re and 1 % CuO-Water nanofluid, the maximum enhancement in Nu by 42 % and reduction thermal resistance by 17 %.

- Finally, PF improves with particle concentration due to improved effective Nu compared to effective friction factor. The maximum Performance factor 1.41 was observed for 1 % CuO-Water nanofluid over conventional fluid. On the other hand, a little rise in PF was observed with increasing Re.

CHAPTER 8

Experimental study of nanofluids on optimized elliptical fin microchannel heat sink

This chapter focuses on the impact of CuO-water nanofluids on the thermal performance of an optimized elliptical fin microchannel heat sink under steady-state laminar flow conditions. The study used 17-4PH, a precipitation-hardening martensitic stainless steel, as the heat sink material. The experimental investigation involved varying concentrations of CuO-water nanofluid (0.15 %, 0.25 %, 0.5 %, 0.75 %, and 1 %) and comparing their thermal performance with that of water at a heat flux of 65 W/cm^2 and a Reynolds number range of 100-768. In addition, various parameters, including average wall temperature, Nusselt number, friction factor, and performance factor variation with Reynolds number and volume fraction of nanofluid, were analyzed and discussed in detail.

8.1 Experimental setup

8.1.1 Microchannel test rig

A schematic representation of the experimental layout is shown in Figure 8.1. It consists of a 5 litre capacity holding tank from which deionised water flows into the loop by means of pump. Bypass line is provided to control the flow rate which is recorded by a flow meter. Pressure gauge and differential pressure transducer were connected at the inlet and across the test section respectively to record the pressure. Liquid-to-air heat exchanger was provided to dissipate the heat from loop fluid. Type-T thermocouples were also located at the inlet and outlet of the test section to measure the fluid temperatures at these locations. Apart from that five thermocouples were placed from inlet to outlet an equal distance of 12.5 mm to capture microchannel wall temperatures. All thermocouples were read into a data acquisition system.

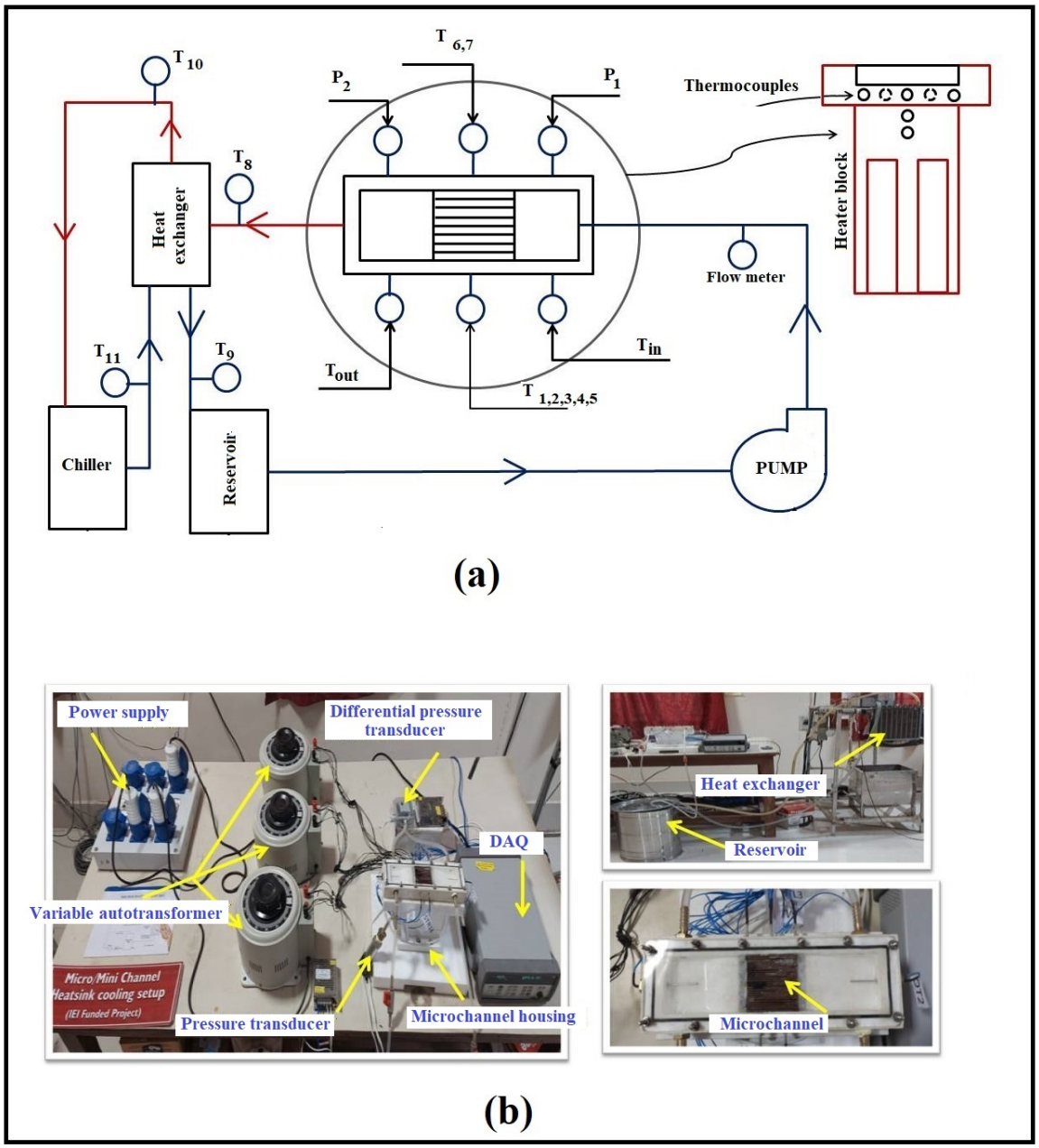

Figure 8.1 Experimental setup of microchannel heat sink (a) line diagram (b) actual experimental setup

8.1.2 Test Section

In the test rig, the main point of focus is test section. The test section consists of a base plate (bottom housing), heater housing and test section (Top housing). All housing is made of White Teflon because of its high strength and insulating properties. Bottom housing is fastened to flat surface to support the entire test section. Middle housing consists of copper block which is used for heat generation. In the test rig, microchannel base area is 50 mm × 50 mm. In general this base area replicates solar cells. The maximum heat generated from solar cells is up to 200 W/cm^2. Hence twelve cartridge heaters of 500 W each were fixed into the copper block. The voltage input to the cartridge heaters was controlled by a DC power supply unit. Microchannel heat sink is placed into top housing consists of inlet/outlet manifolds. Figure 8.2 shows an exploded view of the test section.

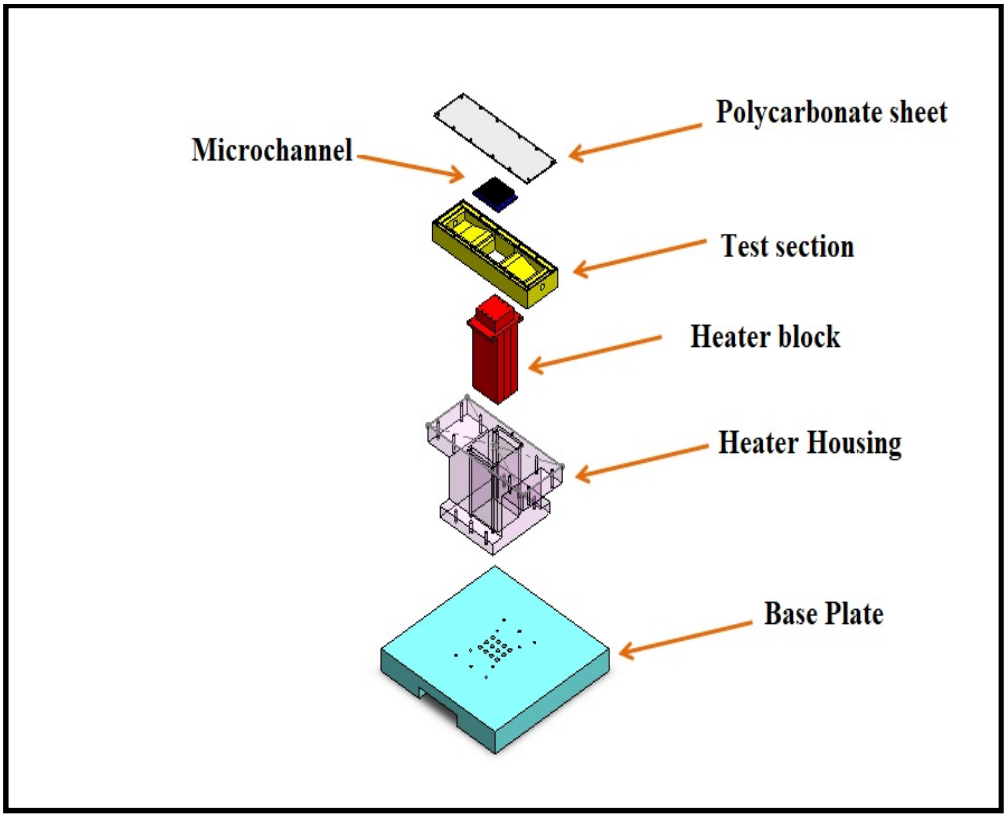

Figure 8.2 Exploded view of test section

8.1.3 Microchannel fabrication

The heat sink was fabricated using 3D metal printing machine called DMFLEX-100 as shown in Figure 8.3. This can print intricate parts with a minimum wall thickness of 150µm without compromising accuracy. Hence it was used for fabrication of complex microchannel and the specifications of 3D metal printer are provided in Table 8.1. In the present study, optimal elliptical fin microchannel of foot print area 50 mm × 50 mm × 5 mm was fabricated using stainless steel 17-4PH. A total of 24 microchannels was printed on base (4 mm) with a height of 1mm as per geometrical file provided to 3D metal printer. The geometrical dimensions of microchannel are shown in Table 8.2.

Figure 8.3 Schematic diagram of 3D metal printer

Table 8.1 3D metal printer specifications

Make	3D systems
Model	DMPFLEX-100
Software	3D-XPERT
Metal alloys	CoCr, AlSi7Mg, Ti6Al4V, 17-14Ph
Build volume	100 mm × 100 mm × 80 mm
Minimum wall thickness	150 µm
Layer thickness	10 µm -100 µm
Minimum size	X=100 µm, Y=100 µm, Z=20 µm
Accuracy	0.1 % - 0.2 %

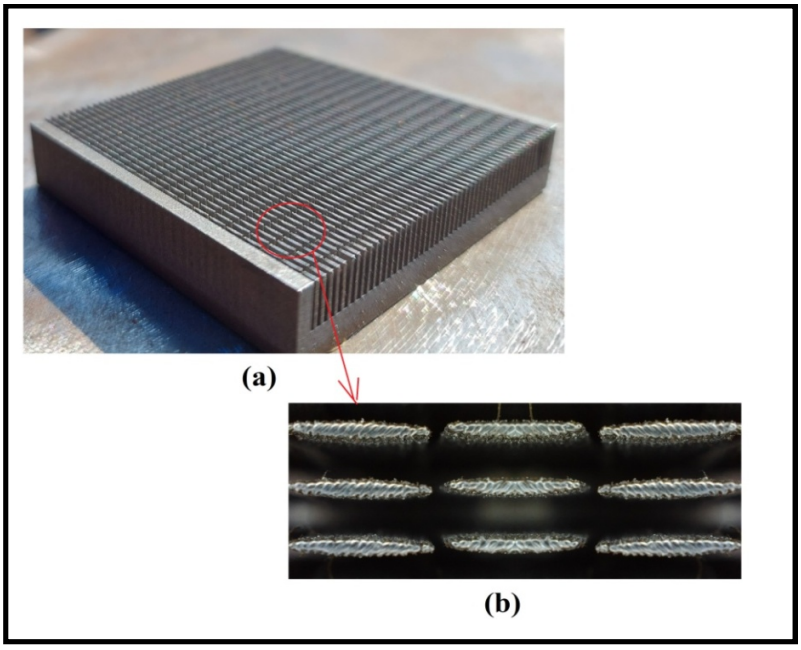

Figure 8.4 The 3D printed microchannel heat sinks (a) 3D view (b) enlarged view

Table 8.2 The geometrical dimensions of microchannel heat sink

S.NO	**Characteristic**	**Elliptical fin microchannel**
1	Material	17-4PH
2	Foot print Area ,(W × H)	50 mm × 50 mm
3	Channel Width, W_{ch}	562 (µm)
4	Length of channel, L	50 (mm)
5	Channel height, H_{ch}	1000 (µm)
6	Number of fins row, n	49
7	Number of fins per row	20
8	Fin width , W_f	438 (µm)
9	Fin centre distance, S	3000 (µm)
10	Semi-Major axis, l_f	1090 (µm)
11	Semi-Minor axis, b_f	219 (µm)
12	orientation angle, θ	2 (deg)

8.1.4 Nanofluid preparation

Two step techniques is the most common approach for preparing nanofluids. In this technique, the prepared nanopowders were dispersed in base liquid using ultrasonic sonicator as shown in Figure 8.5 to reduce agglomeration of nanoparticles. In addition to this, a surfactant known as CTAB is employed with the aim of reducing the surface tension of the nanofluid in order to improve its stability.

Figure 8.5 Ultrasonic sonicator

The specifications of nanoparticles provided by a reputed manufacturer are summarized in Table 8.3.

Table 8.3 Specifications of the nanoparticles

Manufacturer	**SISCO Research laboratory Pvt Ltd**
Particle size (nm)	40
Particle thermal conductivity(W/m. K)	69
Particle density (kg/m^3)	6300
specific surface area (SSA) (m^2/g)	80
Molar mass (J/K mole)	79.5

The mass of the nanoparticles required for a particular particle concentration is estimated by using eq.8.1.

$$\Phi = \frac{\left(m/\rho\right)_{np}}{\left(m/\rho\right)_{np}+\left(m/\rho\right)_{bf}} \tag{8.1}$$

To weigh the nanoparticles, a digital electronic balance (Figure 8.6(a)) was employed. Initially, the surfactant (CTAB, 10 % by weight of nanoparticles) was added to distilled water, which was then sonicated for 30 minutes with an ultra sonicator (Figure 8.5). The addition of surfactant to the base fluid improves the stability and distribution of nanoparticles in base fluid. Then, the weighted CuO nanoparticles were mixed to the base fluid, and sonicated for 5 hours with 10 minutes of sonication and 2 minutes of idle time. Finally, the well dispersed, stable nanofluid was obtained as shown in Figure 8.6(d).The CuO/ Water nanofluids with volume concentration range of 0.15 % - 1 % were prepared to estimate the heat transfer characteristics of optimal elliptical fin microchannel heat sinks.

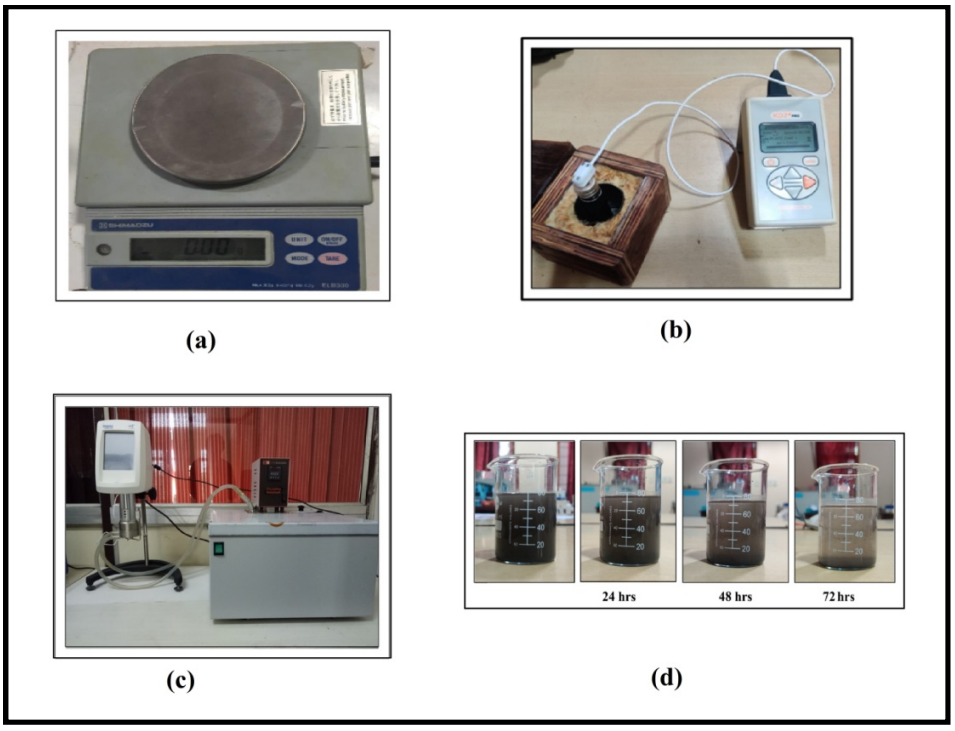

Figure 8.6 Various equipments used for measuring properties (a) digital weighing machine (b) thermal conductivity analyzer (KD2 PRO) (c) Brookfield DV2T viscometer (d) nanofluid at different time periods

8.2 Estimation of thermo-physical properties of nanofluids

To access the effect of nanofluids in microchannel heat sink, thermo-physical properties of nanofluids such as thermal conductivity, specific heat and density are required. These parameters are helpful in determining heat sink thermal performance. The evaluation of thermo-physical properties is presented in the following section.

8.2.1 Density and specific heat of nanofluid (Theoretical)

In this study, the base fluid contains very low concentration of nanoparticles. The density and specific heat of these nanofluids vary with particle concentration and can be determined theoretically using equation 4.2. and 4.3 [88], [89].

The density of nanofluids is defined as: $\rho_{nf} = \emptyset\rho_{np} + (1 - \emptyset)\rho_{bf}$

The specific heat of nanofluid is evaluated using following equation:

$$\left(\rho.C_p\right)_{nf} = \emptyset\left(\rho.C_p\right)_{np} + (1 - \emptyset)\left(\rho.C_p\right)_{bf}$$

8.2.2 Thermal conductivity (Experimental)

Thermal conductivity of all the concentrations of nanofluids (0.15 % -1 %)used in the present work was measured experimentally using thermal conductivity analyzer (**KD2 PRO**, **Decagon Devices, Inc., USA**), as illustrated in Figure 8.6(b). The instrument is equipped with different types of sensors with a software module interface to measure the thermal conductivity and specific heat of different materials like solid materials, powders, thin films, and wide range of liquids including nanofluids. This instrument also measures thermal diffusivity and volumetric specific heat of rock and concrete. The apparatus works based on transient line source principle and follows ASTM, IEEE, SSSA standards. In the current work, KS-1 sensor of 1.27 mm diameter and 6 cm long needle sensor was used to measure thermal conductivity of nanofluids with a maximum error of about 5 %.The equipment was facilitated by cylindrical testing chamber of diameter of 30 mm and length of 100 mm. After filling nanofluid in the testing chamber, a KS-1 needle sensor was immersed vertically. The needle was approximated as line heat source supplied for 30 sec and kept idle for 30 sec to attain thermal equilibrium state and then thermal conductivity was measured from the software interface module. This sensor can measure thermal

conductivity over a wide range of temperatures, from -50 °C to 150 °C. Each sample was tested three times under identical temperature conditions and the average of the experimental results was considered for further analysis. The experimentally measured thermal conductivity and correlations are shown in Figures 8.7 (a) & (b).

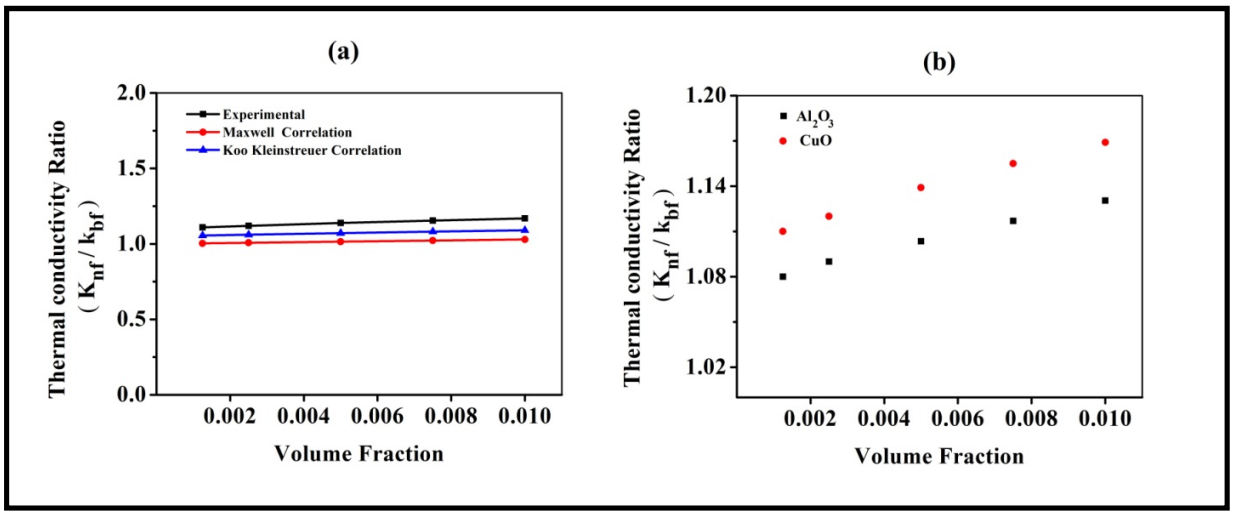

Figure 8.7(a) comparison of thermal conductivity with correlations (b) comparison of thermal conductivity of CuO-water nanofluid and Al_2O_3–water nanofluid

8.2.3 Viscosity of nanofluid (Experimental)

Viscosity of all the concentrations of nanofluids (0.15 % -1 %) used in the present work were measured experimentally using Viscometer (Brookfield DV2T, USA), as illustrated in Figure 8.6(c). In order to measure the Viscosity of the samples, a cylindrical container with a diameter of 82.5 mm was used. After loading nanofluids into the cylindrical container, the standard spindle was vertically inserted into the center of nanofluids. Viscosity is measured by rotating a spindle attached to the viscometer in the liquid sample until a constant reading is obtained. Similarly, the viscosity of CuO-water nanofluid was measured at various volume fractions. The experimentally measured results and correlations were compared and presented in Figure 8.8.

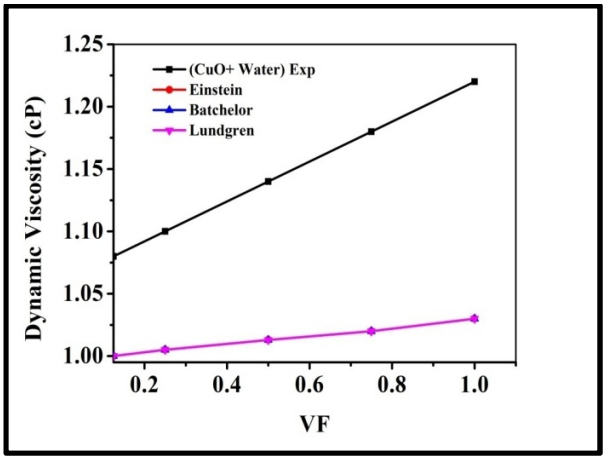

Figure 8.8 Dynamic viscosity variations with volume fraction

8.3 Data reduction

8.3.1 Heat transfer

To validate the integrity of the experimental setup, the effective heat absorbed by the fluid was evaluated by considering heat loss to environment. This heat loss to surrounding environment through conduction, convection and radiation was determined using an approach adopted in experimental investigation of Anbumeenakshi et al. [90]

$$q''_{conv} = \frac{\dot{m}C_p(T_{out}-T_{in})}{NL(2\eta H_{ch}+W_{ch})} \tag{8.6}$$

Since the calculated heat transfer to fluid using equation (8.6) is 7 % lower than the heat produced by the heaters, this demonstrates that the microchannel heat sink is well insulated. Where, N, L, H_{ch}, W_{ch}, η , T_{out} and T_{in} are number of fins, length, height, width of microchannel, efficiency of fin fluid temperature at outlet and inlet respectively. The efficiency of fin(η)was determined by using equation (8.7) because manifold cover acts like an insulating material at the fin tip. Hence adiabatic fin tip condition is assumed.

$$\eta = \frac{\tanh(mH)}{mH} \tag{8.7}$$

Where, $m = \sqrt{\frac{h_{nf}P}{K_w.A_c}}$

And local convective Heat Transfer Coefficient ($h_{nf,x}$) is evaluated using

$$h_{nf,x} = \frac{q''_{conv}}{(T_{w,x} - T_{bnf,x})} \tag{8.8}$$

The average heat transfer coefficient is calculated as follows:

$$h_{avg} = \int_0^L h_{nf,x}\, dx \tag{8.9}$$

In which $T_{bnf,x}$is the local nanofluid temperature as defined by Eq. (8.11) or (8.10) depending on the region. $T_{w,x}$ is the local wall temperature which can be obtained by assuming one dimensional heat conduction through the substrate.

The wall temperature of the microchannel can be determined by 1D Fourier's heat conduction equation

$$T_{w,x} = T_{tc} - \frac{S * q''_{Conv}}{k_{sol}} \tag{8.10}$$

where k_{sol} represents the thermal conductivity of the metal, T_{tc} represents the temperature reported by the thermocouple, and 'S' represents the distance between the position of the thermocouple and the microchannel surface, which is 5 mm.

The bulk nanofluid temperatures at various locations of a microchannel can be determined using a standard energy balance equation given below.

$$T_{bnf,x} = T_{in} + \frac{N \times x \times (2\eta H_{ch} + W_{ch}) * q''_{Conv}}{\dot{m} C_p} \tag{8.11}$$

In which $'x'$ represents the distance from the beginning of themicrochannel.
And Nusselt number is measured as follows:

$$Nu = \frac{h_{avg} D_h}{k_f} \tag{8.12}$$

The variables "D_h" and "k_f" represent the hydraulic diameter of the channel and the thermal conductivity of the fluid, respectively.

8.3.2 Pressure drop

As fluid moves through the microchannel, it experiences two abrupt contractions and two expansions from inlet to outlet respectively. To obtain a pressure drop across the microchannels (ΔP_{mc}) all the pressure losses associated with these contraction and expansion as well as pressure loss due to elevation will be subtracted from the total pressure drop measured using pressure transducer and differential pressure transducer.

Pressure drop in microchannel:

$$\Delta P_{mc} = \Delta P_{tot} - \left(\Delta P_{con1} + \Delta P_{con2} + \Delta P_{ep1} + \Delta P_{ep2} + \rho g h_r\right) \quad (8.13)$$

Where, ΔP_{con1} , ΔP_{con2} are pressure contractions at inlet, ΔP_{ep1} , ΔP_{ep2} are pressure expansions at exit and are evaluated using the following equations [9]

$$P_{con} = \frac{1}{2}\rho_{nf}(u_2^2 - u_1^2) + \frac{K_{c1}}{2}\rho_{nf}u_2^2 \quad (8.14)$$

$$P_{con2} = \frac{1}{2}\rho_{nf}(u_3^2 - u_2^2) + \frac{K_{c2}}{2}\rho_{nf}u_3^2 \quad (8.15)$$

$$P_{ep1} = \frac{1}{2}\rho_{nf}(u_3^2 - u_4^2) + \frac{K_{e1}}{2}\rho_{nf}u_4^2 \quad (8.16)$$

$$P_{ep2} = \frac{1}{2}\rho_{nf}(u_4^2 - u_5^2) + \frac{K_{e2}}{2}\rho_{nf}u_5^2 \quad (8.17)$$

In these equations, k_{con} and k_{ep} are contraction and expansion coefficients and these values are determined using [91].

8.4 Uncertainty analysis

The uncertainty analysis was carried out to assess the error associated with the equipment used to measure experimental data. The uncertainties of the instruments are listed in Table 8.4. The uncertainty of dependent variables such as thermal resistance, heat transfer coefficient, Nu, friction factor etc were determined using Taylor et al. [92] equation given below. The uncertainty values which correspond to dependent variables are evaluated and listed in Table 8.5.

$$W_R = \left\{\left(\frac{\partial R}{\partial x_1}w_1\right)^2 + \left(\frac{\partial R}{\partial x_2}w_2\right)^2 + \left(\frac{\partial R}{\partial x_3}w_3\right)^2 + \cdots \left(\frac{\partial R}{\partial x_n}w_n\right)^2\right\}^{\frac{1}{2}} \quad (8.18)$$

Where, R is a function of independent variables (X_1, X_2....., X_n) and individual uncertainties of measured variables W_1, W_2, W_3.....W_n.

Table 8.4 Uncertainty of measuring instruments

Parameter	**Uncertainty**
Voltage Measurement, V	0.8 %
Current measurement, A	3 %
Thermocouple	± 0.5 ^{o}C
Pressure Transducer	0.3 % Full scale
Differential Pressure Transducer	1.0 % Full scale
Channel width, length and height, fin width and length	0.1 %-0.2 %

Table 8.5 Uncertainty of estimated data

Parameter	**Uncertainty**
Hydraulic diameter	0.29 %
Reynolds number	0.23 %
Friction factor	1.04 %
Heat flux	3.1 %
h	4.0 %
Nu	4.02 %

8.5 Flow characteristics

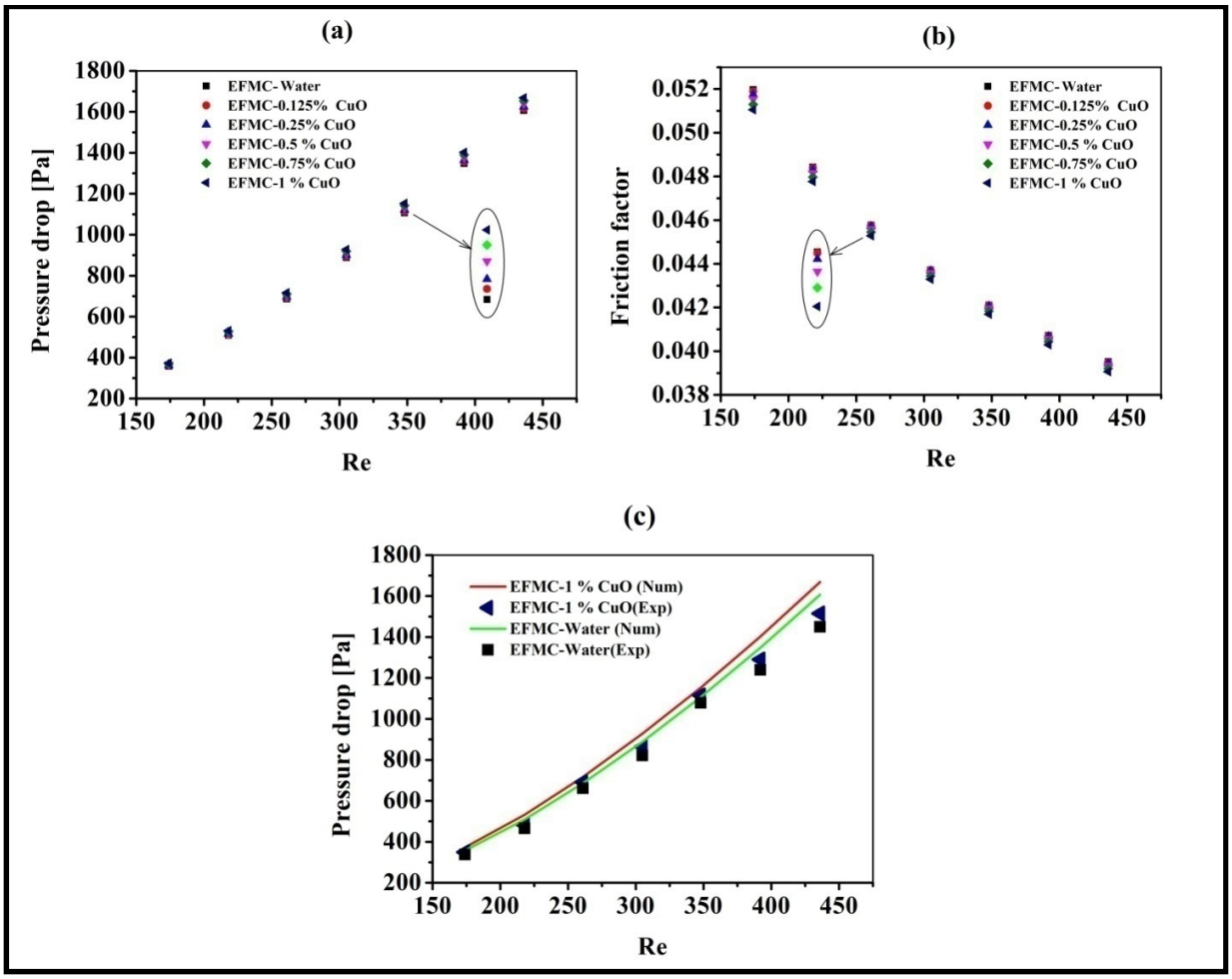

Figure 8.9 Effect of pure water and CuO-water nanofluid concentrations on (a) pressure drop (b) friction factor in EFMC at different Re (c) experimental and numerical results of water and 1% CuO-water nanofluid

The pressure drop for pure water and CuO-water nanofluid at different nanoparticle concentrations is demonstrated in Figure 8.10(a). It indicates that with the enhancement of nanoparticle concentration, the pressure drop increases across the micro channel. The reason for this was already discussed in chapter 7. The percentage increase of pressure for various nanoparticle concentrations 0.125 %, 0.25 %, 0.50 %, 0.75 % and 1 % are 0.63 %, 1.3 %, 2.4 %, 3.5 % and 5 % respectively for an Re of 174. The maximum rise in pressure drop has

been recorded as 5 % for Re 174 at 1% volume concentration of CuO nanoparticles over water. It indicates that, in EFMC, the percentage rise in pressure drop for CuO-water nanofluid and pure water are almost same. Therefore, CuO-water nanofluids have proven to be a good cooling fluid, even though pressure drop in EFMC rises with the volume fraction of CuO-water nanofluid.

Figure 8.9(b) illustrates the effect concentration of nanofluids on friction factor and this was compared with pure water. A volume concentration of 0.125 % to 1 % CuO-Water nanofluids and a particle diameter of 40 nm were considered in this analysis. As seen in Figure 8.9(b), friction factor reduces with an increase in Re, this behaviour is analogous to that of water in EFMC. Friction factor varies inversely with the square of fluid velocity, as shown in equation 3.18. The use of nanofluids in microchannel marginally raises friction factor. Because nanoparticles are so small, nanofluids with low concentrations do not cause significant pressure penalty as shown in Figure 8.9(b). The experimental and numerical results are in good agreement and that is shown in figure 8.9(c)

8.6 Heat transfer characteristics

Figure 8.10(a) depicts the impact of CuO particle concentration on wall temperature of the microchannel. For a constant Re of 174, with an increase in the particle concentration of CuO significantly reduces the wall temperature of heat sink. The reduction in wall temperature for various particle concentrations of 0.125 %, 0.25 %, 0.50 %, 0.75 % and 1 % are 3 %, 5 %, 8.1 %, 10.6 % and 12 % respectively. For constant volume fraction 1 %, an increase in Re from 174-438 further reduces the wall temperature by 34 %. Hence, the maximum reduction in wall temperature was recorded as 34 % for Re 438 at 1 % volume concentration of CuO nanoparticles.

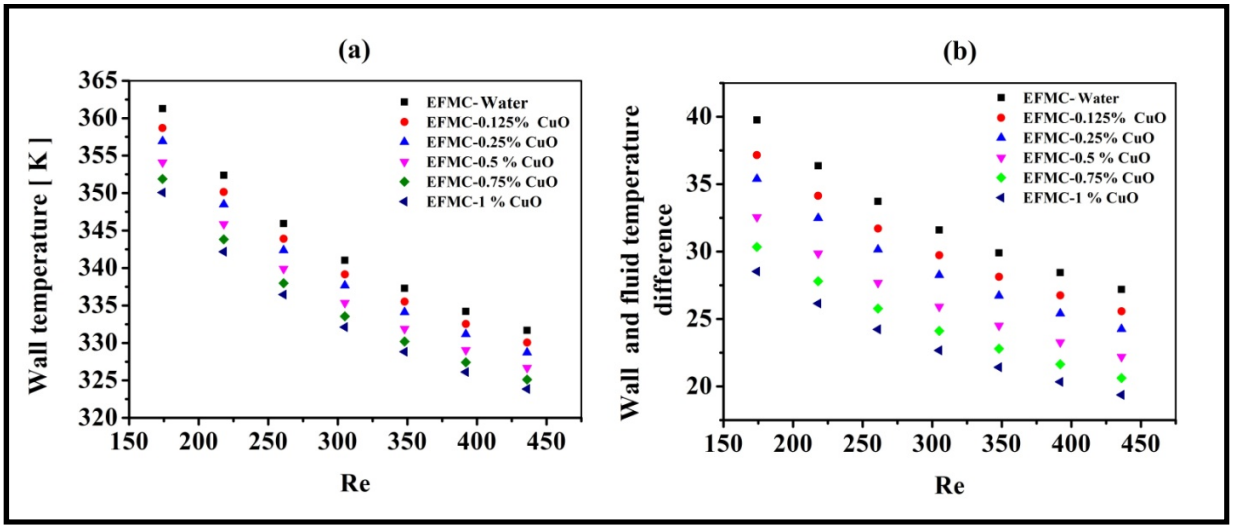

Figure 8.10 Effect of pure water and CuO-water nanofluid concentrations on (a) wall temperature (b) wall and fluid temperature difference in EFMC at different Re.

Figure 8.10(b) illustrates variation of temperature difference between microchannel wall and fluid with nanoparticle concentration and Reynolds number. For a constant Re of 174, an increase in the particle concentration of CuO reduces the temperature difference between wall and fluid. This reduction in the temperature difference is more rapid with particle concentration as seen in Figure 8.10(b). For Re 174, the reduction in the temperature difference between wall and fluid for various particle concentrations of 0.125 %, 0.25 %, 0.50 %, 0.75 % and 1 % are 6.5 %, 11 %, 18.1 %, 23.7 % and 28.3 % respectively. For constant volume fraction 1 %, an increase in Re from 174-438 further reduces the wall temperature by 32 %. Hence, the maximum reduction in wall temperature was recorded as 32 % for Re 438 at 1 % volume concentration of CuO nanoparticles.

Figure 8.11(a) depicts that with an increase in the particle concentration of CuO from 0.125 % to 1 %, there is a significant enhancement in Nu. For a constant Re of 174, Nu is 16.1 for a volume concentration of 1 % compared to pure water. Moreover, it can also be inferred that with an increase in Re the Nu increases. This happens because the convective heat transfer coefficient increases with increase in the velocity of the flowing fluid. An increase in Nu for various particle concentrations of 0.125 %, 0.25 %, 0.50 %, 0.75 % and 1 % are 12.6, 13, 14, 14.9 and 16.2 respectively. Moreover, Nu further increased by increasing Reynolds number from 174 to 438. The maximum Nu of 23 was achieved with 1 % CuO-

Water nanofluid at Re of 438, which was 28 % higher than pure water in EFMC. Therefore, it can be concluded that nanofluid is undoubtedly superior to water for enhancing heat transfer in EFMC.

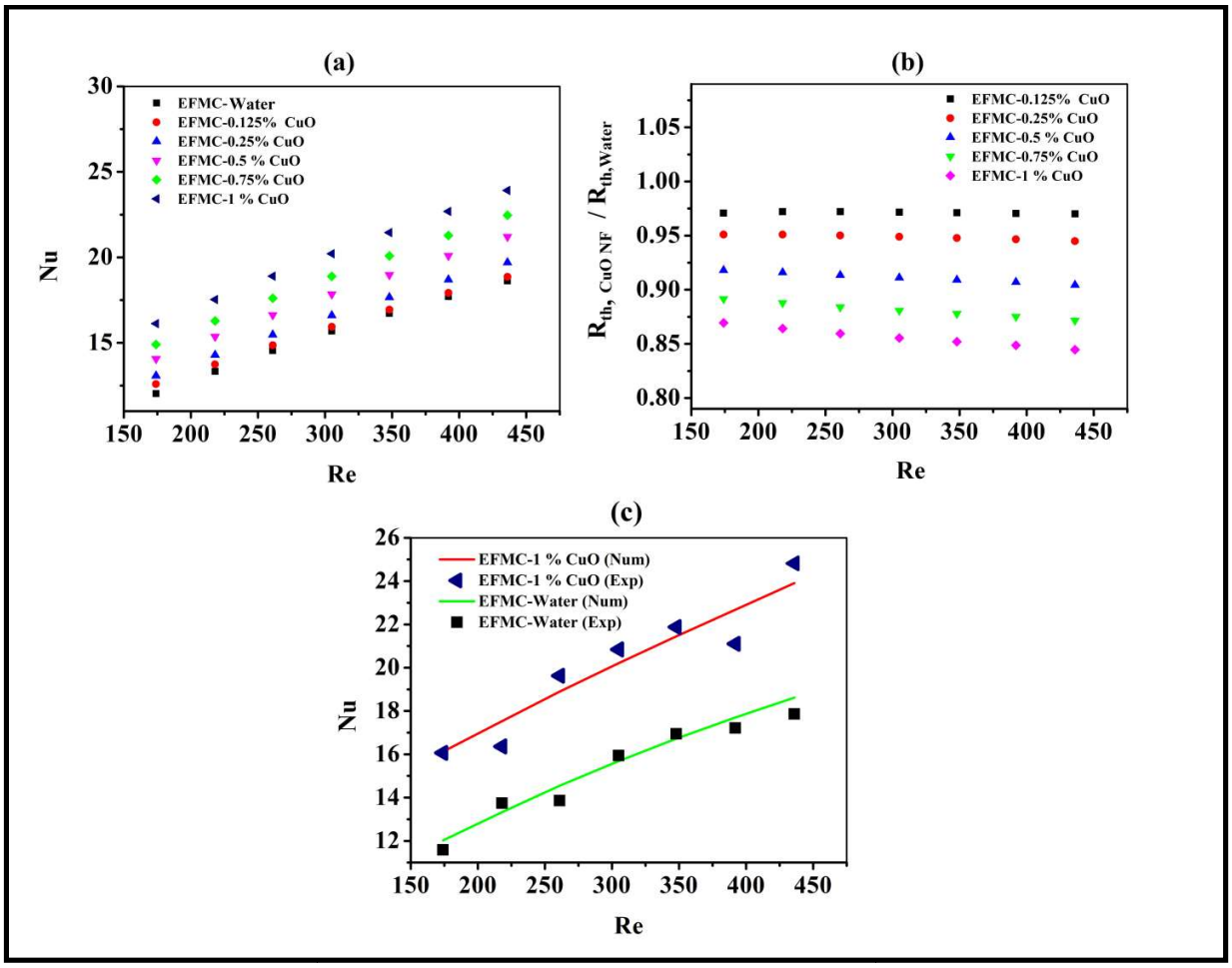

Figure 8.11 Effect of pure water and CuO-water nanofluid concentrations on (a) Nu (b) thermal resistance ratio in EFMC at different Re (c) experimental and numerical results of water and 1% CuO-water nanofluid.

Thermal resistance can be determined using equation 3.20. Figure 8.11(b) highlights that the thermal resistance ratio is inversely proportional to nanoparticle concentration and Re. Increasing the concentration of CuO nanoparticles from 0.125 % to 1 % and Re from 178 to 438 leads to a noticeable reduction in the thermal resistance ratio. For a constant Re of 174, the reduction in thermal resistance was 2.9 %, 4.9 %, 8.1 %, 10.8 % and 13 % for

particle concentrations of 0.125 %, 0.25 %, 0.50 %, 0.75 % and 1 % respectively. This happens because the maximum wall temperature of EFMC decreases with increasing CuO nanoparticle concentration. It is also observed that the thermal resistance of the nanofluid further decreases with an increase in Re from 174 to 438. For higher Reynolds number, the reduction in thermal resistance ratio is more rapid due to increased Brownian motion of particle with velocity and as a consequence, thermal transport increases as well. The highest reduction in thermal resistance of 15 % was noted for 1 % volume concentration of CuO-water nanofluid at Re of 438. The experimental and numerical results are in good agreement and that is shown in figure 8.11(c)

Fig 8.12(a) describes that with an increase in the nanoparticle concentration of CuO the pumping power increases due to an increase in the density of the nanofluid. The pumping power was maximum for 1 % volume concentration and minimum for pure water. However, no significant difference in pumping power was observed. It was further evident that the pumping power rises by a significant amount with an increase in the Reynolds number. The pumping power required is higher for achieving higher velocity of the flowing fluid. The maximum rise in pumping power of 4.4 % was observed for 1 % CuO-water nanofluid at Re 438.

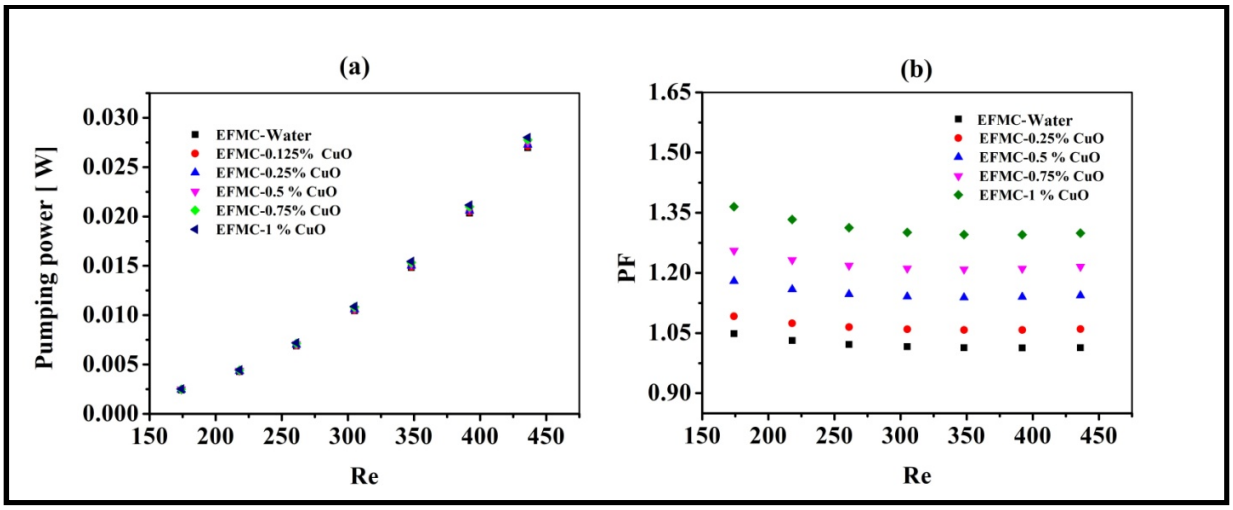

Figure 8.12 Effect of pure water and CuO-water nanofluid concentrations on (a) pumping power (b) PF in EFMC at different Re.

Figure 8.12(b) shows variation of PF for various volume fractions of CuO nanofluid and Re. The performance factor increases with an increase in nanoparticle concentration in base fluid. This is because an increase in effective Nusselt number is more prominent than an increase in effective friction factor.It is seen from figure 8.12(b) that higher volume fraction of CuO nanofluid shows higher PF. At higher concentrations, the thermal conductivity of nanofluid increases, which in turn led to an increase in convective heat transfer capacity of nanofluids.The maximum performance factor enhancement of 36 % was noted at Re 438 for 1 % CuO-Water nanofluid. It is also clear from Figure 8.12(b) that, an increase in Re does not have a significant impact on PF.

8.7 Conclusions

In this study, the effect of flow and heat transfer characteristic of optimized EFMC heat sink on particle concentration of 0.15 %, 0.25 %, 0.5 %, 0.75 % and 1 % was examined experimentally. In addition, other parameters such as average wall temperature, Nusselt number, and friction factor and performance factor variation with Reynolds number and particle concentration were evaluated. Based on the results, the following conclusion can be made.

- Adding nanoparticles to base fluid increases viscosity of fluid which in turn raises the pressure drop in optimized elliptical fin microchannel over conventional fluid. An increase in the volume concentration of CuO-particles from 0.125 % to 1 % results in a maximum pressure increase of 5 %.
- In an optimized elliptical fin microchannel, the maximum reduction of wall temperature of 12 % was recorded for 1 % CuO-Water nanofluid at Re 438. It was also found that Nu increased by 42 % when 1 % CuO-Water nanofluid was used in an optimised elliptical fin microchannel instead of conventional fluid for the same Re.
- For higher Re, the reduction in thermal resistance ratio was more rapid due to increased Brownian motion of particle with velocity and as a consequence, thermal transport increased as well. The highest reduction in thermal resistance of 15 % was evident for a 1 % volume concentration of CuO-water nanofluid at Re 438.

- The pumping power was found to increase significantly with a rise in Re when compared to rise in nanoparticle concentration. At Re 438, 1 % CuO-water nanofluid was found to have increased pumping power of 4.4 % compared to the conventional fluid. Hence, nanofluids were proved to be better cooling fluids for microchannels heat sinks.
- Moreover, results from both experiments and computations were found to be identical, with only a small percentage of deviation**.**

CHAPTER 9

Overall conclusions and scope for future research

9.1 Overall conclusions

The present numerical and experimental analysis was aimed to enhance the heat transfer performance of a microchannel heat sink. Initially, a double-tapered microchannel was analyzed, with taper provided on both side walls as well as on the bottom wall. This taper induced a converging and diverging effect in the heat sink and resulted in more uniform wall temperature and improved heat transfer performance. This design led to the selection of an elliptical fin microchannel, which naturally induced converging and diverging flow patterns and showed enhanced heat transfer performance. The elliptical fin microchannels were then investigated by varying the orientation angle and heat fluxes. Later, an optimized elliptical fin microchannel was evaluated by varying parameters such as ellipticity ratio, fin orientation, channel depth, and fin-to-fin center distance to further enhance the heat transfer capabilities of the elliptical fin microchannel. Finally, the optimized elliptical fin microchannel heat sink was tested with nanofluids to examine the effects of flow and heat transfer characteristics on particle concentration. Based on the results, the following conclusions are drawn.

- Elliptical fin microchannels naturally have a converging and diverging flow patterns due to their shape. The converging and diverging flow patterns in elliptical fin microchannels induce vigorous mixing of the fluid, which leads to more efficient heat transfer and lower wall temperatures compared to double-tapered microchannels. This is due to the fact that the fluid is forced to change direction and velocity as it flows over the elliptical fins. The improved mixing also helps to prevent hot spots and temperature gradients from forming along the walls of the microchannel, resulting in a more uniform distribution of temperature and heat.
- The thermal performance of the elliptical fin microchannel heat sink was further improved by orienting the elliptical fin at an angle to the flow stream. This orientation promoted flow mixing and generated secondary flow in the microchannel, which

disrupted the development of the boundary layer and caused the boundary layer to re-initialize at each fin in the downstream direction of the channel. As a result, the heat transfer rate was increased, and the temperature distribution along the stream wise direction became more uniform, ultimately enhancing the reliability of high heat flux generating devices.

- The results of the parametric analysis conducted on the elliptical fin microchannel demonstrated that the optimal channel dimensions induced vigorous flow mixing and reduced the boundary layer thickness, resulting in enhanced heat transfer with minimal pressure penalty. The maximum performance factor achieved was 1.61, which represented an improvement over the straight fin microchannel. Therefore, these findings suggest that the optimized elliptical fin microchannel has the potential to further enhance the performance of heat sinks in high heat flux applications, making it a promising technology for future development.
- The thermal performance of the elliptical fin microchannel was further improved by replacing water with nanofluids, in addition to optimizing its geometry. Among the nanofluids tested, CuO-water nanofluid was found to be the most suitable. The use of CuO-water nanofluid in the optimized channel resulted in an increment of up to 42 % in the Nusselt number (Nu). This finding suggests that the use of nanofluids in combination with the optimized elliptical fin microchannel has great potential to further improve the thermal performance of heat sinks.

9.2 Scope for future research

Even though a significant amount of research has already been done on the elliptical fin design, there is still a need for even more research on the topic.

- To enhance the heat transfer rate, it is crucial to increase the surface area in contact with the liquid medium. Filling microchannels with porous material or designing elliptical fins with porous material is a promising approach to achieve this objective. Thus, exploring the impact of porosity on thermal performance of elliptical fin heat sinks with porous fins across different porosity ranges could be a potential area for future research.

- The effect of fluid flow entry and exit location as well as the design of the manifold plays an important role in the enhancement of heat transfer. Thus, research needs to be conducted on the manifold design and its location for elliptical microchannel heat sink.

- The effect of flow boiling of hybrid nanofluid and their mixture ratio plays a crucial in improving thermal performance of elliptical fin microchannel due to their high heat transfer coefficient. Thus, an extensive research is required to understand the valuable insights that influence the heat transfer performance of hybrid nanofluid. This research could potentially be applied to the cooling of solar panels to maintain the reliability and performance of the heat sink.

- From the numerical analysis, it is evident that the elliptical fin microchannel enhances fluid mixing, while the double-tapered microchannel provides a uniform bottom wall temperature. To further improve the heat transfer performance, a combination of a double-tapered and elliptical fin microchannel heat sink could be a potential area for future research.

Publications

1. Heat transfer enhancement using double taper microchannel. *Proceedings of the Institution of Mechanical Engineers, Part E: Journal of Process Mechanical Engineering*doi:10.1177/09544089211052738 *(SCI)*

2. Heat transfer enhancement using elliptical fin microchannel. *Asia-Pacific Journal of Chemical Engineering* doi:10.1002/apj.2712 *(SCI)*

3. Numerical modelling of nanofluid based microchannel heat sink. *International Journal of Advanced Trends in Computer Applications (IJATCA))* http://ijatca.com/specialissue/Volume1/Number1/sp19010131(WOS)

4. Comparative study elliptical and oblique micro-fin heat sink. *Asia-Pacific Journal of Chemical Engineering,* Wiley https://doi.org/10.1002/apj.2834 *(SCI)*

5. A parametric study to enhance cooling performance of elliptical fin microchannel heat sink. *International Journal of Heat and Mass Transfer (Under review) SCI*

6. Numerical and experimental study of nanofluids in optimized elliptical fin microchannel heat sink *(To be communicated)SCI*

References

[1] D.B Tukerman R.F.W Pease, "High-performance heat sinking for VLSI," *IEEE Electron Device Letters*, vol. 2, no. 5, pp. 126–129, 1981.

[2] S. S. Mehendale, A. M. Jacobi, and R. K. Shah, "Fluid flow and heat transfer at micro- and meso-scales with application to heat exchanger design," *Applied Mechanics Reviews*, vol. 53, no. 7, pp. 175–193, 2000.

[3] E. Choi, Stephen U.S., "Enhancing thermal conductivity of fluids with nanoparticles," in *ASME International Mechanical Engineering Congress and Exposition proceedings*, 1995.

[4] D. Wen, G. Lin, S. Vafaei, and K. Zhang, "Review of nanofluids for heat transfer applications," *Particuology*, vol. 7, no. 2, pp. 141–150, 2009.

[5] D. Liu and S. V. Garimella, "Investigation of liquid flow in microchannels," *8th AIAA / ASME Joint Thermophysics and Heat Transfer Conference*, vol. 18, no. 1, pp. 65–72, 2002.

[6] S. G. Kandlikar and W. J. Grande, "Evolution of microchannel flow passages-thermohydraulic performance and fabrication technology," *ASME International Mechanical Engineering Congress and Exposition, Proceedings*, vol. 24, pp. 59–72, 2002.

[7] S. G. K. mark E. steinke, "Single -phase liquid heat transfer in microchannels," *ASME 3rd International Conference on Microchannels and Minichannels*, vol. 41855, pp. 667–678, 2005.

[8] P. S. Lee, S. V. Garimella, and D. Liu, "Investigation of heat transfer in rectangular microchannels," *International Journal of Heat and Mass Transfer*, vol. 48, no. 9, pp. 1688–1704, 2005.

[9] W. Qu and I. Mudawar, "Experimental and numerical study of pressure drop and heat transfer in a single-phase micro-channel heat sink," *International Journal of Heat and Mass Transfer*, vol. 45, no. 12, pp. 2549–2565, 2002.

[10] Y. K. Prajapati, "Influence of fin height on heat transfer and fluid flow characteristics of rectangular microchannel heat sink," *International Journal of Heat and Mass Transfer*, vol. 137, pp. 1041–1052, 2019.

[11] E. M. Abo-Zahhad, S. Ookawara, A. Radwan, M. F. Elkady, and A. H. El-Shazly, "Optimization of stepwise varying width microchannel heat sink for high heat flux applications," *Case Studies in Thermal Engineering*, vol. 18, p. 100587, 2020.

[12] L. Liebenberg and J. P. Meyer, "Constructal cooling channels for micro-channel heat sinks," *International Journal of Heat and Mass Transfer*, vol. 50, no. 21–22, pp. 4141–4150, 2007.

[13] A. M. Sahar, J. Wissink, M. M. Mahmoud, T. G. Karayiannis, and M. S. Ashrul Ishak, "Effect of hydraulic diameter and aspect ratio on single phase flow and heat transfer in a rectangular microchannel," *Applied Thermal Engineering*, vol. 115, pp. 793–814, 2017.

[14] C. Zhang, Y. Chen, and M. Shi, "Effects of roughness elements on laminar flow and heat transfer in microchannels," *Chemical Engineering and Processing: Process Intensification*, vol. 49, no. 11, pp. 1188–1192, 2010.

[15] W. Qu, S. M. Yoon, and I. Mudawar, "Two-phase flow and heat transfer in rectangular micro-channels," *Journal of Electronic Packaging, Transactions of the ASME*, vol. 126, no. 3, pp. 288–300, 2004.

[16] A. Bordbar, A. Taassob, A. Zarnaghsh, and R. Kamali, "Slug flow in microchannels: numerical simulation and applications," *Journal of Industrial and Engineering Chemistry*, vol. 62, pp. 26–39, 2018.

[17] E. Y. K. Ng and S. T. Poh, "Investigative study of manifold microchannel heat sinks for electronic cooling design," *Journal of Electronics Manufacturing*, vol. 9, no. 2, pp. 155–166, 1999.

[18] P. Zajac, "Comparison of cooling performance of manifold and straight microchannel heat sinks using CFD simulation," *2021 22nd International Conference on Thermal, Mechanical and Multi-Physics Simulation and Experiments in Microelectronics and Microsystems, EuroSimE 2021*, pp. 1–4, 2021.

[19] S. Hsieh and C. Lin, "International Journal of Heat and Mass Transfer Convective heat transfer in liquid microchannels with hydrophobic and hydrophilic surfaces," *International Journal of Heat and Mass Transfer*, vol. 52, no. 1–2, pp. 260–270, 2009.

[20] S. Rahbarshahlan, E. Esmaeilzadeh, and A. R. Khosroshahi, "Numerical simulation of fluid flow and heat transfer in microchannels with patterns of hydrophobic / hydrophilic walls," *The European Physical Journal Plus*, vol. 123, pp. 135–157, 2020.

[21] M. K. Moharana and S. Khandekar, “Effect of aspect ratio of rectangular microchannels on the axial back conduction in its solid substrate,” *Progress in Microscale and Nanoscale Thermal and Fluid Sciences*, vol. 4, no. 3, pp. 205–224, 2015.

[22] Y.M. Zhang and C. P. L. J.C. Han, “Augmented heat transfer in square channels with parallel, crossed, and v-shaped angled ribs,” *J. Heat Transfer*, vol. 113, pp. 591–596, 1991.

[23] N. Raja, H. A. Mohammed, and C. W. Lim, “Thermal and hydraulic characteristics of nanofluid in a triangular grooved microchannel heat sink (TGMCHS),” *Applied Mathematics and Computation*, vol. 246, pp. 168–183, 2014.

[24] S. Gururatana, “Numerical Simulation of Micro-Channel Heat Sink with Dimpled Surfaces,” *American Journal of Applied Sciences*, vol. 9, no. 3, pp. 399–404, 2012.

[25] G. Wang, D. Niu, F. Xie, Y. Wang, X. Zhao, and G. Ding, “Experimental and numerical investigation of a microchannel heat sink (MCHS) with micro-scale ribs and grooves for chip cooling,” *Applied Thermal Engineering*, vol. 85, pp. 61–70, 2015.

[26] Y. F. Li, G. D. Xia, D. D. Ma, Y. T. Jia, and J. Wang, “Characteristics of laminar flow and heat transfer in microchannel heat sink with triangular cavities and rectangular ribs,” *International Journal of Heat and Mass Transfer*, vol. 98, pp. 17–28, 2016.

[27] Q. Zhu *et al.*, “Characteristics of heat transfer and fluid flow in microchannel heat sinks with rectangular grooves and different shaped ribs,” *Alexandria Engineering Journal*, vol. 59, no. 6, pp. 4593–4609, 2020.

[28] L. Chai, G. Xia, M. Zhou, J. Li, and J. Qi, “Optimum thermal design of interrupted microchannel heat sink with rectangular ribs in the transverse microchambers,” *Applied Thermal Engineering*, vol. 51, no. 1–2, pp. 880–889, 2013.

[29] K. Wong and J. Lee, “Investigation of thermal performance of microchannel heat sink with triangular ribs in the transverse microchambers ☆,” *International Communications in Heat and Mass Transfer*, vol. 65, pp. 103–110, 2015.

[30] Y. Li, F. Zhang, B. Sunden, and G. Xie, “Laminar thermal performance of microchannel heat sinks with constructal vertical Y-shaped bifurcation plates,” *Applied Thermal Engineering*, vol. 73, no. 1, pp. 185–195, 2014.

[31] G. Wang, N. Qian, and G. Ding, “International Journal of Heat and Mass Transfer Heat transfer enhancement in microchannel heat sink with bidirectional rib,” *International*

Journal of Heat and Mass Transfer, vol. 136, pp. 597–609, 2019.

[32] K. Kumar and P. Kumar, "Effect of groove depth on hydrothermal characteristics of the rectangular microchannel heat sink," *International Journal of Thermal Sciences*, vol. 161, no. November 2020, p. 106730, 2021.

[33] G. Xie, H. Shen, and C. Wang, "Parametric study on thermal performance of microchannel heat sinks with internal vertical Y-shaped bifurcations," *International Journal of Heat and Mass Transfer*, vol. 90, pp. 948–958, 2015.

[34] W. Qu, G. M. Mala, and D. Li, "Heat transfer for water flow in trapezoidal silicon microchannels," *International Journal of Heat and Mass Transfer*, vol. 43, no. 21, pp. 3925–3936, 2000.

[35] A. A. Alfaryjat, H. A. Mohammed, N. Mariah, M. K. A. Arif, and M. I. Najafabadi, "Influence of geometrical parameters of hexagonal , circular , and rhombus microchannel heat sinks on the thermohydraulic characteristics," *International Communications in Heat and Mass Transfer*, vol. 52, pp. 121–131, 2014.

[36] H. Wang, Z. Chen, and J. Gao, "Influence of geometric parameters on flow and heat transfer performance of micro-channel heat sinks," *Applied Thermal Engineering*, vol. 107, pp. 870–879, 2016.

[37] H. Khorasanizadeh and M. Sepehrnia, "Performance evaluation of a trapezoidal microchannel heat sink with various entry / exit configurations utilizing variable properties," *Journal of Applied Fluid Mechanics*, vol. 10, no. 6, pp. 1547–1559, 2017.

[38] L. Su, Z. Duan, B. He, H. Ma, and G. Ding, "Laminar flow and heat transfer in the entrance region of elliptical minichannels," *International Journal of Heat and Mass Transfer*, vol. 145, p. 118717, 2019.

[39] T. Hung and W. Yan, "Effects of tapered-channel design on thermal performance of microchannel heat sink," *International Communications in Heat and Mass Transfer*, vol. 39, no. 9, pp. 1342–1347, 2012.

[40] T. C. Hung, T. S. Sheu, and W. M. Yan, "Optimal thermal design of microchannel heat sinks with different geometric configurations," *International Communications in Heat and Mass Transfer*, vol. 39, no. 10, pp. 1572–1577, 2012.

[41] V. S. Duryodhan, S. G. Singh, and A. Agrawal, "Liquid flow through a diverging microchannel," *Microfluidics and Nanofluidics*, vol. 14, no. 1–2, pp. 53–67, 2013.

[42] V. S. Duryodhan, S. G. Singh, and A. Agrawal, “Liquid flow through converging microchannels and a comparison with diverging microchannels,” *Journal of Micromechanics and Microengineering*, vol. 24, no. 12, p. 125002, 2014.

[43] M. Dehghan, M. Daneshipour, M. S. Valipour, and R. Rafee, “Enhancing heat transfer in microchannel heat sinks using converging flow passages,” *Energy Conversion and Management*, vol. 92, pp. 244–250, 2015.

[44] K. X. Cheng, Y. S. Chong, and K. T. Ooi, “Thermal-hydraulic performance of a tapered microchannel,” *International Communications in Heat and Mass Transfer*, vol. 94, no. April, pp. 53–60, 2018.

[45] M. Dehghan, M. Daneshipour, M. S. Valipour, R. Rafee, and S. Saedodin, “Enhancing heat transfer in microchannel heat sinks using converging flow passages,” *Energy Conversion and Management*, vol. 92, pp. 244–250, 2015.

[46] K. Vafai and L. Zhu, “Analysis of two-layered micro-channel heat sink concept in electronic cooling electronic cooling,” *International Journal of Heat and Mass Transfer*, vol. 42, no. 12, pp. 2287–2297, 1999.

[47] T. C. Hung, W. M. Yan, and W. P. Li, “Analysis of heat transfer characteristics of double-layered microchannel heat sink,” *International Journal of Heat and Mass Transfer*, vol. 55, no. 11–12, pp. 3090–3099, 2012.

[48] J. M. Wu, J. Y. Zhao, and K. J. Tseng, “Parametric study on the performance of double-layered microchannels heat sink,” *Energy Conversion and Management*, vol. 80, pp. 550–560, 2014.

[49] B. Osanloo, A. Mohammadi-Ahmar, A. Solati, and M. Baghani, “Performance enhancement of the double-layered micro-channel heat sink by use of tapered channels,” *Applied Thermal Engineering*, vol. 102, pp. 1345–1354, 2016.

[50] B. Wei, M. Yang, Z. Wang, H. Xu, and Y. Zhang, “Flow and thermal performance of a water-cooled periodic transversal elliptical microchannel heat sink for chip cooling,” *Journal of Nanoscience and Nanotechnology*, vol. 15, no. 4, pp. 3061–3066, 2015.

[51] H. Sadique, Q. Murtaza, and Samsher, “Heat transfer augmentation in microchannel heat sink using secondary flows: A review,” *International Journal of Heat and Mass Transfer*, vol. 194, p. 123063, 2022.

[52] Y. J. Lee, P. K. Singh, and P. S. Lee, “International Journal of Heat and Mass Transfer

Fluid flow and heat transfer investigations on enhanced microchannel heat sink using oblique fins with parametric study," *International Journal of Heat and Mass Transfer*, vol. 81, pp. 325–336, 2015.

[53] S. S. Panse and S. V. Ekkad, "A numerical parametric study to enhance thermal hydraulic performance of a novel alternating offset oblique microchannel," *Numerical Heat Transfer; Part A: Applications*, vol. 79, no. 7, pp. 489–512, 2021.

[54] N. Irmawati, R. Zulki, and P. Gunnasegaran, "In fluence of the oblique fin arrangement on the fluid flow and thermal performance of liquid cold plate," *Case Studies in Thermal Engineering*, vol. 12, no. October, pp. 717–727, 2018.

[55] S. S. Yogesh, A. S. Selvaraj, D. K. Ravi, T. Karuppa, and R. Rajagopal, "International Journal of Heat and Mass Transfer Heat transfer and pressure drop characteristics of inclined elliptical fin tube heat exchanger of varying ellipticity ratio using CFD code," *International Journal of Heat and Mass Transfer*, vol. 119, pp. 26–39, 2018.

[56] P. A. Deshmukh and R. M. Warkhedkar, "Thermal performance of elliptical pin fin heat sink under combined natural and forced convection," *Experimental Thermal and Fluid Science*, vol. 50, pp. 61–68, 2013.

[57] A. Al and W. H. Khalil, "Three- dimensional computational comparison of mini pinned heat sinks using different nanofluids : Part one — the hydraulic - thermal characteristics," *Heat Transfer - Asian Research*, vol. 49, no. 1, pp. 591–613, 2019.

[58] S. V. Jadhav, P. M. Pawar, and B. P. Ronge, "Effect of pin-fin geometry on microchannel performance," *Chemical Product and Process Modeling*, vol. 14, no. 1, pp. 1–15, 2019.

[59] S. V. Jadhav and P. M. Pawar, "Performance analysis of microchannel with different pin fin layouts," *International Journal of Numerical Modelling: Electronic Networks, Devices and Fields*, vol. 33, no. 2, pp. 1–19, 2020.

[60] S. V. Jadhav, P. M. Pawar, A. B. Shinde, and S. S. Wangikar, "Performance Analysis of Elliptical Pin Fins in the Microchannels," *Proceedings of the 2nd International Conference on Advanced Technologies for Societal Applications*, vol. 2, pp. 295–304, 2020.

[61] R. Saidur, K. Y. Leong, and H. A. Mohammed, "A review on applications and challenges of nanofluids," *Renewable and Sustainable Energy Reviews*, vol. 15, no. 3. pp. 1646–1668, 2011.

[62] L. Sun, L. Yang, N. Zhao, J. Song, X. Li, and X. Wu, “A review of multifunctional applications of nanofluids in solar energy,” *Powder Technology*, vol. 411, p. 117932, 2022.

[63] B. Mehta, D. Subhedar, H. Panchal, and Z. Said, “Synthesis, stability, thermophysical properties and heat transfer applications of nanofluid – A review,” *Journal of Molecular Liquids*, vol. 364, p. 120034, 2022.

[64] J. P. Vallejo, J. I. Prado, and L. Lugo, “Hybrid or mono nanofluids for convective heat transfer applications. A critical review of experimental research,” *Applied Thermal Engineering*, vol. 203, p. 117926, 2022.

[65] W. Ajeeb and S. M. S. Murshed, “Nanofluids in compact heat exchangers for thermal applications: A State-of-the-art review,” *Thermal Science and Engineering Progress*, vol. 30, p. 101276, 2022.

[66] A. Chandravadhana, V. NandaKumar, and K. Venkatramanan, “Mono and hybrid nanofluid based heat sink technologies - A review,” *Journal of Physics: Conference Series*, vol. 1644, no. 1, 2020.

[67] G. Colangelo, E. Favale, M. Milanese, A. de Risi, and D. Laforgia, “Cooling of electronic devices: Nanofluids contribution,” *Applied Thermal Engineering*, vol. 127, pp. 421–435, 2017.

[68] E. C. Okonkwo, I. Wole-Osho, I. W. Almanassra, Y. M. Abdullatif, and T. Al-Ansari, *An updated review of nanofluids in various heat transfer devices*, vol. 145, no. 6. 2021.

[69] S. M. Sohel Murshed and C. A. Nieto de Castro, “A critical review of traditional and emerging techniques and fluids for electronics cooling,” *Renewable and Sustainable Energy Reviews*, vol. 78, pp. 821–833, 2017.

[70] M. Bahiraei and S. Heshmatian, “Electronics cooling with nanofluids: A critical review,” *Energy Conversion and Management*, vol. 172, pp. 438–456, 2018.

[71] R. Chein and G. Huang, “Analysis of microchannel heat sink performance using nanofluids,” *Applied Thermal Engineering*, vol. 25, pp. 3104–3114, 2005.

[72] S. E. Ghasemi, A. A. Ranjbar, and M. J. Hosseini, “Numerical study on effect of CuO-water nanofluid on cooling performance of two different cross-sectional heat sinks,” *Advanced Powder Technology*, vol. 28, no. 6, pp. 1495–1504, 2017.

[73] Z. Azizi, A. Alamdari, and M. R. Malayeri, “Convective heat transfer of Cu-water

nanofluid in a cylindrical microchannel heat sink," *Energy Conversion and Management*, vol. 101, pp. 515–524, 2015.

[74] S. P. Jang and S. U. S. Choi, "Cooling performance of a microchannel heat sink with nanofluids," vol. 26, pp. 2457–2463, 2006.

[75] J. Jung, H. Oh, and H. Kwak, "International Journal of Heat and Mass Transfer Forced convective heat transfer of nanofluids in microchannels," *International Journal of Heat and Mass Transfer*, vol. 52, no. 1–2, pp. 466–472, 2009.

[76] C. J. Ho, J. K. Peng, T. F. Yang, S. Rashidi, and W. M. Yan, "On the assessment of the thermal performance of microchannel heat sink with nanofluid," *International Journal of Heat and Mass Transfer*, vol. 201, p. 123572, 2023.

[77] M. Ghazvini and H. Shokouhmand, "Investigation of a nanofluid-cooled microchannel heat sink using Fin and porous media approaches," *Energy Conversion and Management*, vol. 50, no. 9, pp. 2373–2380, 2009.

[78] H. A. Mohammed, P. Gunnasegaran, and N. H. Shuaib, "Heat transfer in rectangular microchannels heat sink using nanofluids," *International Communications in Heat and Mass Transfer*, vol. 37, no. 10, pp. 1496–1503, 2010.

[79] S. M. Peyghambarzadeh, S. H. Hashemabadi, A. R. Chabi, and M. Salimi, "Performance of water based CuO and Al_2O_3 nanofluids in a Cu-Be alloy heat sink with rectangular microchannels," *Energy Conversion and Management*, vol. 86, pp. 28–38, 2014.

[80] X. C. Helin Wang, "Performance improvements of microchannel heat sink using Koch fractal structure and nanofluids," *Structures*, vol. 50, pp. 1222–1231, 2023.

[81] A. Sakanova, J. Zhao, and K. J. Tseng, "Investigation on the Influence of Nanofluids in Wavy Microchannel Heat Sink," *IEEE Transactions on Components, Packaging and Manufacturing Technology*, vol. 5, pp. 956–970, 2015.

[82] F. P. Incropera, "Convection Heat Transfer in Electronic Equipment Cooling," vol. 110, pp. 1097–1111, 1988.

[83] F. Incorpera, *Liquid Cooling of Electronic Devices by Single-Phase Convection*. New York: Wiley, 1999.

[84] Y. J. Lee, P. S. Lee, and S. K. Chou, "Enhanced thermal transport in microchannel using oblique fins," *Journal of Heat Transfer*, vol. 134, no. 10, pp. 1–10, 2012.

[85] C. Leng, X. D. Wang, and T. H. Wang, "An improved design of double-layered

microchannel heat sink with truncated top channels," *Applied Thermal Engineering*, vol. 79, pp. 54–62, 2015.

[86] Y. J. Lee, P. S. Lee, and S. K. Chou, "Numerical study of fluid flow and heat transfer in the enhanced microchannel with oblique fins," *Journal of Heat Transfer*, vol. 135, no. 4, pp. 1–10, 2013.

[87] S.-K. C. Yong-Jiun Lee, Poh-Seng Lee, "Experimental investigation of oblique finned microchannel heat sink," in *12th IEEE Intersociety Conference on Thermal and Thermomechanical Phenomena in Electronic Systems*, pp. 1–7, 2010.

[88] Y. I. C. Bock Choon Pak, "Hydrodynamic and Heat Transfer Study of Dispersed Fluids With Submicron Metallic Oxide," *Experimental Heat Transfer : A Journal of Thermal Energy Transport , Storage and Conversion*, pp. 37–41, 2013.

[89] Y. Xuan and W. Roetzel, "Conceptions for heat transfer correlation of nano fluids," *International Journal of Heat and Mass Transfer*, vol. 43, pp. 3701–3707, 2000.

[90] C. Anbumeenakshi and M. R. Thansekhar, "On the effectiveness of a nanofluid cooled microchannel heat sink under non-uniform heating condition," *Applied Thermal Engineering*, vol. 113, pp. 1437–1443, 2017.

[91] M. R. K. S.Kandlikar , S.Garimella, D.LI, S.Colin, *Heat transfer and fluid flow in minichannels and microchannels*. Elsevier, 2006.

[92] J. R. Taylor, "An introduction to error analysis the study of uncertainties in physical measurements." Sausalito, Calif: University Science Books, 1997.